Dependence of transport in high-beta low collisional H-modes on ExB-shear and q-profile

Maximilian Reisner

München 2022

Dependence of transport in high-beta low collisional H-modes on ExB-shear and q-profile

Maximilian Reisner

Dissertation
an der Fakultät für Physik
der Ludwig–Maximilians–Universität
München

durchgeführt am
Max-Planck-Institut für Plasmaphysik,
Garching bei München

vorgelegt von
Maximilian Reisner
aus Dachau

München, den 16. August 2022

Erstgutachter: PD Dr. Jörg Stober

Zweitgutachter: PD Dr. Alexei Ivlev

Tag der mündlichen Prüfung: 21.11.2022

Contents

Zusammenfassung

Kernfusions-Kraftwerke sind eine attraktive Option, in der Zukunft nachhaltig, verlässlich und sicher Energie zu erzeugen. Ein vielversprechender Typ Fusionsreaktor ist der Tokamak, in welchem Plasma von einem spiralförmigen Magnetfeld in einem toroidalen Gefäß eingeschlossen wird. Die maximal erreichbare Temperatur im Zentrum eines solchen Reaktors – und damit auch die maximale Leistung, die darin produziert werden kann – ist durch Turbulenz beschränkt. Diese kann einen signifikanten Transport von Wärme aus dem Plasma heraus verursachen. In vorhergehenden Experimenten sind Temperaturen im Zentrum von Tokamaks beobachtet worden, die deutlich über dem liegen, was moderne numerische Modelle vorhersagen würden. In dieser Arbeit werden experimentelle und numerische Studien präsentiert, in denen untersucht wird, welche Effekte für die beobachtete Unterdrückung von Turbulenz verantwortlich sind.

Eine mögliche Ursache sind verscherte Flüsse in poloidaler Richtung, die turblente Strukturen dekorrelieren. Die Ursache für diese sogenannte $E\times B$-Verscherung ist eine Drift im Plasma, die von radialen elektrischen Feldern E_r erzeugt wird. In dieser Arbeit wurden Experimente durchgeführt, in denen diese $E\times B$-Verscherung variiert wurde. Hierzu wurden die Plasma-Heizsysteme so umgestellt, dass die Rotation des Plasmas – der Hauptverursacher radialer elektrischer Felder im Zentrum – reduziert wird. Da diese Umstellung der Heizsysteme auch andere Parameter beeinflusst, die möglicherweise relevant sind, wurden nicht-lineare Simulationen mit dem gyrokinetischen Code GENE durchgeführt, um die Stärke dieser verschiedenen Effekte separat zu untersuchen. Sowohl in den Experimenten als auch in den Simulationen wurde kein Zusammenhang zwischen der beobachteten Reduktion turbulenten Transports und der $E\times B$-Verscherung gefunden.

Stattdessen konnte in weiteren Experimenten eine starke Abhängigkeit von dem sogenannten q-Profil – ein Maß für die Helizität der magnetischen Feldlinien – festgestellt werden. Wenn man q erhöht und so formt, dass die magnetische Verscherung s – ein normierter Gradient von q – im Zentrum negativere Werte annimmt, steilt sich das Ionen-Temperatur-Profil auf. Wie bei den Untersuchungen zur $E\times B$-Verscherung wurden erneut nichtlineare GENE Simulationen durchgeführt, um Effekte des q-Profils von anderen potenziell konkurrierenden Effekten zu separieren. Detailliertere Studien, in denen untersucht werden sollte welche Aspekte des q-Profils genau für die Reduktion des Transports verantwortlich sind, führten leider nicht zu einem endgültigen Ergebnis, da es schwierig ist das q-Profile mit hoher Präzession zu messen.

Trotzdem konnten in den vereinzelten Experimenten, in denen das q-Profil mit hoher Präzision bestimmt werden konnte, einige generelle Trends beobachtet werden: Zum einen deuten die Experimente darauf hin, dass der Transport in der Nähe von Orten reduziert wird, an denen s negative Werte annimmt; theoretisch wird das damit erklärt, dass turbulente Strukturen Richtung Hoch-Feld-Seite gebogen werden, welche von Natur aus stabil gegenüber Turbulenz ist. Des Weiteren sind die Experimente generell konsistent mit numerischen Studien, laut denen die Transport-Reduktion von den genauen Werten von q

und s abhängen. Der zugrunde liegende Mechanismus hierbei ist, dass die Instabilität, die die Turbulenz verursacht, mit anderen Instabilitäten interagiert, welche von hochenergetischen Ionen getrieben werden und Energie an diese abgibt. Durch diese Interaktionen wird der Haupt-Instabilität Energie entzogen und dadurch die Turbulenz reduziert. Diese von schnellen Ionen getriebenen Instabilitäten sind empfindlich gegenüber den genauen Werten von q und s.

Basierend auf diesen Ergebnissen wurde ein heuristisches Modell in dem Transport Code TGLF implementiert, mit dem Experimente besser beschrieben werden können, bei denen er sonst den turbulenten Transport stark überschätzt. Dies hilft nicht nur, solche Szenarien mit reduziertem Transport besser untersuchen und weiterentwickeln zu können, es erlaubt auch etwas tiefere Einblicke in die Rolle, die q, s und die hochenergetischen Ionen bei der Stabilisation von Turbulenz spielen.

Abstract

Thermonuclear fusion power plants could at some point be an attractive way for humanity to harness energy in a sustainable, reliable and safe manner. One promising design for a fusion reactor is the tokamak, in which plasma is confined by helically twisted magnetic field lines in a toroidally shaped vessel. A limiting factor on the core temperature that can be achieved in such a reactor – and therefore also on the power that can be produced in it – is turbulence, since it can cause a significant transport of heat out of the plasma. In previous experiments, temperatures have been observed in the core of tokamaks, that exceed what state of the art numerical models of turbulent transport would predict. In this thesis, experimental and numerical studies are presented, that investigate what effects are responsible for this observed suppression of turbulence.

One possible cause are sheared flows in poloidal direction that decorrelate turbulence structures. The cause for this so-called $E{\times}B$-shear is a drift in the plasma created by radial electric fields E_r. In this work, experiments have been conducted that vary the $E{\times}B$-shear, by changing the heating sources of the plasma such that its rotation – the main cause for the radial electric field in the core – is reduced. Since this change in heating mix also affects other potentially relevant parameters, non-linear simulations with the gyrokinetic code GENE are performed, to disentangle between these effects. Both in the experiments and simulations, the $E{\times}B$-shear was not found to play a role in observed reduction of turbulent transport in the plasma core.

Instead, in further experiments a strong dependence on the so-called q-profile – a measure for the helicity of the magnetic field lines – became evident. By elevating q, and shaping it such that the magnetic shear s – a normalized gradient of q – reaches more strongly negative values in the core, the ion temperature profiles become more peaked. As with the investigations regarding the $E{\times}B$-shear, nonlinear GENE simulations were performed to disentangle effects of the q-profile from other potentially competing effects. More detailed studies to determine which aspects of the q-profile are responsible for the reduction of transport did unfortunately not lead to a conclusive result, since it is challenging to measure the q-profile with high precision.

Nevertheless, from the limited amount of experiments where a variety of q-profiles could be determined with great precision, some general trends could be observed: For one, experiments seem to indicate that transport is reduced near locations where s exhibits negative values; Theory explains this with turbulent structures being bent towards the high-field side, which is inherently stable towards turbulence. Furthermore, the experiments are in general consistent with numerical studies that find the reduction of transport to be dependent on the values of q and s. The mechanism here is that the instability causing turbulence interacts with other instabilities driven by suprathermal ions and transfers energy into them. Through these interactions, energy is siphoned away from the main instability, reducing the turbulence. These fast ion driven instabilities are sensitive to the exact values of q and s.

Based on these findings, a heuristic model has been implemented in the transport code TGLF, that allows it to better model experiments for which it otherwise strongly overestimates turbulent transport. This not only paves a path to be able to better study and develop such scenarios with reduced transport, it also sheds some further light on the role q, s and fast ions have on the stabilization of turbulence.

1 Introduction

With the negative effects of global warming becoming more and more noticeable in our every-day lives and many governments worldwide pledging substantial reductions in CO_2 emissions over the coming decades, the combustion of fossil fuels as our main source of energy is becoming less and less viable.

At the same time, the worldwide energy consumption increases strongly and will likely continue to do so in the foreseeable future – in particular in developing countries as they raise their standard of living [1]. It is therefore important to increase the amount of power produced by clean and sustainable sources.

The main sources of energy foreseen to be used in the future are wind and solar. However, due to their dependence on the weather, their output is inherently unreliable. To reduce the risk of the demand temporarily exceeding the energy produced, it is desirable to have reliable base-load power plants be part of the world-wide energy mix.

CO_2 neutral candidates for this would be hydroelectric power and nuclear fission. With the latter of these two, there are issues connected with the long term storage of radioactive waste, concerns regarding its safety and the potential to be weaponized. Because of these concerns, some countries, such as Germany [2], are therefore in the process of shutting down their nuclear fission power plants. And while hydroelectric power is CO_2 neutral, it generally still has a significant environmental impact as it requires the flooding of significant portions of land and obstructs the migration of fish such as salmon. It can therefore not be scaled up indefinitely.

An attractive alternative could be thermonuclear fusion power plants, which produce energy via the nuclear fusion of hydrogen isotopes into helium. Besides their controllable output, which makes them viable base load plants, they require only abundant resources as fuel, are inherently safe, and produce no long-lived radioactive waste.

1.1 Thermonuclear Fusion

Thermonuclear Fusion is the process from which also the sun and other stars draw their power. Here, the energy is derived from the binding energy that gets released when small

nuclei are combined into a larger one. In the sun, four hydrogen nuclei are fused into helium over several intermediate steps – the so-called proton-proton-chain. Since these steps involve the transformation of two protons into neutrons – a process involving the weak interaction – the cross-section of the proton-proton-chain is very low. While this is positive for life on earth, since it means that it will take a long time until the sun has used up all its fuel, power-plants based on the exact same principle would not be viable as a source of energy here on earth.

Nuclear fusion reactors therefore instead fuse the hydrogen isotopes deuterium and tritium via the following process:

$$^2_1D \,+\, ^3_1T \,\rightarrow\, ^5_2He^* \,\rightarrow\, ^4_2He \,+\, ^1_0n \,+\, 17.6\,\text{MeV} \tag{1.1}$$
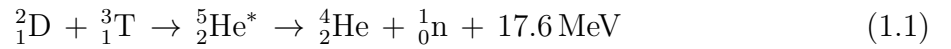
Of the 17.6 MeV released in the D-T Fusion-process, $^4/_5$ are carried off by the neutron, $^1/_5$ remains in the plasma in the form of kinetic energy of the created alpha-particle. Since deuterium and tritium already provide the right amount of protons and neutrons to form a helium nucleus, no process involving the weak force is needed. Because of this, and the fact that their combined rest mass is close to the energy of the metastable isotope ^5_2He, this reaction has a significantly higher cross section than other possible fusion reactions, including the proton-proton chain in the sun.

Still, since all the hydrogen isotope nuclei are positively charged, one first needs to overcome the Coulomb-barrier for the fusion reaction to start. For this, high relative velocities between two colliding nuclei are required, as well as a means to confine the particles so they don't push themselves apart before the fusion reactions can start.

In the sun, the energy required for this is provided by the gravitational attraction due to its enormous mass. On earth, however, these extreme conditions must be created by other means; In general, one can express the necessary conditions for a fusion power plant to reach ignition – i.e. conditions where the power from the alpha-particles alone is in principle enough to sustain the fusion reaction – with the following criterion, the so-called *triple-product* [3]:

$$nT\tau_E \geq 5 \times 10^{21}\,\text{keVsm}^{-3} \tag{1.2}$$

Here, n and T are the density and temperature of the plasma, while τ_E is the so-called energy confinement time. This is defined as the stored energy in the plasma at a given time, divided by the total input power

$$\tau_E = \frac{\frac{3}{2}\int (n_iT_i + n_eT_e)\,\mathrm{d}V}{P_{\text{input}}}, \tag{1.3}$$

where T_e and T_i are the temperatures of the electrons and ions, which typically need to be considered separately. Assuming the presence of impurities in the plasma, the same is true for the densities n_e and n_i.

There are different concepts for how the triple-product criterion could be fulfilled, such as inertial confinement fusion, in which it is envisioned to compress the D-T mixture with high energy laser pulses, such that one reaches extremely high densities that could compensate for the very low τ_E of only a few ns. As was recently published, the current record for machines using this concept, is the release of $1.37\,\text{MJ}$ of energy after depositing $1.92\,\text{MJ}$ into the D-T fuel, achieved at the US *National Ignition Facility* (NIF) [4]. In a less peaceful application, this concept has also been realized in the form of hydrogen bombs.

Another promising concept is *magnetic confinement fusion (MCF)*, which will be the focus for the remainder of this work. In MCF, the triple-product criterion is fulfilled mainly through relatively large τ_E in the range of several seconds and T in the order of several tens of keV ($\approx 100\,\text{Mio.}\,°\text{C}$). At these temperatures, the reaction rate of the deuterium-tritium reaction is near its maximum [3]. When keeping the hydrogen isotopes at such high temperatures for extended periods of time, they will be a plasma, i.e. a fully ionized but globally neutral gas, in which the electrons and ions move freely and are not directly bound to each other. Since no material is able to withstand temperatures of several million $°\text{C}$, it is necessary to somehow levitate and confine the plasma in a vacuum, which – due to the fact that the plasma is made of electrically charged particles – can be done with magnetic fields. This makes use of the fact that charged particles moving in a magnetic field are forced on circular trajectories. For sufficiently strong magnetic fields, charged particles therefore move on trajectories spiraling around the magnetic field lines.

Over the years, many different configurations of the magnetic field have been tried out: A very early approach were linear devices – so-called *Magnetic Mirror Machines* – that simply trapped the plasma on straight magnetic field lines. To avoid losing the plasma at the two ends, the devices were set up such that there were strong gradients in the magnetic field on both sides. With this, one could make use of the fact that any charged particle that fulfills the following condition

$$\frac{v_\parallel^2}{v_\perp^2} < \frac{B_{\max}}{B_{\min}} - 1 \tag{1.4}$$

gets reflected by a magnetic field gradient. Here, $v_\parallel$ and $v_\perp$ are the parallel and perpendicular component of the particle velocity, and $B_{\max}$ and $B_{\min}$ are the maximum and minimum magnetic field along the particle trajectory. As a result, the plasma particles should simply bounce back and forth between the two ends of the mirror machines. After it was found that such devices had too many end-losses, due to particles that did not fulfill the mirror condition, toroidal configurations have been used instead – essentially bending a linear machine such that the two ends are now connected.

In doing so, however, the strength of the magnetic field is no longer constant, but instead decreases with $1/R$, where R is the major radius of the torus. This gradient, together with the curvature of the magnetic field lines, leads to a drift in the trajectory of the plasma particles

$$\vec{v}_D = -\left(W_\perp + 2W_\parallel\right) \frac{\nabla B \times \vec{B}}{qB^3},$$ (1.5)

where $W_\perp$ and $W_\parallel$ are the fraction of the kinetic energy corresponding to the movement perpendicular and parallel to the magnetic field lines and q is the electric charge. For a detailed derivation of how this drift arises from the geometry of the magnetic field, see [5].

It can in fact be shown that similar drifts are caused by any external force $\vec{F}$ acting on the particles gyrating in a magnetic field. These drifts are always perpendicular to both the force and the magnetic field:

$$\vec{v}_\mathrm{D} = \frac{1}{q} \frac{\vec{F} \times \vec{B}}{B^2}$$ (1.6)

Since the ∇B Drift 1.5 is dependent on q and moves the electrons and ions in opposite directions, this leads to a charge separation causing a vertical electric field. According to eq. 1.6, the resulting electrostatic force $\vec{F}_E = q \cdot \vec{E}$ leads then ultimately to a charge independent particle drift from the high- to the low-field side, resulting in a loss of confinement.

To solve this issue, the (so far) purely toroidal magnetic field-lines can be helically twisted, such that the electrons and ions are regularly exchanged between high and low field side, before the particles at the low field side drift too far away. A simple picture to help understand this better is a spoon full of honey: When holding the spoon still, the honey will start to flow off the spoon and drip; when slowly turning the spoon, the honey can be held indefinitely.

There are two reactor designs in which such a helically wound magnetic field geometry is realized: *Stellarators* and *Tokamaks*. In stellarators, the helical magnetic field is directly created by complex three dimensional coils, that are challenging to design and manufacture. The currently largest stellarator – with a major radius of $5.5\,\mathrm{m}$ and an average minor radius of $0.5\,\mathrm{m}$ – is Wendelstein 7-X. It is located in Greifswald, Germany and has been in operation since 2015 [6, 7].

In tokamaks, instead, the magnetic field coils are planar and only create a purely toroidal magnetic field; By additionally driving an electric current I_p in the plasma, the missing poloidal component of the magnetic field is created. This current is typically induced by a strong electromagnet in the center of the torus, with the plasma acting as the secondary circuit of a transformer. The downside of this is, that a tokamak can generally only be run in pulsed operation.
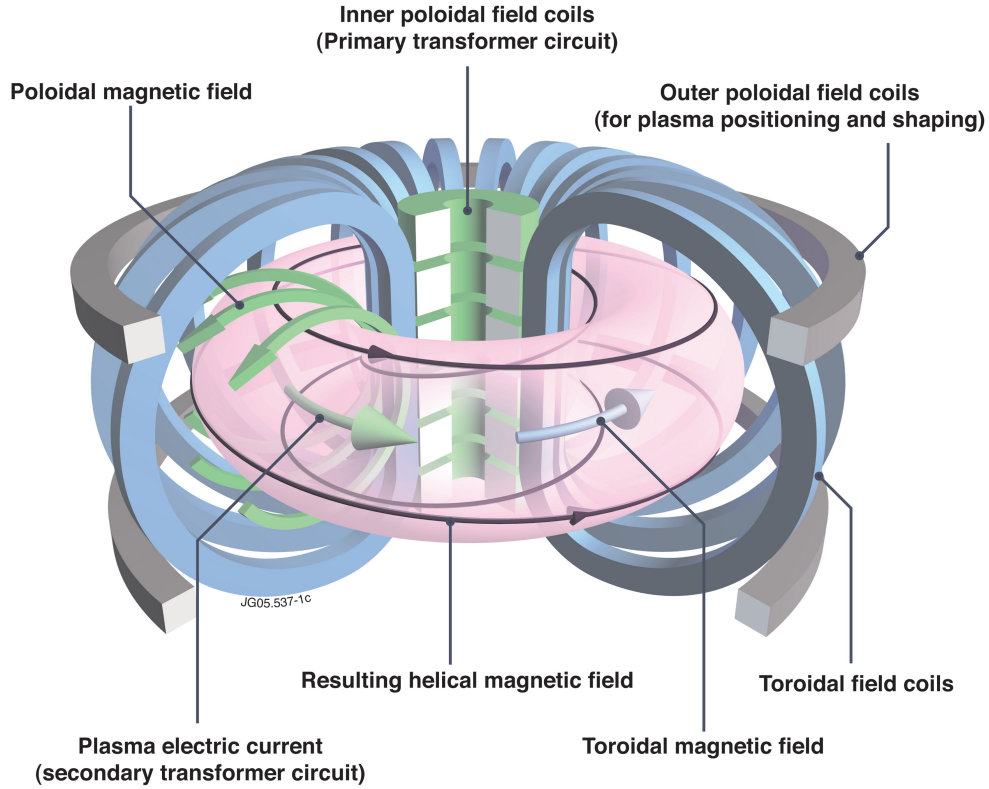
Inner poloidal field coils
(Primary transformer circuit)

Poloidal magnetic field

Outer poloidal field coils
(for plasma positioning and shaping)

JG05.537-1c

Resulting helical magnetic field

Toroidal field coils

Plasma electric current
(secondary transformer circuit)

Toroidal magnetic field

Figure 1.1: Schematic overview of the Tokamak design [8]. The helical magnetic field is composed on the one hand by a toroidal component B_{tor}, created by toroidal field coils (both in blue) and on the other hand by a poloidal component B_{pol} that is created by a toroidal plasma current I_{p} (both in green). This current is typically induced by an electromagnet in the center of the torus (also green). Additional poloidal coils are used to control the shape and position of the plasma (shown in grey).

A schematic overview of the tokamak concept can be seen in figure 1.1. Given their relative simplicity, reactors using the tokamak design are cheaper and easier to build and maintain than the ones based on the stellarator concept. For this reason, the tokamak design is technologically more mature.

The tokamak ITER – which is currently being constructed in Cadarache, France – aims to demonstrate for the first time the feasibility of achieving a surplus of energy in a nuclear fusion reactor. With its 6 m major radius and 2 m minor radius, it will be significantly larger than any other tokamak built so far [9, 10].

1.2 Scope of this Thesis

A reason for the large size of ITER is the fact that the maximum temperature and density gradients achievable in fusion experiments are limited. The reason for this is, that above

certain critical gradients instabilities arise that cause turbulence, leading to strong heat and particle transport that flattens the gradients until these critical values are no longer exceeded. The exact mechanisms behind this are discussed in section 2.3.2. If one assumes the gradients to be fixed, it is therefore necessary to increase the size of the machine to reach the desired, fusion relevant conditions in the core. A simple analogy for this is a pile of sand, whose sides have a characteristic angle that cannot be exceeded. When trying to pile the sand up steeper, friction is overcome and the sand simply flows downwards until the characteristic angle is reached again. To increase the height of the pile, one needs to broaden the base.

However, contrary to that general finding, certain experiments conducted in tokamaks such as *ASDEX Upgrade* (AUG) – where also the studies presented in this work have been carried out – steep temperature gradients have been observed that are up to a factor of two larger than expected. This implies a local reduction of turbulence that is so far not fully understood [11, 12, 13].

In this thesis, these local reductions in turbulent transport and the mechanisms behind them are investigated. This is done by conducting experimental and numerical studies that systematically vary relevant quantities such as the $E \times B$-shear and the q-profile. For definitions of these quantities, see sections 2.4.1 and 2.1, respectively. A deeper understanding of these reductions in transport would not only help to improve the performance of current day devices, it would also allow future nuclear fusion power plants to be built at a smaller size than currently deemed necessary.

To be able to extrapolate from experiments done in smaller present-day devices such as ASDEX Upgrade, to larger future machines, it is important to have transport models that are able to reproduce the results of such experiments. While so-called *gyrokinetic* codes like *GENE* (see section 2.5.1) have been shown to be able to do that, they are very expensive in time and computing resources, making them impractical for large parameter scans and simulations covering the entire radial extent. In commonly used reduced transport models, such as the *quasilinear TGLF* (Trapped Gyro Landau Fluid, see section 2.5.2), the relevant physics is not yet fully represented, leading to an over-prediction of transport. To improve upon this situation, a heuristic model implemented in TGLF is proposed in section 5.4, that allows the recovery of the experimental profiles.

In chapter 2, the open questions regarding the peaked ion temperature profiles are discussed, after first establishing the necessary theoretical background. In chapter 3 then, an overview of the tokamak ASDEX Upgrade is given, with a particular focus on the heating and current drive systems, as well as the different diagnostics used to measure the quantities relevant for the investigations presented here. In chapters 4 and 5 results of the experimental and numerical investigations are shown, concentrating on the aforementioned $E \times B$-shear and q-profile, respectively. In chapter 6, finally, these results are briefly summarized and an outlook for future investigations is given.

2 Theory and Background

So far, we considered for the most part only single particle trajectories, when describing how the plasma is confined by magnetic fields. In this picture, particles are essentially perfectly bound to a magnetic field line; with the exception of drifts, there is no transport in radial direction that would cause a loss in confinement.

As soon as one considers a thermal plasma, this changes, however. In that case, one also needs to take into account collisions between particles, which can cause radial displacements. Given the presence of gradients, this can then lead to fluxes in radial direction.

On top of that, in early fusion experiments at the beginning of the second half of the 20th century, it soon became evident that radial transport is in fact significantly higher than one would expect based on the well understood collisional theory. For some time this mysterious observation was known as *anomalous transport*, before it was finally understood that the source of it are turbulences, which are caused by gradient driven micro-instabilities.

This transport of heat and particles out of the plasma effectively limits the maximum achievable gradients in temperature and density. As mentioned before, this gives stringent lower bounds to the machine size required to reach the temperatures necessary for ignition. It is therefore desirable to operate fusion reactors such that this transport is as low as possible, predominately by suppressing turbulence.

Turbulence by itself is already one of the hardest problems classical mechanics has to offer, and adding long range electromagnetic fields to the mix – as is the case with fusion plasmas – only increases its complexity. It is therefore no surprise that transport caused by turbulence is still an active field of research. To properly describe turbulence arising in the plasma of fusion experiments, and to understand it well enough to make statements on how fusion reactors need to be operated to suppress it as much as possible, powerful numerical tools are required.

In section 2.3, an overview of the theory behind collisional and turbulent transport will be given. Building on this, in section 2.4 then, parameters that are considered important for the suppression of turbulent transport are introduced. Here, a particular focus will be given on the parameters that were investigated in more detail in this thesis. In section 2.5 then, the numerical tools are described, that were used to model turbulent transport in this

work, before then finally, in section 2.6, the open questions that are sought to be answered in this thesis are being discussed. Before all that, details on the magnetic configuration in tokamak devices and an overview of the different means of current drive that are used to shape it are given in sections 2.1 and 2.2, respectively, as a foundation for the discussions later on.

2.1   Plasma Equilibrium

As mentioned in the previous chapter, in MCF-devices the plasma is suspended with magnetic fields, to avoid it coming into contact with the surrounding vessel. This can be done, because the plasma is made up almost entirely out of charged particles; according to the Lorentz force

$$\vec{F} = q\left(\vec{E} + \vec{v} \times \vec{B}\right),\tag{2.1}$$

charged particles can move freely parallel to magnetic fields, but are forced on circular trajectories of radius $r_{\mathrm{L}} = {}^{mv_\perp}/_{qB}$, if they try to move perpendicular to it. Because of this, the plasma particles are forced on helical trajectories that follow magnetic field lines, and are thus confined. In the equations above, $\vec{E}$ and $\vec{B}$ are the electric and magnetic field, q the electric charge, and $\vec{v}$ and $v_\perp$ the total particle velocity and its component perpendicular to $\vec{B}$; r_{L} is the so-called *Larmor-radius*.

For such a setup to be stable, the forces resulting from the kinetic pressure in the plasma need to be balanced by the forces from the magnetic field, i.e. fulfill the following equilibrium condition:

$$\vec{j} \times \vec{B} = \nabla p\tag{2.2}$$

where $\vec{j}$ is the current density and p the plasma pressure.

In this context, the ratio between the average thermal pressure and the magnetic pressure

$$\beta = \frac{\langle p \rangle}{B^2/2\mu_0}\tag{2.3}$$

is a useful metric to express how efficient the plasma is confined.

A normalized value

$$\beta_{\mathrm{N}} = \frac{aB_{\mathrm{tor}}}{I_{\mathrm{p}}}\beta\tag{2.4}$$
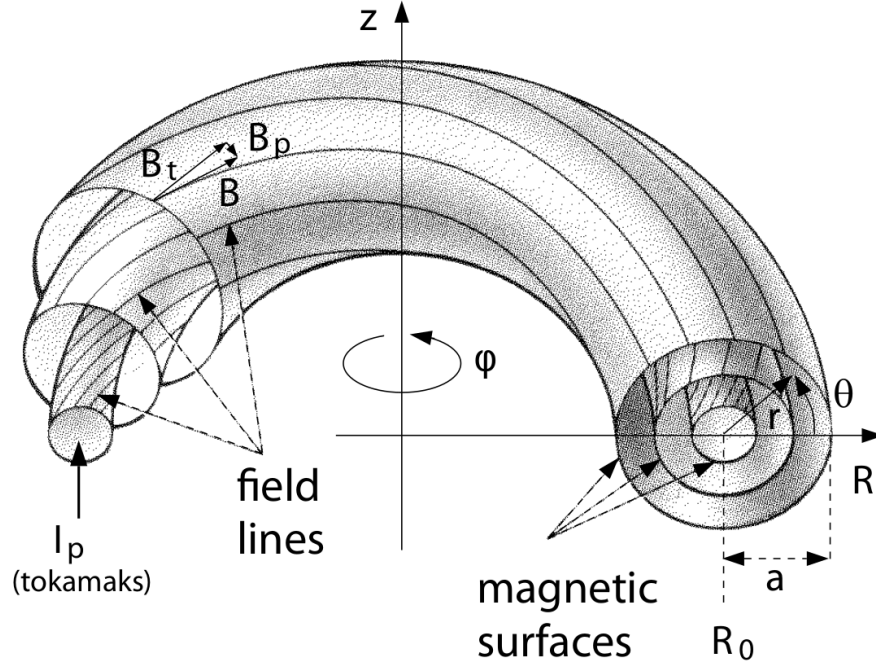
Figure 2.1: Schematic of the structure of the magnetic equilibrium in a toroidal MCF device with major radius $R = R_0$ and minor radius $r = a$. The magnetic field lines lie in nested magnetic flux surfaces and are helically wound around the torus. Figure reproduced from [14].

is used to estimate how close the plasma is to an instability in the magnetic equilibrium. Here a is the minor radius of the machine in meter and B_{tor} is the toroidal magnetic field on the plasma axis. It was found that there is a maximum value of β_{N} above which the plasma becomes unstable [15]. For conventional tokamaks, this so-called *Troyon limit* is observed to be $\beta_{\text{N}} \leq 3.5$ [16]. Another related quantity to β is β_{pol}, which replaces B with B_{pol} in equation 2.3. This parameter is useful, as the fraction of *bootstrap current* (a non-inductively driven current, that arises in the plasma spontaneously, see section 2.2.4) is proportional to it.

The magnetic structure of the magnetised plasma can be described by *Magnetohydrodynamic* (MHD) theory [17], that treats it as a single fluid (as opposed to treating electrons and ions separately). The precise shape of the magnetic equilibrium expressed in equation 2.2 can be calculated via the *Grad-Shafranov-equation* (GSE), (assuming toroidal axisymmetry, as the system can then be reduced to a two-dimensional poloidal cross-section)[3, 17]:

$$\Delta^* \psi = -\mu_0 2\pi R j_\varphi = -\mu_0 (2\pi R)^2 \frac{\mathrm{d}p}{\mathrm{d}\psi} - \mu_0^2 \frac{\mathrm{d}I_{\text{pol}}}{\mathrm{d}\psi} I_{\text{pol}}, \qquad (2.5)$$

where ψ is the poloidal magnetic flux, defined as the integral of the magnetic field over

any surface S_{pol} where $z = \text{const}$. Equivalently, one can also define a toroidal flux ϕ, that is the integral over any surface S_{tor} with $\varphi = \text{const}$.

$$\psi = \int_{S_{\text{pol}}} \vec{B} \cdot \mathrm{d}S \qquad\qquad \phi = \int_{S_{\text{tor}}} \vec{B} \cdot \mathrm{d}S \qquad\qquad (2.6)$$

For a definition of the coordinates z and φ, see figure 2.1.

In axisymmetric toroidal MCF devices, the magnetic equilibrium always takes the form of nested surfaces of constant pressure (see fig. 2.1). This can be shown by multiplying equation 2.2 with $\vec{B}$. As any vector is per definition perpendicular to a cross-product involving itself, the left hand side becomes 0. It therefore follows that the right hand side must be 0 as well, implying that the pressure gradient is perpendicular to the magnetic field lines and that $\vec{B}$ must therefore lie in surfaces of constant pressure. These nested surfaces of constant pressure that are spanned by magnetic field lines are also called *flux surfaces*. As these flux surfaces are nested and do not intersect, ψ and ϕ can be used as coordinates. This is particularly useful, since – contrary to the simplified graphic in figure 2.1 – the poloidal cross-sections of the flux surfaces have (by design) typically more complex shapes than just plain circles. This can be seen in figure 2.2.

Besides being elongated and given a slightly triangular outline, the magnetic field is shaped such that two separate regions are created: An inner region of closed flux-surfaces, and an outer region with open flux-surfaces. In this so-called *divertor configuration*, only these open flux surfaces come into contact with the wall, at dedicated locations at the bottom and/or top of the vessel – the so-called *divertor* [18]. Through this arrangement, the contamination with impurities can be significantly reduced. Furthermore, the slightly triangular shape helps to improve confinement, as it reduces the fraction of the plasma at the low-field side. As will be discussed in section 2.3, this region is inherently prone to instabilities.

To facilitate comparisons between different machines and different plasma shapes, it is useful to define normalized flux-coordinates instead of directly using ψ and ϕ. The ones most commonly used are ρ_{pol} and ρ_{tor}:

$$\rho_{\text{pol}} = \sqrt{\frac{\psi - \psi_{\text{axis}}}{\psi_{\text{separatrix}} - \psi_{\text{axis}}}} \qquad\qquad \rho_{\text{tor}} = \sqrt{\frac{\phi - \phi_{\text{axis}}}{\phi_{\text{separatrix}} - \phi_{\text{axis}}}} \qquad\qquad (2.7)$$

Here ψ_{axis} and $\psi_{\text{separatrix}}$ are the values of ψ at the magnetic axis and at the *separatrix* – the flux surface dividing the inner and outer region – respectively. Equivalent definitions are used for ϕ.

Each value for ρ (ρ_{pol} or ρ_{tor}) corresponds to one unique flux surface. We established earlier that the pressure is constant on a given (closed) flux-surface, which means it is possible to describe the pressure inside any toroidal MCF device as a simple 2D relation between p and ρ. The same holds true for other plasma quantities, such as temperature T and density n. This is because the plasma particles can move much more freely parallel to the magnetic field lines than perpendicular to them, leading to the particles at a given flux-surface being in equilibrium.

Another important flux surface quantity is the so-called *safety-factor* q, which expresses the helicity of the field lines at a given flux surface:

$$q = -\frac{\mathrm{d}\phi}{\mathrm{d}\psi} \qquad (2.8)$$

The safety-factor has its name from the role it plays in confining the plasma, without losses from drifts that arise from the curvature of the plasma. Assuming small inverse aspect ratios $\epsilon = r/R \ll 1$, the expression in equation 2.8 can be approximated by [3]:

$$q \approx \frac{r}{R}\frac{B_{\text{tor}}}{B_{\text{pol}}} \qquad (2.9)$$

Figure 2.2: Poloidal cross-section of an ASDEX Upgrade equilibrium in divertor configuration. Flux-surfaces are indicated with dashed lines, the separatrix with a solid line.

Considering B_{tor} is given by the toroidal field coils and largely independent of the conditions inside the plasma, q is mainly determined by B_{pol}. Since B_{pol} is in turn mainly dependent on I_{P}, the shape of the q-profile has a strong connection to the distribution of current in the plasma.

A lower safety-factor means a stronger helical winding, which counters the separation of charge due to drifts, that was described earlier. In figure 2.3, an example of a typical q-profile is depicted. In standard plasma scenarios, q monotonically increases from values slightly below 1 in the core to values between approximately 3 and 7 at the flux surface that encloses $95\,\%$ of the poloidal flux, before approaching infinity at the separatrix.

Over this span of values, flux-surfaces that feature a rational value of q are of particular interest. While for irrational values of q the field lines within a flux-surface are ergodic,
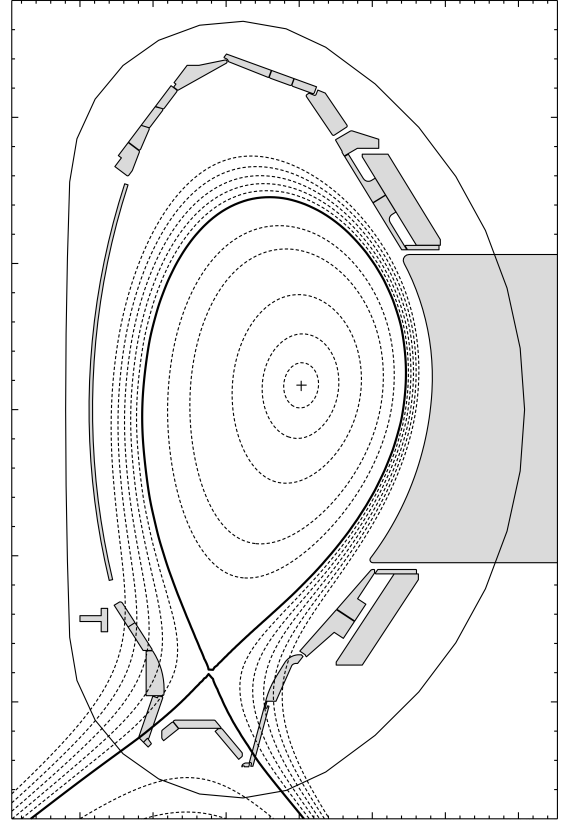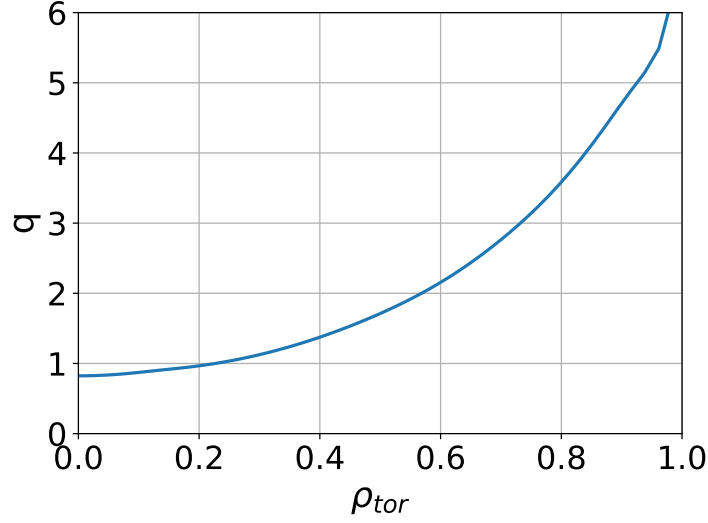
Figure 2.3: Example of a typical profile of the safety-factor q, plotted against ρ_{tor}.

i.e. one field line covers the entire flux-surface without closing in on itself, for flux-surfaces with rational values of q this is not the case. In these special cases, the field lines form a closed loop that connects back on itself after a finite number of revolutions around the torus. When this happens, small perturbations can get amplified and lead to instabilities. An example for such an instability that is regularly observed in tokamak experiments and relevant in the context of this thesis is the *sawtooth instability* [19]. This instability is located at the $q = 1$ surface, where the plasma is particularly prone to amplify perturbations, as the field lines already close in on themselves after only one toroidal and poloidal revolution around the torus. Sawteeth take their name from the characteristic shape they cause in the time-trace of parameters like the core temperature (see figure 2.4, left).

In the presence of a sawtooth instability, plasma surrounding the magnetic axis periodically gets redistributed. As a consequence, the temperatures in the very center of the plasma (fig. 2.4 (left, black)) – inside the $q = 1$ surface – sharply drop and then slowly rise over timescales of the order of $\sim 100\,\text{ms}$ before the cycle repeats itself. In the region outside the *inversion radius* (fig. 2.4 (left, grey)) the exact opposite happens, as hotter plasma from the core is exchanged with cooler plasma closer to the edge.

The exact mechanisms behind this sudden redistribution of plasma is not yet fully understood, though the general consensus is that it is caused by a sudden reconnection [20] or stochastisation [21] of magnetic field lines caused by an initial $m/n = 1/1$ MHD mode (where m and n are the poloidal and toroidal mode number of that mode, respectively). This redistribution of current also manifests itself in periodic variations of the q-profile, (fig. 2.4, right), which can be accurately modeled [22], and thus used to calibrate diagnostics that are used to accurately determine the q-profile (see section 3.2.6).

Despite this application, in general sawteeth are unwanted as they reduce fusion perfor-
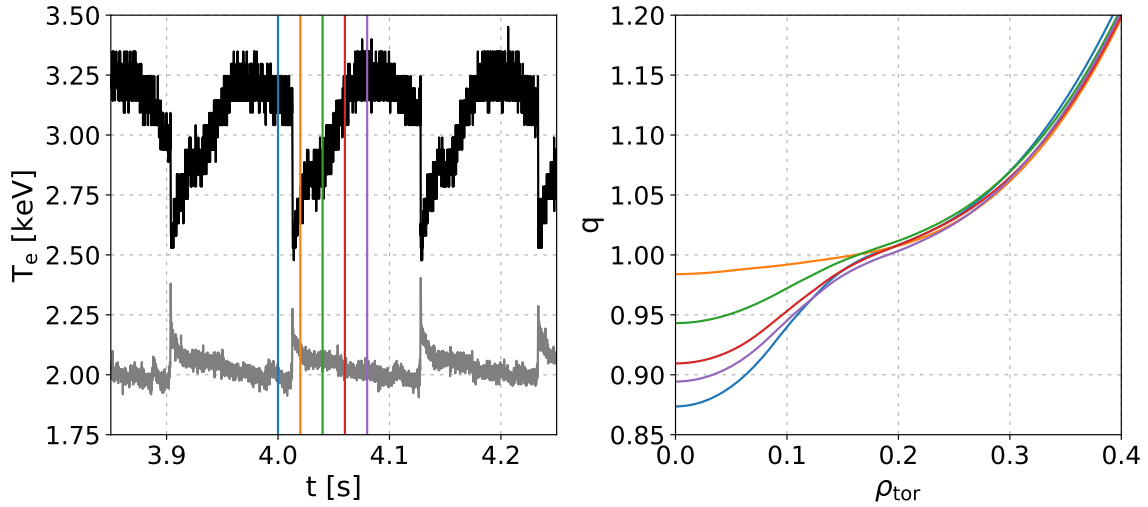
Figure 2.4: Left: Time-traces of the electron temperature of the sawtoothing ASDEX Upgrade discharge #34664, at $\rho_{\text{tor}} = 0.05$ (black) and $\rho_{\text{tor}} = 0.36$ (grey). In the black curve, the characteristic periodic shape is clearly visible, from which the name of the sawtooth instability is derived. Right: Development of the q-profile throughout a sawtooth-crash. The colors of the different profiles correspond to the time-points indicated on the left.

mance and can trigger other instabilities that ultimately may even lead to a disruption of the plasma. It is therefore desirable to avoid them. This can be done by shifting the q-profile via external current sources to values above unity, thus avoiding the $q = 1$ surface altogether. In the following section, an overview of the different sources of current drive and – related to that – heating is given.

2.2   Heating and Current Drive

In a working fusion power plant, the main heating source during operation will be the alpha particles resulting from the fusion processes. In current day devices, where the power provided by fusion processes is nowhere near to being sufficient (especially because generally they don't operate with a D-T mix), other sources of heating power are needed. But even in future reactors, additional heating sources will always be necessary during the ramp-up phase and for control. This is done via electromagnetic waves at the resonant frequencies of the electrons or ions, and by shooting energetic neutral particles into the plasma that transfer their energy via collisions after initial ionization.

Closely connected to the heating is also the external current drive, as some of these heating systems cannot just be used to increase the overall kinetic energy of the plasma particles, but are also capable of accelerating the charged particles in a preferential direction, thus creating a current.

As established previously, in a tokamak it is necessary to drive a toroidal current in the plasma to create the poloidal component of the magnetic field that is needed to keep the plasma confined. Conventionally, this is done by inducing the current via an electromagnetic coil in the center of the torus. Driving this current via induction, however, has the disadvantage that the fusion reactor can only be operated in a pulsed manner. For this reason, and maybe more importantly also to provide the ability to shape the current profile such that for example MHD instabilities like sawteeth can be avoided, other methods of current drive are needed.

In this section, the theory behind the different methods of heating and current drive will be explained in more detail. For an overview of the actual systems used in ASDEX Upgrade, see section 3.1.

2.2.1 Electron Cyclotron resonant heating and current drive

With *Electron Cyclotron Resonant Heating* (ECRH), power is deposited into the plasma via electromagnetic waves with a frequency equal to (harmonics of) the cyclotron frequency of the electrons

$$\omega_{\text{c}} = \frac{eB}{m_{\text{e}}},$$

(2.10)

where e and m_{e} are the charge and mass of an electron, respectively. At this resonant frequency, the wave is absorbed by electrons that then proceed to distribute this gained energy via collisions across the whole plasma. Due to the inefficient transfer of energy in collisions between electrons and ions – owed to the large mass difference between the two species – ECRH heats mainly the electrons. Depending on the conditions in the plasma, it can therefore happen that the temperature of the electrons T_{e} is significantly higher than the temperature of the ions T_{i}.

The following explanations are meant to only give an overview of electron cyclotron heating and current drive; for more details, the interested reader is referred to [23].

In the limit of cold plasmas, the dispersion relation of electron cyclotron waves can be approximated by

$$\tan^2\theta + \frac{P(n^2 - R)(n^2 - L)}{(Sn^2 - RL)(n^2 - P)} = 0,$$

(2.11)

where

$$n = \frac{c|\vec{k}|}{\omega}$$

(2.12)

is the refractive index, ω is the frequency of the propagating wave and P, R, L and S are functions dependent on ω, ω_c and the *plasma frequency*

$$\omega_{\mathrm{p}} = \sqrt{\frac{e^2 n_{\mathrm{e}}}{\varepsilon_0 m_{\mathrm{e}}}}. \tag{2.13}$$

Here, ω_{p} can be understood as the inverse of the time scale on which the charged particles in the plasma can still react to external fields.

In equation 2.11, θ is the angle between the wave vector $\vec{k}$ and the magnetic field $\vec{B}$. For a given value of θ, two solutions to equation 2.11 can be found, representing the so-called *ordinary mode* (O-mode) and *extraordinary mode* (X-mode) of propagation.

For values of the refractive index of $n \leq 0$, it is not possible for the wave to propagate. For this reason, there exist cutoffs that make certain regions in the plasma inaccessible to ECRH. For O-mode waves, this cutoff is for example simply ω_{p}. To get around this cutoff issue, electromagnetic waves with harmonic frequencies of ω_c are used. For the experiments conducted for this work, for example, second harmonic X-mode waves have been used.

The ECRH waves are sent into the plasma in the form of narrow microwave beams who are typically only several centimeters wide. This – in combination with the fact that the resonant frequency is dependent on the magnetic field (which in turn is dependent on the location) – means that ECRH allows for a very localised heat deposition. If the beam is angled such that it has a component parallel to the magnetic field lines (which is typically the case), one needs to take also the doppler effect into account. The doppler-shifted resonance condition of the lth harmonic, taking also relativistic effects into account, is described by

$$\omega = \frac{l\omega_{\mathrm{c}}}{\gamma} + k_\parallel v_\parallel, \tag{2.14}$$

where $\gamma = 1/\sqrt{1 - v_\perp^2/c^2 - v_\parallel^2/c^2}$ is the relativistic Lorentz-factor and $v_\perp$ and $v_\parallel$ are the component of the velocity perpendicular and parallel to the magnetic field, respectively; $k_\parallel = \omega n_\parallel/c$ is the component of the wave vector $\vec{k}$ parallel to $\vec{B}$. It is possible to rewrite equation 2.14 fully relativistically in the following form [23]:

$$\frac{v_\perp^2}{v_{\mathrm{t}}^2} = \left(1 - \frac{\omega^2}{l^2 \omega_{\mathrm{c}}^2}\right)\frac{c^2}{v_{\mathrm{t}}^2} + 2n_\parallel \frac{\omega^2}{l^2 \omega_{\mathrm{c}}^2}\frac{c}{v_{\mathrm{t}}}\frac{v_\parallel}{v_{\mathrm{t}}} - \left(1 + n_\parallel^2 \frac{\omega^2}{l^2 \omega_{\mathrm{c}}^2}\right)\frac{v_\parallel^2}{v_{\mathrm{t}}^2} \tag{2.15}$$

Here, $v_{\mathrm{t}} = c\sqrt{(2T_* + T_*^2)/(1 + 2T_* + T_*^2)}$ is the relativistic analog of the thermal velocity, using $T_* = k_{\mathrm{B}}T/mc^2$.

Equation 2.15 describes an ellipse in velocity space $(v_\perp, v_\parallel)$. For values of $k_\parallel \neq 0$, i.e. injection at an angle with a parallel component, this ellipse is shifted horizontally (towards

nonzero $v_\parallel$), which means only electrons moving in one direction fulfill the resonance conditions and are accelerated further. In figure 2.5, this is indicated with the resonance ellipse shaded in red.

The electrons that fulfill the resonance condition and are accelerated, move upward in phase space, towards higher $v_\perp$, since this is the direction in which the gyrating motion occurs with which the waves are in resonance. This is indicated in figure 2.5 with the two arrows that originate on the resonance ellipse.

Having shifted the resonance curve towards finite $v_\parallel$ can now lead to a current being driven in the plasma. This *electron cyclotron current drive* (ECCD) is caused by two opposing effects, which are briefly described in the following:

In the so-called *Ohkawa current drive* [24], the electrons have a sufficiently large increase in $v_\perp$ to fulfill the mirror-condition (eq. 1.4). This is indicated on the right side of figure 2.5 by the arrow that crosses into the region of trapped particles, delimited by the dashed lines. As the magnetic field is higher in the inner curve of the torus, particles on their helical trajectory around the torus experience gradients in the magnetic field. Particles that now fulfill the mirror-condition can no longer make a full revolution around the torus and instead bounce back and forth on the low field side of the plasma – they become *trapped*. As passing particles become trapped, they no longer contribute to the total plasma current, which effectively causes a current in the opposite direction to the one the particle was originally headed. Through collisions, the newly trapped particles are quickly
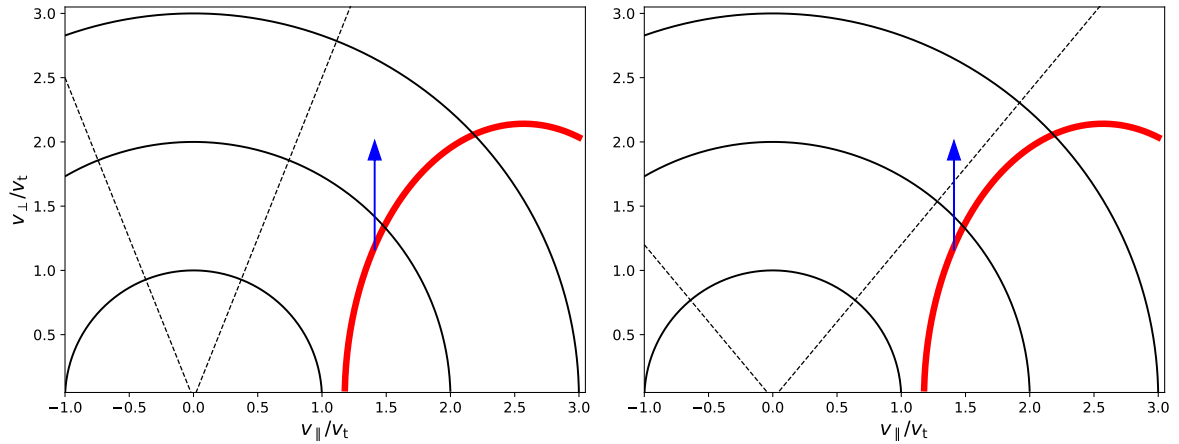

Figure 2.5: Overview of electron cyclotron current drive in velocity phase-space. The solid black semicircles indicate contours of constant electron velocity, the area above the dashed lines is the region of trapped particles, where the mirror-condition (eq. 1.4) is fulfilled. Electrons that lie on the region highlighted in red fulfill the resonance condition and are moved upwards towards increasing $v_\perp/v_t$; this is indicated with the blue arrows. Depicted on the left is the case of the Fisch-Boozer current drive, while the right shows the case of the Ohkawa current drive.

un-trapped again, but this process does not have any preferential direction, which means there is still a net current being driven.

In the so-called *Fisch-Boozer current drive* [25], the particles are far enough away in phase space from the trapping cone, that they do not become trapped (as indicated by the arrow on the left of figure 2.5). The electrons still move freely, albeit at a higher velocity v. But since the collision rate declines with the velocity ($\propto v^{-3}$), accelerated electrons take longer to be slowed down by scattering processes than their counterparts moving in the opposite direction. Through this imbalance, a net current is being driven.

These two effects go in opposite direction and depending on the conditions in the plasma, one or the other might win out. In the experiments presented in this work, the Ohkawa current drive is negligible, since heating and current drive were applied close to the magnetic axis, where the fraction of trapped particles is small.

As with heat deposition, also the position of the current drive is very localized. Given a system that allows to flexibly adjust this position – such as steerable mirrors –, the shape of the q-profile can be very well controlled.

To determine the angles at which the ECRH beams should be sent into the plasma to drive the current at the desired position, numerical calculations are necessary. For the planning of the experiments conducted within the scope of this thesis, the beam tracing code TORBEAM was used [26].

2.2.2 Ion Cyclotron Resonant Frequency heating

A similar concept to ECRH is the *Ion cyclotron resonant frequency* (ICRF) heating, which uses electromagnetic waves at the ion cyclotron frequency

$$\omega_{c,i} = \frac{ZeB}{m_i} \tag{2.16}$$

to transfer energy to the ions in the plasma. The descriptions in this section follow [27].

The dispersion relations of ICRF waves propagating through a plasma can be approximated by the following two terms, describing *fast* and *slow waves* (denoted by FW and SW) [27]:

$$n_{\perp,\text{FW}}^2 = \frac{\left(S - n_\parallel^2\right)^2 - D^2}{S - n_\parallel^2} \qquad\qquad n_{\perp,\text{SW}}^2 = \frac{P\left(S - n_\parallel^2\right)}{S} \tag{2.17}$$

Here $n_\parallel$ and $n_\perp$ are the refractive indices parallel and perpendicular to $\vec{B}$.

The quantities S, D and P are defined as

$$S = 1 - \sum_{\text{s}} \frac{\omega_{\text{p,s}}^2}{\left(\omega^2 - \omega_{\text{c,s}}^2\right)} \tag{2.18}$$

$$D = \sum_{\text{s}} \frac{\omega \cdot \omega_{\text{p,s}}^2}{\omega_{\text{c,s}} \left(\omega^2 - \omega_{\text{c,s}}^2\right)} \tag{2.19}$$

$$P = 1 - \frac{\omega_{\text{p,e}}^2}{\omega^2}, \tag{2.20}$$

where the index s in the sums refers to different ion species in the plasma. Besides this distinction, they are analogous to the definitions for the ECRH dispersion relation. This approximation neglects geometric effects and only holds in the limit of cold plasma; Nevertheless, it is sufficient for our purposes, which is to provide a general background of ICRF heating.

From these dispersion relations, it can be shown that the slow wave is evanescent in large portions of the plasma, making it unsuitable as part of a heating source. Looking instead at the fast waves, it can be shown that the waves can propagate as long as the density of the plasma is sufficiently large. As a consequence, the fast ICRF waves become evanescent only at the plasma edge. To avoid the amplitude of the waves decreasing too much in the area between the antenna and the region with sufficiently high density, it is important to place the antenna as close to the plasma as possible.

In the course of this thesis, this has posed a challenge, since for many of the experiments it was important to deposit as much ICRF heating power into the plasma as possible. At the same time, the experiments were run at rather low densities – to improve the current drive efficiency – which not only means that the cutoff-region is shifted further towards the core of the plasma, but also that a larger wall clearance is required to avoid detrimental effects from impurities sputtered from the wall. A delicate balance between these two contradicting constraints had to be maintained.

Without going into too much detail, the damping of ICRF waves at the fundamental resonance is not very strong, as the polarisation of the electromagnetic wave is in opposite direction compared to the gyro-motion of the ions [27]. To overcome this issue and be able to use ICRF waves effectively as a heating source, special heating scenarios are utilised. One example for such a special heating scheme is *minority heating*, where the frequency of the ICRF wave is tuned such that it is in resonance with ω_{c} of a minority species, such as hydrogen. Such a hydrogen minority heating scheme has also been used in the experiments discussed in this work. Via collisions, the energy is then transferred from the minority species to the rest of the plasma. As this transfer rate decreases for higher energies, a population of fast ions is built up that can have temperatures that are an order of magnitude above that of the bulk plasma.

As ω_c of H is at the same frequency as the second harmonic of deuterium – due to the factor of 2 mass difference – such an ICRF wave coupled to the hydrogen minority can also heat deuterium ions. However, this only happens when the deuterium ions have large energies, such that their larmor-radius becomes comparable to the wavelength of the ICRF wave. This occurs mostly when the deuterium ions were already accelerated, for example by *neutral beam injection heating* (NBI, see the following section) [28].

To determine ICRF heat deposition profiles or the amount of superthermal ions created by ICRF heating, it is necessary to do numerical calculations. In the work presented here, the full wave code TORIC was used [29]. To properly consider the interaction between NBI and ICRF, it is necessary to couple TORIC to models describing the effects of the NBI, such as the Fokker-Planck code SSFPQL [30].

2.2.3   Neutral Beam Injection (NBI)

Of the three methods of external heating sources described in this chapter, the concept of *Neutral Beam Injection* (NBI)[31] is comparatively simple. Here, a beam of highly energetic neutrals is shot into the plasma, which then simply distribute their energy to the rest of the plasma via collisions.

In more detail, NBI heating works as described in the following: A beam of ions – typically D^+ – is accelerated in a strong electric field, before being sent through a chamber filled with a neutral gas (typically also deuterium). When passing through this gas, the accelerated ions take electrons from the neutral gas via charge exchange reactions and are thus neutralized. After that, the now neutral beam continues on into the plasma. Beam particles that remain ionized are not able to penetrate into the plasma due to the magnetic field present there.

The neutral beam that remained unaffected by the magnetic field now collides with particles in the plasma and becomes ionized again, before it finally thermalises over a characteristic slowing-down time τ_s, heating the plasma in the process. As with ICRF heating, a fast ion population builds up as the energy is transferred less efficiently at higher energies. With NBI, the energy can be transferred to both electrons and ions, though the relative proportions depend on the beam energies and plasma parameters. In medium sized machines like AUG, NBI heats mostly the ions [32].

When injected at an angle with a parallel component with respect to $\vec{B}$, also a current can be driven in the plasma – the so-called *neutral beam current drive* (NBCD) [33]. This works, because as the neutral beam particles are ionized when they initially hit the plasma, the resulting new ions retain their momentum much longer than the electrons, which are thermalised much quicker due to the fact that the velocity of the neutral beam is still significantly lower than the velocity of the thermal electrons. This leaves a net current in the direction the beam is pointed. As electrons are being dragged along by the much heavier ions, this current is in principle shielded. However, as trapped particles cannot contribute to this shielding current, a significant portion of the neutral beam driven current remains.

Besides the fact that NBI can be used to heat the plasma and drive current, it also plays an important part in several diagnostic setups. As the beam neutrals collide with the main plasma, either they or the bulk plasma receiving an electron from them may end up in an excited state. When this excited electron eventually relaxes to the ground state, a photon is emitted, which when detected allows for the inference of several properties of the ion it was sent from – and by extension also properties of the plasma and its magnetic equilibrium. More details on the different diagnostic methods are found in section 3.2.

As with ECRH and ICRF, also NBI requires numerical calculations to determine the heat deposition and current drive profiles, as well as the amount of suprathermal ions created. In this work, several different models have been used for this task: The first one, NUBEAM [34], is a Monte-Carlo code, which is used inside the transport code TRANSP [35] (see section 2.5.4). NUBEAM is very accurate and in good agreement with experimental results, but at the same time also numerically rather expensive. Quicker, reduced models were used within simulations using the transport code ASTRA [36] (see section 2.5.3). These were the very fast RABBIT code [37] and the NBI block already included in ASTRA [38].

2.2.4 Neoclassical Bootstrap Current

Besides the external sources for current drive described in the preceding sections, a substantial amount of current can also arise spontaneously, given the right conditions. In the following section, the mechanisms behind this current – the so-called *bootstrap current* – will be explained [39].

In the previous sections and the introduction, we already established the existence of the so-called trapped particles. These particles have a high enough ratio $v_\perp/v_\parallel$ that they fulfill the mirror condition (eq. 1.4) and cannot complete the full revolution around the torus, but instead bounce back and forth on the low field side of the plasma.

On top of that, we can now recall that the gradient in the magnetic field responsible for trapping electrons on the low field side also causes a vertical drift in their motion. As the trapped particles move back and forth, also this drift changes its direction, leading to trajectories whose shape is similar to that of a banana – if projected in the poloidal plane. Such a *banana trajectory* is illustrated in figure 2.6.

As also illustrated in figure 2.6, at any given position several banana orbits intersect, with electrons from orbits closer to the core moving in opposite direction than electrons from orbits closer to the edge. In the presence of a gradient in the pressure, particles on the banana orbits closer to the core are packed more densely and move faster. Under these circumstances, the movement of the intersecting banana orbits does not fully cancel and a net current arises. This current, however, is not yet the bootstrap current. The bootstrap current itself arises through collisions with passing particles, during which the net momentum is transferred.
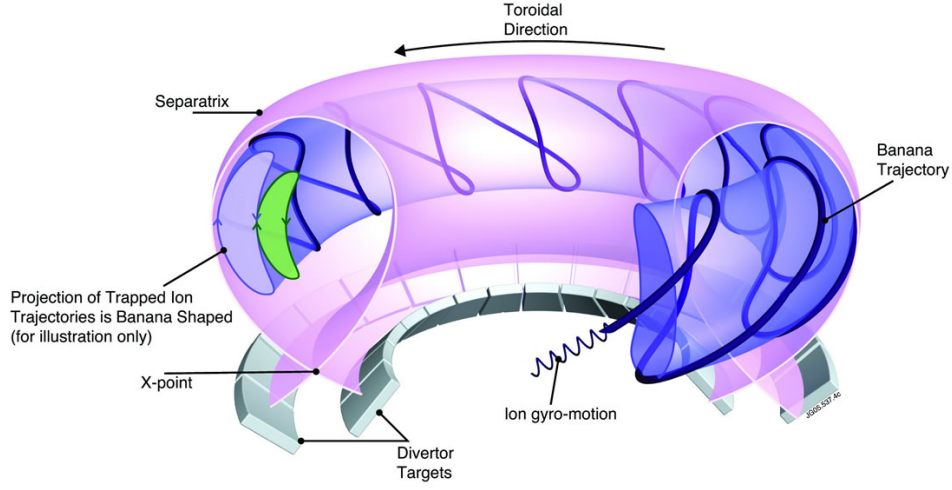
Figure 2.6: Trajectory of a trapped particle moving through a tokamak. As it is reflected on the high field side, the trajectories in opposite directions don't align. This is due to the ∇B drift in vertical direction and leads to the characteristic banana shape. Differences in population on intersecting banana orbits ultimately cause the formation of the bootstrap current. Figure adapted from [40].

Assuming a small inverse aspect ratio $\epsilon = r/R$, the bootstrap current density can be described with the following formula [39]:

$$j_{\mathrm{BS}} = -\sqrt{b}\frac{RB_{\mathrm{tor}}}{B_0}\left[2.44(T_{\mathrm{e}} + T_{\mathrm{i}})\frac{\mathrm{d}n}{\mathrm{d}\psi_{\mathrm{pol}}} + 0.69n\frac{\mathrm{d}T_{\mathrm{e}}}{\mathrm{d}\psi_{\mathrm{pol}}} - 0.42n\frac{\mathrm{d}T_{\mathrm{i}}}{\mathrm{d}\psi_{\mathrm{pol}}}\right], \qquad (2.21)$$

with $b = (B_{\max} - B_{\min})/(B_{\max} + B_{\min})$.

The terms in brackets are all in relation to the pressure gradient as the main drive for the bootstrap current. It can be seen that the density gradient has a stronger contribution than the temperature gradients. The prefactor before the bracket is essentially proportional to $\sqrt{\epsilon}/B_{\mathrm{pol}}$; The dependence on the inverse aspect ratio is related to the bootstrap current being proportional to the fraction of trapped particles in the plasma, which – for geometric reasons – is approximately $\sqrt{\epsilon}$[3]. The dependence on B_{pol} can be understood if one considers that the strength of drifts in the plasma are inversely proportional to the magnetic field (see eq. 1.6). Increasing the distance over which the particles drift, leads to wider banana-orbits, which means the differences in temperature and density between two intersecting banana-orbits increase, keeping everything else constant.

A more comprehensive description of the bootstrap current is derived in references [41, 42], which arrive at the following expression:

$$\langle j_{\mathrm{BS}}B \rangle = -I(\psi)p_{\mathrm{e}} \left[\mathcal{L}_{31} \frac{p}{p_{\mathrm{e}}} \frac{\partial \ln p}{\partial \psi} + \mathcal{L}_{32} \frac{\partial \ln T_{\mathrm{e}}}{\partial \psi} + \mathcal{L}_{34} \alpha \frac{1 - R_{pe}}{R_{pe}} \frac{\partial \ln T_{\mathrm{i}}}{\partial \psi} \right] \qquad (2.22)$$

Here $R_{\mathrm{pe}} = p_{\mathrm{e}}/p$, while $\mathcal{L}_{31}$, $\mathcal{L}_{32}$, $\mathcal{L}_{34}$ and α depend on the specific conditions in the plasma. For the exact expressions and typical values, see [41, 42].

The bootstrap current is a particularly attractive way to replace the inductively driven current, as it does not require additional recirculating power – unlike the means of external current drive described in the previous sections. It is therefore desirable to operate tokamaks such that the bootstrap current makes up as large a fraction of the total plasma current as possible. As was shown in this chapter, for this one requires on the one hand a low B_{pol} (which translates to increased values of the safety factor q), and on the other hand strong gradients in temperature and density. The latter point is another reason why the scenarios with peaked temperature profiles are an attractive mode of operation for MCF devices.

In MCF devices, the maximum achievable values for temperature and density gradients are limited by transport in radial direction, caused in particular by turbulent structures. In the following section, the underlying mechanisms behind this transport will be explained in more detail. In a subsequent section, a discussion on effects that may reduce and suppress this transport will then follow.

2.3   Transport

As will be discussed in more depth later in this section, the maximum values for T and n, as well as their gradients, are limited by fluxes of heat and particles in radial direction. To operate MCF devices such that the desired target values for n and T are achieved, the heat transport properties of the plasma need to be well understood.

As a basis of discussion, one can look at the continuity equation for the density of the stored energy $w \, [\mathrm{Jm}^{-3}]$:

$$\frac{\partial w}{\partial t} = -\nabla \cdot \vec{q} + P \qquad (2.23)$$

Changes to the stored energy over time are balanced by the heat flux $\vec{q} \, [\mathrm{Wm}^{-2}]$, as well as sources and sinks of power $P \, [\mathrm{Wm}^{-2}]$. While the sources for heating power come from fusion processes and the external heating sources discussed in the previous section, power sinks arise mainly in the form of radiation.

The heat-flux is typically described via the formula

$$\vec{q} = -n\chi\nabla T, \tag{2.24}$$

where χ is the so-called *heat conductivity*.

In steady state operation – i.e. w, n and T constant – losses via the heat flux need to be compensated by the external heating sources. In that case, it is possible to do a *power balance analysis* and solve equations 2.23 and 2.24 for χ. To predict χ and $\vec{q}$ from plasma quantities, however, a deeper understanding of the different processes contributing to the radial transport is necessary. These will be described in some detail in the following. The descriptions in this section are based on references [3, 5, 36].

2.3.1 Collisional Transport

As the charged particles in the plasma are all gyrating around magnetic field lines, one might expect that the individual particles always stay on the same flux-surface and don't move perpendicular to the magnetic field (assuming helically wound field lines that mitigate drifts). This picture, however, works only when considering single particles alone. Through collisions with other particles, transport perpendicular to magnetic field lines can occur.

Such a transport caused by collisions can very simply be described by a random walk model. Here, we say that on average every time step Δt a collision occurs that displaces the colliding particles by a distance Δx.

Since this displacement is equally likely in direction towards the core or the edge, the average position of particles starting on a given flux surface does not change. However, eventually the particles will find themselves in a normal distribution whose width increases with time. We can describe that with a diffusion coefficient

$$D = \frac{\Delta x^2}{\Delta t}. \tag{2.25}$$

Considering classical collisions between two particles, the characteristic length scale Δx of displacement is of the order of magnitude of the larmor radius r_L. The characteristic time-scale Δt is the inverse of the collision frequency ν, resulting in a diffusion coefficient $D_\mathrm{Classical} = r_\mathrm{L}^2\nu$. Given a gradient in the density, this collision based diffusion can lead to a particle flux. This, however, is only the case if the two colliding particles are not of the same species, as they would simply trade places in that case, without changing the overall distribution.

For the transport of heat, a similar derivation can be done, resulting in a heat conductivity $\chi_\mathrm{Classical} = r_\mathrm{L,s}^2\nu$, that causes a transport of heat given a gradient in the temperature. Unlike the particles themselves, heat can also be transported when the two colliding particles are of the same species s, as long as they have different energies.

If one calculates D and χ based on these considerations, one arrives at values that are several orders of magnitude lower than the values that are experimentally observed, indicating that there are additional means of perpendicular transport.

An additional term is contributed by trapped particles on their banana orbits. Taking them and their collisions into account – in the so-called *neoclassical theory* –, the characteristic length scale Δx from equation 2.25 that needs to be considered is the width of the banana orbit. This width can be approximated by $w_\mathrm{B} = r_\mathrm{L} q/\sqrt{\epsilon}$. As w_B is larger than r_L, collisions involving trapped particles cause a larger radial displacement than what was assumed in the derivation of $D_\mathrm{Classical}$ and $\chi_\mathrm{Classical}$.

Besides that, when considering trapped particles, also the collision frequency is higher and increases to the effective collision frequency $\nu_\mathrm{eff} = \nu/2\epsilon$. This increase can be explained as follows: When two particles in the plasma collide, the angle they are deflected by is typically very small. To be displaced by one larmor radius – as was assumed in the derivation of the classical diffusion coefficients – they need to be deflected by 90°; the collision frequency ν used in the previous derivation therefore actually represents the frequency in which particles cumulatively are deflected by 90°. For trapped particles on banana-orbits, the situation is now different: For the particles to be displaced by one banana-width, they just need to become un-trapped, which requires a much smaller deflection angle.

When we now plug these values for Δx and Δt into equation 2.25, we can calculate a neoclassical diffusion coefficient

$$D_\mathrm{neo} = w_\mathrm{B}^2 \nu_\mathrm{eff} \frac{n_\mathrm{trap}}{n} = r_\mathrm{L}^2 \frac{\nu q^2}{2\epsilon^2} \sqrt{2\epsilon} \approx \frac{q^2}{\epsilon^{3/2}} D_\mathrm{classical}. \tag{2.26}$$

For this calculation, also the fraction of trapped particles $n_\mathrm{trap}/n \approx \sqrt{\epsilon}$ needed to be considered.

As for the classical case, an equivalent derivation can be performed for the neoclassical heat conductivity. It should be noted that in this derivation of the neoclassical diffusion coefficient and heat conductivity, the assumption was made that the trapped particles complete at least one banana-orbit before they are involved in a collision. At larger collision rates, where trapped particles collide before they can complete one orbit, the random walk model does not apply anymore. In this so-called *Pfirsch-Schlüter regime*, D and χ are lower than the values in the *banana regime*, but still significantly higher than the classical values.

If one now again compares the neoclassical values for D and χ with the values observed in experiments, however, they are still underestimated by one or two orders of magnitude. For a long time, this transport not captured by theory has been known as *anomalous transport*, before it was finally understood what the physics mechanisms behind it was. These will be discussed in the following section.

2.3.2   Turbulent Transport

After puzzling for a long time about the unexpectedly large transport coefficients, orders of magnitude above what one would expect from collisional theory, it was finally realized that this anomalous transport can be attributed to fluctuations in temperature, density and plasma potential. These fluctuations are owed to turbulence eddies, which arise from *micro-instabilities* [43, 44] that can get amplified if *critical gradients* in temperature or density are exceeded. If that is the case, small initial perturbations can grow into larger, radially extended structures which transition to turbulence via processes similar to *Kelvin-Helmholtz instabilities*.

In this section, micro instabilities that are relevant in the context of this work are introduced, as well as parameter dependencies of the critical gradients above which they are excited.

Micro-Instabilities

There are several different types of micro-instabilities that can lead to turbulent transport in a MCF device: These include so-called *interchange instabilities* that are driven by gradients in the temperature and are aptly named *electron-* and *ion temperature gradient driven modes* (ETG and ITG mode), the so-called *trapped electron mode* (TEM), which is driven by gradients in n_e and T_e, as well as *kinetic balloning-* (KBM) and *microtearing-modes* (MTM), which are electromagnetic instabilities that occur at high β.

In the context of this thesis, the most important one of these is the ITG mode; the focus of this section will therefore be on discussing interchange modes in general and the ITG mode in particular. For a more in-depth description about the other types of micro-instabilities, in particular *drift-wave instabilities* in the form of TEMs, the reader is referred to references [3] and [5].

As discussed in section 1.1, the curvature of the magnetic field lines in a toroidal configuration and the resulting gradient in the magnetic field lead to a charge dependent drift in vertical direction. Recalling equation 1.5, the magnitude of this drift is proportional to the kinetic energy of the particles and therefore also to their temperature. This now comes into play if we assume a small periodic perturbation of the temperature on a given flux surface, as is sketched in figure 2.7. Assuming a temperature gradient in radial direction pointed towards the center of the plasma, such a perturbation leads to periodic fluctuations in the temperature on the flux-surface we are looking at. Due to the temperature dependence of the curvature drift, an accumulation and rarefaction of ions at the interfaces between high and low temperature occurs, since the ions from the high temperature region can move quicker into the low temperature region than the ions there can move away, and vice versa. Assuming the electrons respond adiabatically, this periodic ion density perturbation immediately leads to an electron density perturbation such that *quasi-neutrality* (i.e. that the plasma globally remains electrically neutral) is maintained. Parallel force balance then implies the existence of an electrostatic potential Φ that is proportional to the density per-
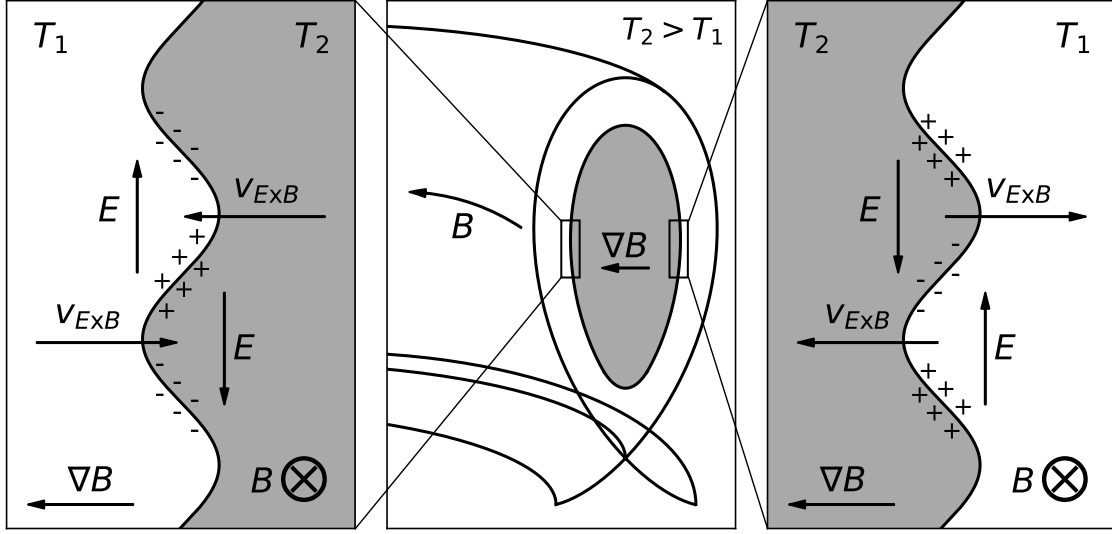
Figure 2.7: Schematic overview of the mechanism that leads to the emergence of an ITG mode. Periodic perturbations in T_i lead to a periodic variation of v_D, resulting in periodic electric fields. These fields cause a $E \times B$ Drift $v_{E \times B}$ that either stabilizes the initial perturbation (high field side, left) or further amplifies it (low field side, right).

turbation. This potential then results in an electric field $\vec{E} = -\nabla \Phi$ that causes a charge independent $E \times B$ drift $v_{E \times B} = (\vec{E} \times \vec{B})/B^2$ in radial direction. As is shown in figure 2.7, this works out such that on the low field side of the torus, this $E \times B$ drift amplifies the initial perturbation, which then ultimately leads to the creation of turbulence. On the high field side on the other hand, the drift is directed such that the initial perturbation is stabilized.

Such an interchange instability – which is named for the *Rayleigh-Taylor* [45] like mixing between high- and low-temperature regions it can cause – can be driven both by gradients in the ion- as well as the electron-temperature, following the same basic principle. The main difference between the ∇T_i driven ITG and the ∇T_e driven ETG is the characteristic length scale at which they appear. While the scale of ITG turbulence is of the size of the ion larmor radius $r_{L,i}$, the size of ETG turbulence is of much smaller scale, in the range of the electron larmor radius $r_{L,e}$.

Critical Gradients

As stated before, these micro-instabilities only get destabilized and cause increased transport, if the gradients driving them exceed a certain threshold. In the case of the ITG mode for example, the relevant parameter is the normalized ion temperature gradient $R/L_{T_i} = R \frac{\nabla T_i}{T_i}$. As long as it is below a critical gradient $(R/L_{T_i})_{\text{crit}}$, the mode remains stable. As soon as this threshold is exceeded, the heat flux rises dramatically with small increases in R/L_{T_i}. As these strong fluxes flatten the temperature profiles until their gradients are

again close to the critical value, it is in practice difficult to obtain temperature gradients that exceed this threshold by a significant amount. This behaviour is known as *profile stiffness* [46] and severely limits the temperatures that can be achieved in the core of a fusion plasma.

However, the critical gradient is not at all a fixed value, but is instead dependent on several parameters. An expression for the parameter dependence of the critical gradient of the ETG mode is derived in reference [47]. In the limit of low ϵ and β, this expression can also applied to the ITG mode:

$$\left(\frac{R}{L_{T_\mathrm{i}}}\right)_\mathrm{crit} = \max\left\{\left(1 + \frac{T_\mathrm{i}}{T_\mathrm{e}}\right)\left(1.33 + 1.91\frac{s}{q}\right)(1 - 1.5\epsilon)\left(1 + 0.3\epsilon\frac{\mathrm{d}\kappa}{\mathrm{d}\epsilon}\right), 0.8\frac{R}{L_n}\right\} \quad (2.27)$$

Here $\kappa = b/a$ is the plasma *elongation*, defined as the ratio between the vertical and horizontal extent of the confined plasma; s is the *magnetic shear*, a measure of how much the safety factor q changes with the radius [5]:

$$s = \frac{r}{q}\frac{\mathrm{d}q}{\mathrm{d}r} \quad (2.28)$$

Equation 2.27 shows that possible ways to shift the critical gradient to higher values include either changing the shape of the plasma or producing very peaked density profiles. The quantities that are perhaps more relevant in the context of this thesis are the temperature ratio $T_\mathrm{i}/T_\mathrm{e}$ as well as the shear s and safety-factor q, which are of course related to each other.

2.4 Means to reduce turbulent transport

In the previous section, parameters were discussed that can affect turbulent transport by modifying the critical gradient above which the underlying micro-instability grows unstable. Beyond that, there are also other mechanisms that can lead to a reduction or suppression of turbulence. The most prominent evidence for this is the existence of the so-called *high confinement mode* (or short *H-mode*), which is a mode of operation widely observed in modern tokamak experiments [48]. Compared to the regular mode of operation – also referred to as *low confinement mode* or *L-mode* – the H-mode features a great improvement of the energy confinement time, by approximately a factor of 2. It was first discovered in 1982 at the tokamak *ASDEX* in Garching [49].

The H-mode regime can be accessed if the external heating power exceeds a certain threshold, though the exact mechanisms behind this are not yet fully understood and still a focus of active research. After transitioning to the H-mode, the plasma in a thin layer close to, but inside, the separatrix – typically a few centimeters wide –, spontaneously organizes
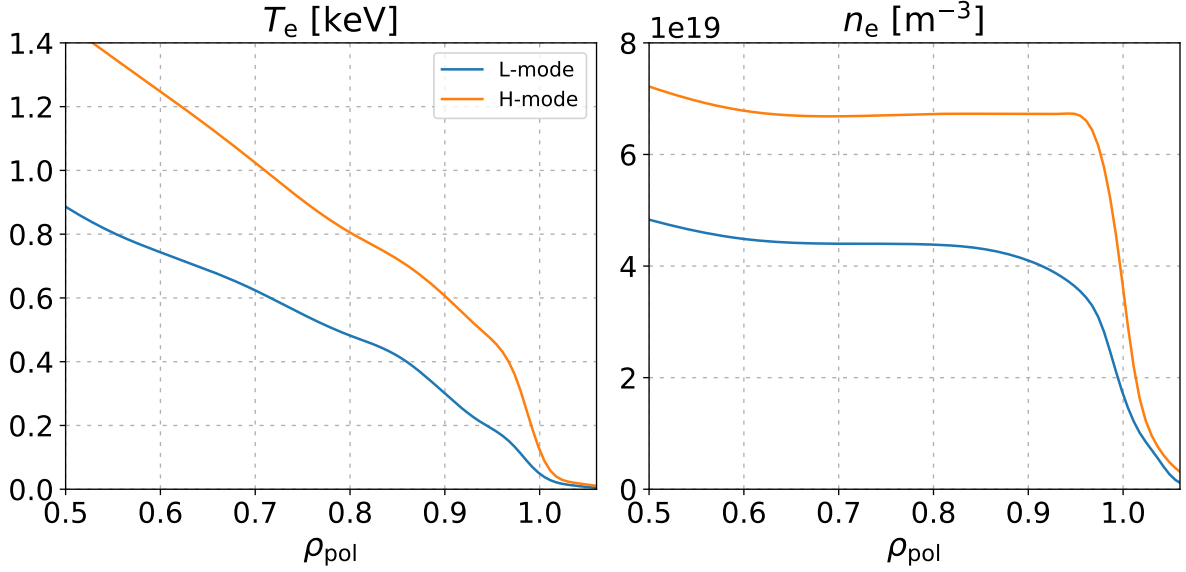
Figure 2.8: Electron temperature and density profiles of AUG discharge #39587, comparing L-mode (1.5 s, blue) and H-mode (1.9 s, orange).

itself such that turbulence is suppressed and therefore radial transport strongly reduced. This region of reduced transport is also referred to as an *edge transport barrier*, or ETB for short. At the location of the ETB, without turbulent transport, much steeper gradients in temperature and density are possible. This results in the otherwise stiff profiles to be shifted upwards, allowing to reach significantly higher values for temperature and density in the core (see figure 2.8).

When hearing about a transport barrier in the edge region of the plasma leading to a significant improvement in confinement, one might wonder if it is also possible to further improve things by creating additional transport barriers further towards the core. Indeed, such *internal transport barriers* (ITB) have been observed in a number of machines, [50, 51, 52, 53] though only transiently for at most a few energy confinement times. It is so far not clear whether ITB are caused by the same mechanisms that lead also to the suppression of turbulence causing the ETB. In the following, several key parameters will be discussed, that are thought to be connected with the formation of transport barriers or more general the reduction and suppression of turbulence in a fusion plasma.

2.4.1 $E \times B$-shear

Though the exact mechanisms that lead to the transition from L- to H-mode are not yet fully understood, it is widely accepted that the suppression of turbulence associated with the formation of an ETB is caused by a sheared poloidal flow in the plasma that decorrelates turbulence structures [54, 55]. A sketch of this process is shown in figure 2.9.
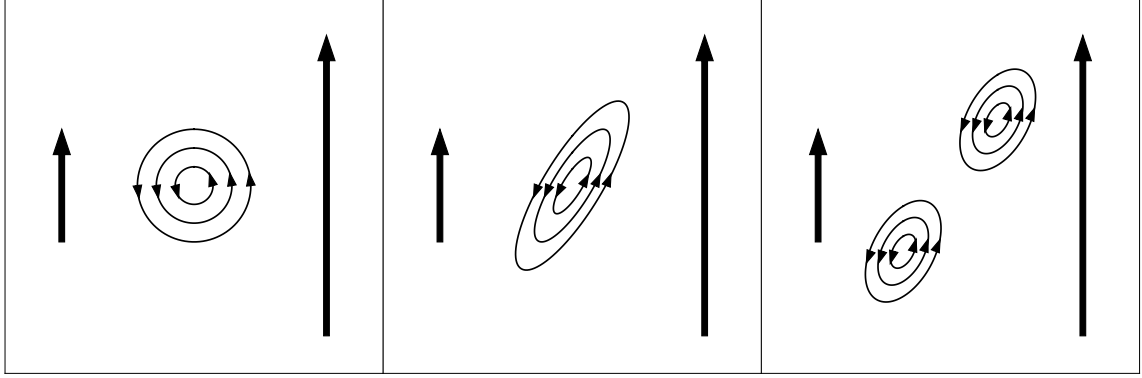
Figure 2.9: Schematic overview of how turbulence is suppressed by the $E{\times}B$-shear. A shear in the background $E{\times}B$ flow (black arrows) deforms and eventually decorrelates turbulence eddies, reducing the distance particles can be transported by these eddies.

This flow comes from an $E{\times}B$ drift

$$\vec{v}_{E{\times}B} = \frac{\vec{E} \times \vec{B}}{B^2} \tag{2.29}$$

that is caused by a radial electric field E_r, which can be calculated via the radial force balance equation [56]:

$$E_r = v_{\text{tor}}B_{\text{pol}} - v_{\text{pol}}B_{\text{tor}} + \frac{1}{eZ_{\text{imp}}n_{\text{imp}}}\frac{\mathrm{d}p_{\text{imp}}}{\mathrm{d}r}. \tag{2.30}$$

Here v_{tor} and v_{pol} are the rotation velocities in toroidal and poloidal direction, and B_{tor} and B_{pol} are the toroidal and poloidal magnetic fields. In principle, this electric field is caused by the movements of the main ions, but any other ion species must uphold the same relation as well. In the third term, Z_{imp}, n_{imp} and $p_{\text{imp}} = n_{\text{imp}} \cdot T_{\text{imp}}$ are therefore the charge, density and pressure of the impurity species boron, as these are quantities that can actually be measured (see section 3.2.5).

To decorrelate turbulence eddies, this $E{\times}B$ flow needs to be sheared, i.e. have strong changes in magnitude and direction for small changes in radial position. To quantify this, one can derive an $E{\times}B$ shearing rate [57, 58]

$$\omega_{E{\times}B} = \left| \frac{(RB_{\text{pol}})^2}{B} \frac{\partial}{\partial\psi} \left(\frac{E_r}{RB_{\text{pol}}} \right) \right|, \tag{2.31}$$

which in first order is indeed just the radial gradient in E_r. If this shearing rate exceeds the growth rate of the turbulence structures, transport is suppressed.

Since this mechanism is widely accepted as the explanation of the ETB, it stands to reason that also the ITB that have been observed may be caused by it. This is still an open point of research, with some studies finding a connection [57, 59], and others not [60].

2.4.2 Negative magnetic shear

Another parameter that has been observed in multiple machines [51, 61, 62, 63] to be related to ITBs is the magnetic shear s. In particular, negative values of s seem to be of importance. In the following, reasons behind this are discussed [50, 64].

In section 2.3.2, the description of microinstabilities and how they lead to turbulence was done in a two-dimensional picture. This simplification is in principle justified as the processes involved are axisymmetric. Nevertheless, as the particles move back and forth between the high- and the low-field side, following the helical field lines, the same is also true for the radially extended perturbations that ultimately lead to turbulence eddies.

Given a non-zero magnetic shear – i.e. assuming that the helicity of the field lines changes between neighboring flux-surfaces – different parts of these radially extended structures move at different speeds in poloidal direction, which results in them being sheared apart. According to this picture, a stronger shear – be it positive or negative – should lead to a stronger suppression of turbulence. This result has also been found in numerical studies [65]. The reason why particularly negative values of s are found to be associated with ITB, and not strong positive values of s can be easily understood when looking at figure 2.10.

Before they are actually sheared apart in the presence of a finite magnetic shear, the radially extended structures are initially just bent. For a positive s, the geometry works
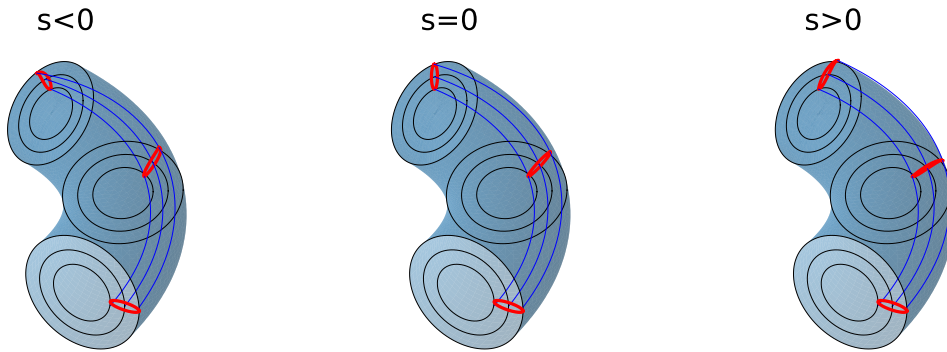

Figure 2.10: Schematic overview of the effect the magnetic shear has on radially extended mode structures. For both $s < 0$ and $s > 0$, the structures are sheared apart, leading to a decorrelation of the structures, similar to the effect of the $E \times B$-shear. While for $s > 0$ the structures are bent towards the unstable low-field-side, for the $s < 0$ case the structures are bent towards the stable high-field-side, explaining why a negative magnetic shear has a particularly stabilizing effect.

out such that this bending moves the structures towards the *bad curvature region* on the low field side, while for negative *s* they are bent towards the *good curvature region* which provides additional stabilization [66].

2.4.3 Fast ions

The final avenue for suppressing turbulent transport described here are fast ions – highly energetic particles. In future nuclear fusion reactors, fast ions will be created during fusion reactions in the form of helium ash; in today's machines, they are produced by different heating sources. Fast ions of the main ion species are typically ionized particles that have been deposited into the plasma via NBI heating, before they are slowed down and thermalized. Fast ions of a minority species – such as hydrogen – are rather accelerated by ICRF heating. There are a number of different ways in which fast ions can lead to the stabilization of microinstabilities and therefore the suppression of turbulent transport:

The first mechanism is by dilution of the main ion species [67]. Due to their significantly higher energies, the drift velocity of the fast ions is different from the one of the main ions. Because of this, they cannot contribute to the main ion ITG instability. As fast ions displace main ions, due to quasi-neutrality, an increase in fast ions directly results in a stabilization of the main ion ITG.

The second aspect in which fast ions can facilitate the reduction of transport, is by increasing the so-called *Shafranov shift*, which is a shift of the center of the nested flux surfaces in direction of the low field side. When such a shift occurs, the density of the magnetic field lines increases on the low field side, which is effectively the same as increasing the poloidal magnetic field. As a consequence, the angle of the field lines on the low field side steepens, meaning particles move more quickly through the low field side and spend less time in the bad curvature region. The magnitude of the Shafranov shift is typically proportional to β. As energetic particles can have a significant contribution to the plasma pressure (and therefore β), it can be easily understood that they lead to an increase in the Shafranov shift [5]. Though of course also the thermal pressure contributes to this increase of Shafranov shift.

The third and most important mechanism in the context of this thesis, is a nonlinear effect for which only recently an explanation has been found in numerical studies [68, 69]. Here, the fast ions drive linearly marginally stable subdominant modes such as *Alfvén eigenmodes* or *kinetic ballooning modes*, that can couple with the dominant ITG mode. Through this interaction, the subdominant energetic particle driven mode can become non-linearly excited and drain energy away from the ITG, stabilizing it in the process. According to [69], this effect leads to a linear decrease of Q_i with both T_{fast}/T_e and $R/L_{T_{\text{fast}}}$. Furthermore, the threshold above which the marginally stable modes are excited depend strongly on the magnetic geometry and have been found to increase quadratically with the safety factor q. The magnetic shear s also has a strong effect and can be either stabilizing or destabilizing, depending on other parameters.

2.5   Codes used to model transport

Theoretical advances in the field of magnetized plasma turbulence have made it possible to recover the experimentally observed levels of heat and particle fluxes much better. However, due to the interdependencies between the parameters discussed in the previous sections – describing for example the magnitude of critical gradients, the coupling between different instabilities, or to what extent turbulent structures arise in the first place – numerical tools are required to properly describe these phenomena and make meaningful predictions. Depending on the specific objective of the simulations, various codes are used; In the following, the different codes that are used in this work to model transport are described, along with a brief overview of their respective underlying theoretical basis.

2.5.1   GENE

GENE (**G**yrokinetic **E**lectromagnetic **N**umerical **E**xperiment) is a *gyrokinetic* microturbulence transport code [70]. The way it is set up in this work, GENE takes as input the temperatures, densities and gradients thereof of an arbitrary amount of particle species (electrons, ions, impurities, etc.), as well as some quantities defining the geometry and magnetic equilibrium, and calculates from this fluctuations of the scale of r_{L}, along with the resulting transport coefficients. Alternatively, in the so-called flux-driven mode, one can also use profiles of the absorbed power and particle sources as input and calculate the kinetic profiles. GENE is well benchmarked and optimized to run very efficiently on modern supercomputers. Typically, simulations are run locally, on a narrow *flux-tube* centered on only one flux-surface, but it is also possible to study non-local effects by extending the box-size for global simulations.

The underlying gyrokinetic theory is based on statistical kinetic equations, but simplifies them by averaging over the fast gyrating movement of the particles around the field lines. Finite larmor radius effects are still considered by describing the point-like particles as charged rings. This average can be done, because the cyclotron time-scale at which the particles gyrate around the field lines is much smaller than the time-scale at which microinstabilities evolve

$$\tau_{\mathrm{cyc}} = \frac{m}{eB} \ll \frac{R}{v_{\mathrm{th}}} = \tau_{\mathrm{turb}}. \tag{2.32}$$

In doing this average, not only are the requirements on the time resolution of the simulations relaxed, the problem is also reduced from six dimensions to five, eliminating one dimension in velocity space. This approach is very powerful and can accurately describe a multitude of effects [71]. However, despite the simplifications described, simulations based on the (non-linear) gyrokinetic equations are computationally still very expensive; Local fluxtube simulations – run on modern supercomputers – can easily require several days to finish. For many applications, such as the development of new scenarios, where it is

necessary to iterate over a large number of simulations, this is prohibitively expensive. For these applications, the availability of reduced models that can be run on much shorter time-scales, is important. Naturally, in order to achieve this, the models must be further simplified, resulting in a reduction of physics fidelity.

2.5.2 TGLF

A more simplified code compared to GENE is the *quasilinear* transport model TGLF (**T**rapped **G**yro **L**andau **F**luid) [72]. The first step in reducing its complexity is moving from a kinetic framework to a fluid picture, which means moving from looking at distribution functions in phase space to describing macroscopic quantities as functions of time and space. This is done by averaging conserved quantities like the mass, the momentum and the energy over the distribution functions, yielding fluid equations or *moments* of the distribution function. If the moments of the distribution function are based on gyrokinetic equations – as is the case with TGLF – the results are so-called *gyrofluid* equations.

Quasilinear models such as TGLF reduce the computational cost even further by solving linearized equations. To still take non-linear effects into account, additional rules are imposed, which are typically fitted to a large database of non-linear qyrokinetic simulations. In TGLF, such rules include the so-called saturation rule [73, 74], that governs how the amplitude of turbulent fluctuations saturates, and the spectral shift model [75], which determines how much the $E \times B$ velocity shear suppresses turbulence. As alluded already by its name, additional important features more unique to TGLF are that it contains an accurate description of trapped particles and that – despite it being a fluid code – it is still able to capture the kinetic effect of *landau damping*.

Like GENE, TGLF takes plasma parameters such as temperatures and densities on a given flux-surface – as well as the normalized gradients thereof – as inputs, along with parameters specifying the (magnetic) geometry and returns transport coefficients for that radial position as output. Due to the multiple simplifications, TGLF requires only very short times for these simulations – of the order of a few seconds. Because of this computational inexpensiveness, one can also use TGLF to simulate entire radial profiles, by performing multiple simulations for different radial positions. This is typically done by including TGLF in the framework of transport codes.

2.5.3 ASTRA

ASTRA (**A**utomated **S**ystem for **TR**ansport **A**nalysis) [36, 76] is the transport code that was used the most for the simulations in this thesis. In ASTRA, radial profiles computed from the magnetic axis to the plasma last closed flux surface – of quantities such as n_e, T_e and T_i as well as v_{tor} and q – are given as input, together with profiles of the injected power and a 2 D boundary for the magnetic equilibrium. With these inputs, ASTRA then calculates profiles of the transport coefficients. Here, the user can decide if these transport coefficients should be used to predictively evolve the profiles given initially as input, or if

the input profiles should be kept fixed, for example to perform a power balance analysis. While the transport equations in ASTRA are one dimensional, the equilibrium is calculated in two dimensions, solving the Grad-Shafranov equation. Due to this combination of one and two dimensional equations, ASTRA is often referred to as a 1.5 D code.

ASTRA allows the user to flexibly define which physics models and equations should be included in the simulations. An example for this is that one can describe the input heating power in the form of simple gaussian profiles, but it is also possible to include more sophisticated models such as TORBEAM or RABBIT, that can calculate how much heat is deposited, given the settings for the different heating systems and the state of the plasma. For the simulations conducted in the context of this thesis, the most important coupling is with the quasi-linear turbulence model TGLF. By combining TGLF with ASTRA, which calculates the evolution of entire profiles, it is possible to investigate effects that lead to local reductions of turbulent transport, by comparing the simulated profiles with the experimentally measured results.

2.5.4   TRANSP

Another transport code used for the investigations done for the work that is presented here is TRANSP [35]. Similar to ASTRA, TRANSP allows the user to include different models and equations for its simulations. One of the differences is which specific models are available for the two respective codes. The setup of TRANSP used in this work does for example not include TGLF or similar transport models that describe turbulence induced effects, making it of limited use in the direct study of how different parameters affect turbulent transport. TRANSP does, however, include a model that can describe the effects ICRF heating has on the plasma – TORIC [29]. With TORIC, it is not only possible to calculate how much heat is deposited to the ions and electrons, it allows also to calculate the properties of the fast ions that were created through the use of ICRF heating. Using the correct settings, TRANSP can also take the coupling between ICRF and NBI into account, where the ICRF further heats ions that were already accelerated from the NBI. Such a model for ICRF heating is at present not available for ASTRA. To still be able to use ASTRA to model experiments that make use of ICRF heating – which is the majority of the experiments conducted for this thesis – one can simply include results from TRANSP simulations. Information of the fast ions calculated with TRANSP, i.e. the parallel and perpendicular components of the temperatures of different fast ion species, are also used as input for gyrokinetic simulations done with GENE.

2.6   Open questions regarding locally reduced transport

In section 1.2, it was already mentioned that at ASDEX Upgrade experiments have been performed, that feature ion temperature gradients that are significantly larger than one
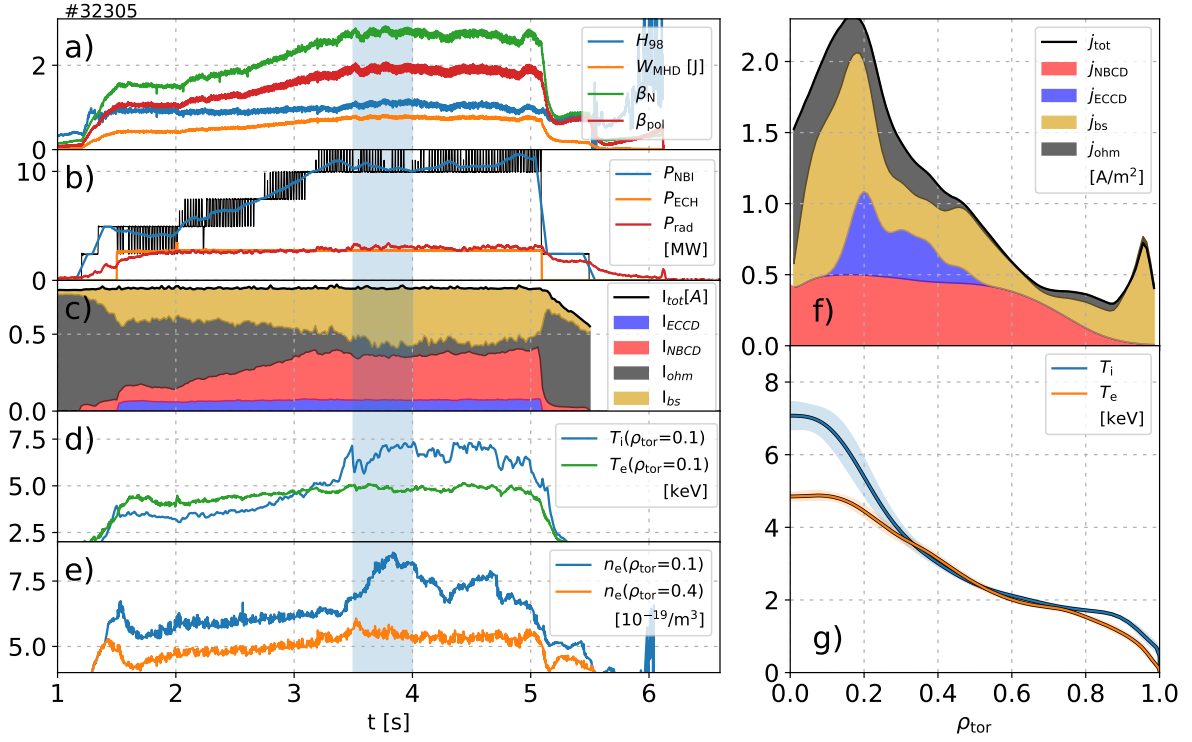
Figure 2.11: Left: Timetraces of key parameters of the AUG discharge #32305, including parameters quantifying the plasma performance (a), the power deposited by the different heating systems (b), the fraction of current contributed from the different current drive sources (c), the electron and ion temperature (d) and the electron density (e). Right: Profiles for the current density (f) and the temperatures (g) averaged over the time-interval shaded on the left-hand side.

would expect based on current theoretical understanding. An overview of such an experiment can be seen in figure 2.11 [11, 12].

This experiment – AUG discharge #32305 – not only features unexpectedly steep ion temperature gradients, it also achieves close to full non-inductive operation. This is very beneficial for fusion reactors, as it avoids several negative aspects connected with the pulsed operation tokamaks are typically run in: The reduced lifetime due to cyclic stresses on its components and a need to bridge the downtime between pulses, where no power is generated.

As can be seen in figure 2.11, about 90 % of the 800 kA plasma current is driven by non-inductive means. About half of this being contributed by the bootstrap current. Besides that, the scenario has an improved confinement of $H_{98} \gtrsim 1.1$, where

$$H_{98} = \frac{\tau_{\mathrm{E}}}{\tau_{\mathrm{E,scal}}} \tag{2.33}$$

is a measure of how good the confinement time τ_E is in comparison with an empiric scaling law based on a large database of discharges [77]. A $H_{98} > 1$ means the scenario exceeds the expectations.

Because of the multiple attractive features of this scenario, it would be worthwhile to further develop it and eventually extrapolate it to larger devices. For that, it is important to be able to reproduce it with reduced models such as TGLF. As was reported in [11], however, ASTRA/TGLF simulations significantly underestimate the core ion temperatures of this scenario. Consequently, this implies that the effects behind this observed local reduction of turbulent transport are not completely captured in TGLF. A study on the same scenario, using the gyrokinetic code GENE, came to the conclusion that nonlinear electromagnetic effects, as well as fast ions, play an important role in the correct capture of the reduced heat fluxes [13]. In that same study, also the safety-factor was found to be of importance.

Contrary to the results reported in [11], a later publication [78] finds a good agreement between TGLF simulations (using the framework code TGYRO) and the experimental profiles of the same discharge investigated in both [11] and [13]. In this later publication, the turbulence stabilization is attributed to a coupling between the ITG and subdominant modes, facilitated by a high thermal β, and favourable effects of the Shafranov-shift. Reasons why this newer TGLF simulations could match the experimental profiles while the older ones could not, include differences in the inputs used (most notably [78] includes fast ions while [11] does not) as well as differences in the setup, in particular between the framework codes ASTRA and TGYRO. The most important reason, however, is that [78] uses a newer version of TGLF, in which the rule how turbulence is suppressed by the $E{\times}B$-shear was updated, from the so-called *quench-rule* to the *spectral-shift-model* [75].

Using this new $E{\times}B$-rule and taking also the other differences into account, it is also possible to recover the experimental profiles of this particular discharge using ASTRA/TGLF. In these TGLF simulations, the saturation rule "SAT0" was used, along with the spectral-shift $E{\times}B$ rule. The input powers used in the simulation was calculated by TORBEAM in the case of ECRH and by TRANSP/NUBEAM in the case of NBI. Radiation losses were tomographically reconstructed from bolometric measurements. As initial conditions, an average over the experimental profiles in the steady-state interval between 3.5 and 4.0 seconds was used; The boundary outside $\rho_\mathrm{tor} = 0.75$ was constantly fixed to that value, as TGLF is not as reliable in the plasma edge. It was also found that it is necessary to keep the equilibrium fixed, similar to how it is done automatically in the TGYRO/TGLF simulations reported in [78]. To do this in ASTRA, which normally recalculates the equilibrium every time step, the variables "TE" and "TI" (T_e and T_i) were set to constant values, while instead additional auxiliary variables "F1" and "F2" were used to calculate the evolution of the temperature profiles. While F1 and F2 were used as inputs for the TGLF calculations, the fixed TE and TI still went into the calculation of the equilibrium, ensuring that it stays constant.

A systematic overview of how strong different effects contribute to the ion temperature
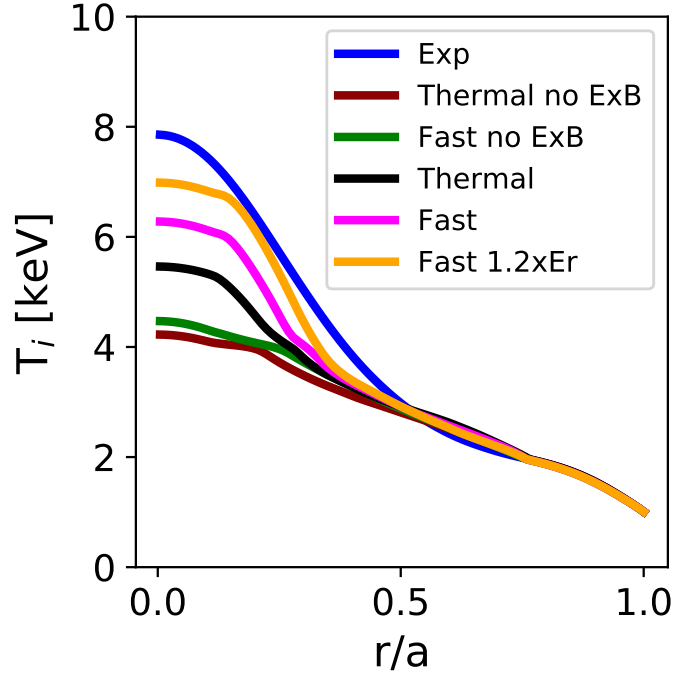
Figure 2.12: Ion temperature profiles resulting from TGLF simulations of the AUG discharge #32305, compared to the experimentally measured profile. Both the inputs of the simulation as well as the experimental profile are averages over the time interval 3.5-4.0 s. Simulations labelled "fast" include fast ions as a kinetic species and the contribution of fast ions to the total pressure. Simulations labelled "thermal" only include thermal ions. Simulations labelled "no $E \times B$" have the radial electric fields set to 0 and therefore do not include $E \times B$-shear effects; simulations without this label include $E \times B$ effects. The simulation labelled "Fast 1.2xEr" include fast ions combined with an increased $E \times B$-shear.

peaking in this numerical study is shown in figure 2.12. Several simulations were performed, covering all permutations of with/without $E \times B$-shear and fast ion effects. If the $E \times B$-shear is taken into account, then both the simulations using thermal ions only, as well as the one that additionally uses fast ions, yield peaked ion temperature profiles, though in the case with fast ions it is much more pronounced. Without the $E \times B$-shear, no profile peaking occurs, regardless whether fast ions were used or not. Additionally, the results of the simulations were found to depend sensitively on the precise value of the $E \times B$-shear. As can be seen in figure 2.12, changing the radial electric field E_r (and therefore the $E \times B$-shear) by 20 % has a significant effect on the resulting ion temperature profile.

An increase of 20 % might sound quite substantial, but in fact, this can be justified by relatively high values of poloidal rotation. Normally in these simulations, the poloidal rotation that goes into the radial electric field is neglected, or taken from neoclassical calculations. When instead taking the poloidal rotation from measurements, E_r can indeed
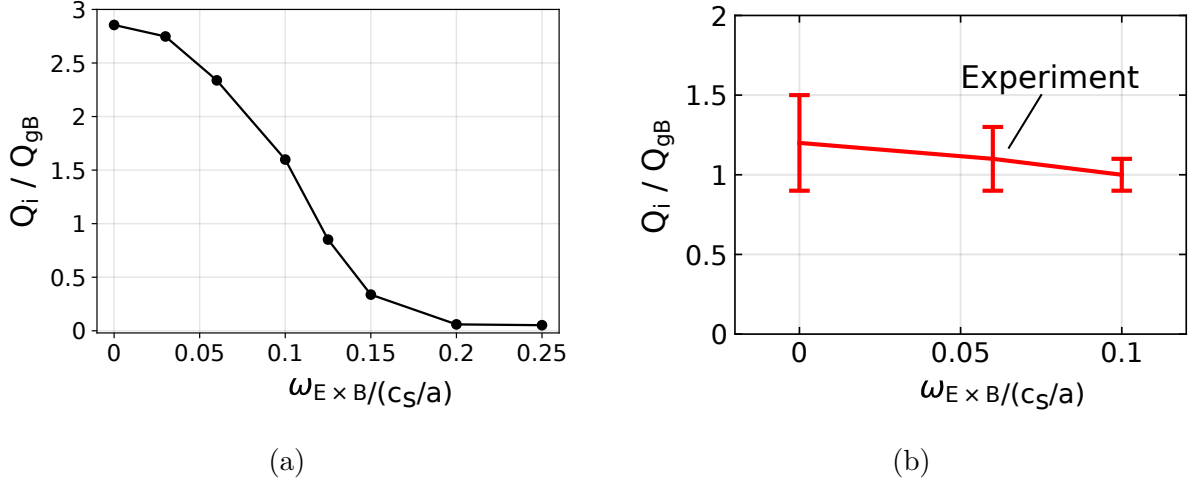
Figure 2.13: Dependence of the ion heat flux on the E×B-shear using TGLF standalone simulations (a) and nonlinear GENE simulations (b). In TGLF varying around the experimentally found E×B-shear of $\omega_{E \times B} = 0.06$ (indicated in (b)) strongly changes Q_i, whereas in GENE there is only a much smaller effect.

be increased by this much. For a more in-depth discussion on this, see chapter 4.1.

To further illustrate the strong dependence of the ion heat flux on the $E \times B$-shear $\omega_{E \times B}$, the results of a series of TGLF standalone simulations is shown in figure 2.13a. As can be seen, in the TGLF simulations using the spectral-shift model, this discharge lies in a point in parameter space where already small changes in $\omega_{E \times B}$ have a strong effect on the ion heat fluxes. Contrary to that, in GENE simulations using the same input values and doing a similar (albeit less extensive) parameter scan, the strong $\omega_{E \times B}$ dependency of the ion heat flux Q_i is not observed. This can be seen in figure 2.13b.

While it is in principle safe to assume that GENE is describing the situation more accurately, owed to the fact that it is much less simplified, the $E \times B$-shear is still considered an important factor in the formation of ITB and more generally the reduction of turbulent transport, as was discussed in section 2.4. It is therefore of great interest to experimentally confirm whether or not $\omega_{E \times B}$ plays an important role in the observed local reduction of turbulent transport in this particular non-inductive AUG scenario. And if the $E \times B$-shear does indeed turn out not to be responsible for the ion temperature peaking, what are then the key parameters?

To explore these questions, a series of experiments have been conducted at AUG, in which – starting from the scenario discussed in this section – a number of potentially important parameters have been varied. Besides the $E \times B$-shear, these parameters include the safety-factor q and magnetic shear s, the fast ion content and the thermal β. These experiments will be discussed in more depth in chapters 4 and 5. Before that, however, a brief overview of the systems that were used for these experiments is given in chapter 3.

3 Experimental Setup

All experiments discussed in this thesis were performed in the tokamak ASDEX Upgrade [79]. In this chapter, a brief overview of this machine is given, with an emphasis on the heating systems and the diagnostics relevant in the context of this work.

ASDEX (**A**xi**S**ymmetric **D**ivertor **EX**periment) Upgrade (AUG) is a medium sized tokamak, with a major radius of $R_0 = 1.65$ m and a minor radius of $a = 0.5$ m, located at the Max-Planck-Institute for Plasma Physics in Garching, Germany. A typical plasma discharge in AUG uses a toroidal magnetic field of 2.5 T, a plasma current I_p of up to 1 MA and lasts for up to 10 s. This time-limit applies also to completely non-inductive discharges, though for those cases the main limiting factor is that AUG lacks an active cooling system that would protect the machine from the excessive heat loads of longer
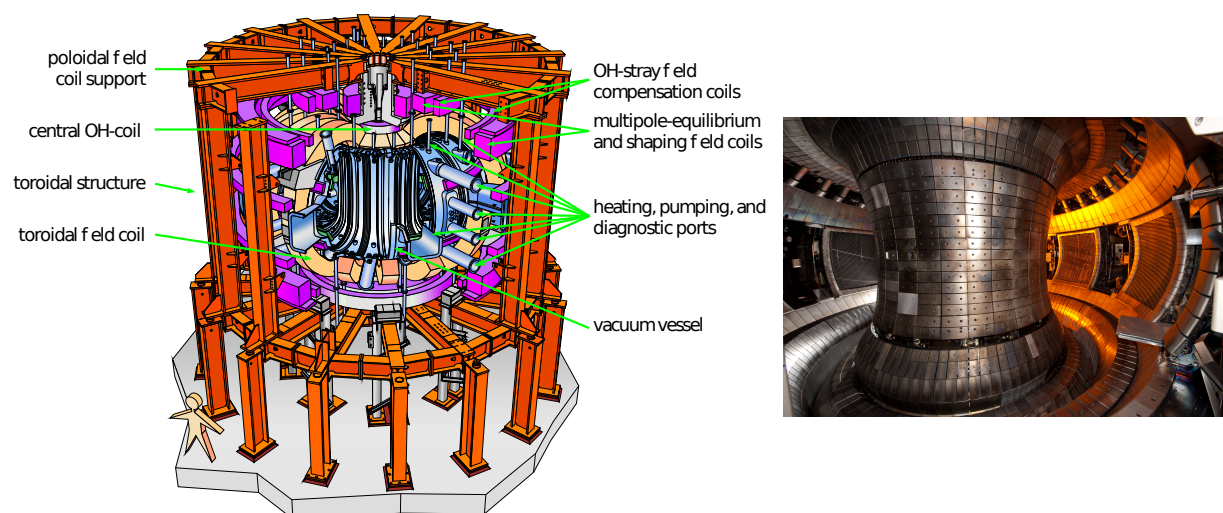

Figure 3.1: Left: CAD drawing of the tokamak ASDEX Upgrade, displaying the vacuum vessel and ports used for the various diagnostics and heating systems, poloidal and toroidal field coils used to control shape and position of the plasma, as well as the surrounding support structure. Right: Photograph of the interior of AUG; here, one can see the tungsten tiles making up the wall, as well as the lower divertor. [IPP database]

pulses. The density of the plasma inside AUG is typically between several 10^{19} and 10^{20} electrons per m^3, with temperatures in the core that can exceed $10\,\mathrm{keV}$. ASDEX Upgrade has been in operation since 1991, replacing its predecessor ASDEX (1980–1990), in which the H-mode regime was first discovered in 1982 [49].

As the "D" in its name suggests, one major focus of research at ASDEX Upgrade is to study and improve the divertor concept in a tokamak, which allows for operation with a reduced influx of impurities and more controllable power exhaust. In general, the physics program of AUG is geared towards aiding in the design and the preparation of operation of ITER.

One of AUG's distinguishing features is the fact that almost all the plasma facing components are made from tungsten, or are at least coated with it [80]. In many other MCF devices, plasma facing components are made from carbon. The advantages of tungsten over carbon are the significantly lower erosion rate and – perhaps more importantly – the fact that the hydrogen fuel is much less likely to bond with the wall material and be deposited in it. Considering that in a future power plant the radioactive hydrogen isotope tritium will be used, this ultimately is a showstopper for carbon. However, the fact that tungsten is an element with a very high atomic number of Z=74 leads to two problems: First, due to the quasi-neutrality of the plasma, one tungsten atom displaces a large number of hydrogen isotopes that can therefore not contribute to the fusion processes. And secondly, due to its high atomic number, tungsten is never fully ionized, which means it constantly radiates away power; If this radiation is too high, this can even lead to an early termination of the plasma. Because of these two issues, the concentration of tungsten must be kept at a very low level.

This is a particular challenge in scenarios that require low densities, for example to maximize the current drive efficiency – which was also the case in the experiments discussed in this work! To this end, so-called *boronisations* are regularly performed in AUG, where the vessel walls are coated with a layer of the low Z element boron. This significantly reduces the amount of impurities coming from the wall and, on the contrary, even leads to the walls pumping impurities away from the plasma [81].

3.1   Heating and Current Drive Systems

ASDEX Upgrade is equipped with powerful and flexible heating and current drive systems in the form of NBI, ECRH and ICRF. Combined, these three systems are able to provide up to approximately $30\,\mathrm{MW}$ of heating power. In section 2.2, an overview of how these different heating and current drive systems operate was already given; in this section, some technical details will be described, of how these systems are implemented in AUG [82].

The main amount of ASDEX Upgrade's heating power can be provided by the NBI system. In total, AUG has 8 beam sources that can each produce up to $2.5\,\mathrm{MW}$ of heating power, yielding a total of $20\,\mathrm{MW}$. These beams are produced in two neutral beam injectors –

referred to as boxes one and two – which are located at two opposing sides of the tokamak. The main difference between these two injectors is that box one has an acceleration voltage of up to 93 kV, while for box two it is only 60 kV. Between the eight different beams, there is some variety as to how they are oriented: Two beams are aimed almost completely radially, four are aimed more tangentially and two are aimed rather strongly off-axis (see figure 3.2). These last two beams are of particular importance in the context of this thesis as they provide a substantial amount of current drive (up to 300 kA) into the plasma. All of the NBI sources allow a rapid beam on/off modulation ($t_{\text{on}} + t_{\text{off}} = 25\,ms$), which can be used for a quasi-continuous variation of the beam power. With this, one can smoothly ramp up the power in the beginning of the discharge and adjust the exact power level via feedback control, to keep for example β_{pol} constant; Both of these techniques have been applied in this work. Besides their use as heat and current source, some NBI beams are also used as active diagnostic beams, used for example in the CXRS and IMSE systems (see section 3.2).
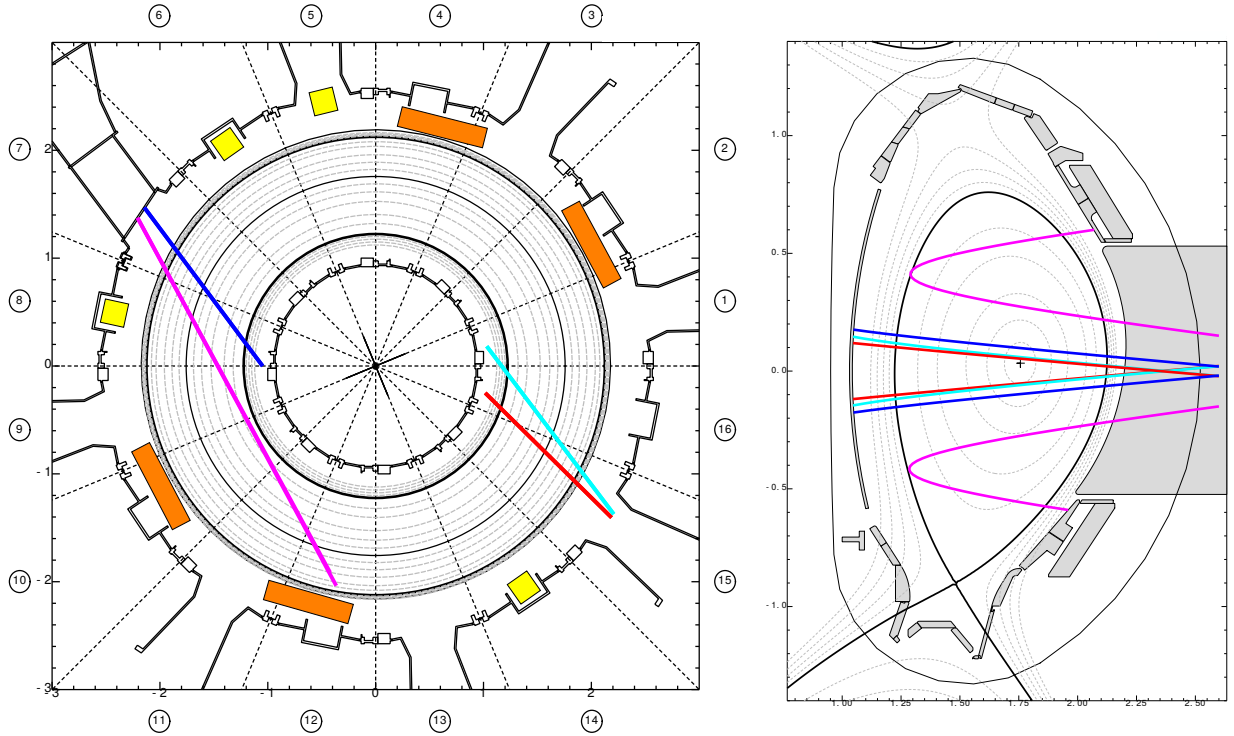

Figure 3.2: Overview of the positions of the different heating systems in AUG, shown from the top (left) and – in the case of the NBI – also the side (right). The coloured lines indicate trajectories of the 8 different NBI beams, which are aligned radially (red), tangentially (blue and cyan) and off-axis to drive current (magenta). The coloured boxes in the left figure indicate the ICRF antennas (orange) and the positions where the ECRH beams are directed into the plasma (yellow).

The ECRH system of AUG [83, 84] is capable of delivering up to 8 MW of heating power. The ECRH waves are produced in a total of eight *Gyrotrons* [85], which can each create a narrow microwave beam of up to 1 MW heating power – either at 105 GHz or 140 GHz. In the experiments discussed in this work, only 140 GHz X2-waves were used (2nd. harmonic extraordinary-mode). As the Gyrotrons are located outside the torus hall in which AUG is located, the waves are transmitted to the tokamak through both waveguides and quasi-optically via mirrors. These mirrors can be controlled to flexibly change their orientation, allowing a wide range of different deposition locations along the resonance. This is of particular use to shape the profile of the plasma current, for example to adjust the *q*-profile.

The ICRF heating system of AUG, finally, consists of four antennas inside the torus vessel, that can deliver a total of up to 6 MW of heating power. Compared to the ECRH, the area in the plasma that is heated by the ICRF waves is much broader. This is due to the fact that the ICRF antennas need to have a size in the range of $\sim 1\,\mathrm{m}$, because ICRF waves have much lower frequencies, in the range of several tens of MHz. As discussed in section 2.2.2, to deposit power, the ICRF antennas need to be located very close to the plasma. Due to this close proximity, the ICRF antennas tend to deposit tungsten impurities into the plasma when operated. This is because of stray electrical fields that affect the plasma such that the sputtering of the ICRF antenna limiter is increased. To mitigate this issue, two of the ICRF antennas were replaced in 2015 with new *3-strap antennas* that were optimized such that these electrical fields and the associated W sputtering are minimized [86]. For the remaining two older *2-strap antennas*, this issue is addressed by covering them with the low Z impurity boron.

3.2 Diagnostics

For an in-depth evaluation of the experiments conducted in AUG, it is equipped with a broad suite of diagnostics that allow to measure a large variety of different quantities. In this section, the most important ones in the context of this work will be briefly introduced. An overview of these various diagnostics and where they are located inside AUG can be seen in figure 3.3.

3.2.1 Magnetic Measurements

In order to reconstruct the magnetic equilibrium, numerical tools solving the Grad-Shafranov equation (eq. 2.5) require some knowledge of the magnetic field inside the torus as constraint. To this end, a number of magnetic coils is positioned around the AUG vessel. By integrating over the voltage U induced in the coils, it is possible to determine the poloidal flux ϕ, according to

$$U(t) = -\frac{\mathrm{d}\phi}{\mathrm{d}t} = -\frac{\mathrm{d}}{\mathrm{d}t}\left[\int \vec{B} \cdot \mathrm{d}\vec{A}\right]. \tag{3.1}$$
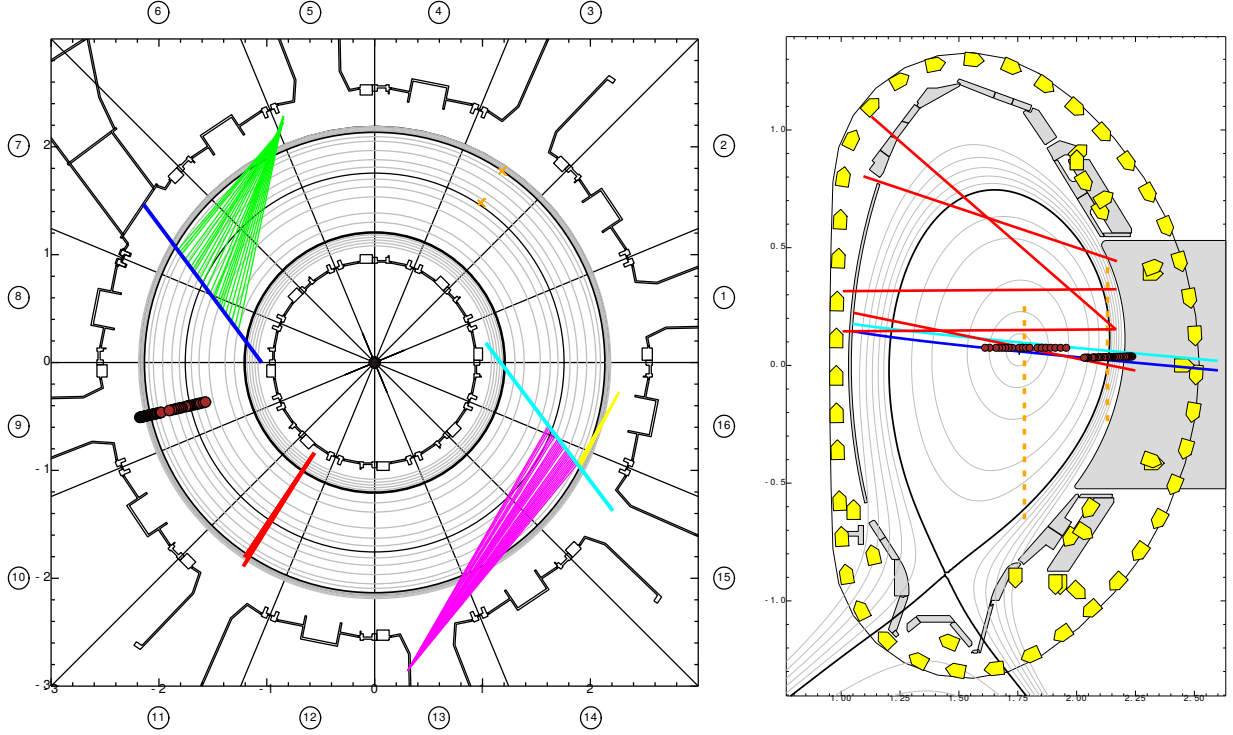
Figure 3.3: Overview of diagnostics used to monitor the plasma, both in toroidal (left) and poloidal (right) view. Shown here are the paths of the DCN- (red) and TS-lasers (orange), as well as the ECE diagnostic (brown). On the left, the different lines of sight of the CXRS systems are indicated (green, magenta and yellow), which look at NBI beams 3 (cyan) and 8 (blue). On the right, the coils used to measure the magnetic field are indicated with yellow boxes.

Due to the high sampling rate of 10 kHz, these coils can also pick up fast oscillations caused by rotating MHD-instabilities, such as *neoclassical tearing modes* (NTMs) [17]. In figure 3.3, an overview of the magnetic probes inside ASDEX Upgrade is given (yellow boxes, right).

3.2.2 DCN Interferometry and Polarimetry

The *Deuterium-Cyanide* (DCN) Laser is an important diagnostic tool in ASDEX Upgrade [87]. It allows not only to determine a line-integrated value of the electron density n_e via interferometry, it can also be used to determine a line-integrated value of the magnetic field B.

The measurement of n_e is done by determining the phase difference φ between a laser beam that has passed through the plasma, with a reference beam that has not, using

interferometry. This phase difference relates to the electron density according to

$$\varphi = \lambda_0 \frac{e^2}{4\pi\varepsilon_0 m_e c^2} \int n_e(x)\mathrm{d}x, \tag{3.2}$$

where $\lambda_0 = 195\,\mu\mathrm{m}$ is the vacuum-wavelength of the laser and x is a coordinate along its line of sight. In AUG, five beams with different lines of sight are used, which allows also for a reconstruction of density profiles. In figure 3.3, the paths of the DCN lasers are indicated by the red lines.

By taking advantage of the fact that linearly polarized light travelling parallel to a magnetic field undergoes a rotation of the plane of polarization – the so-called *Faraday rotation* – the DCN laser can also be used to obtain information about the direction of the magnetic field lines. This is done by decoupling light from the beam used for the density measurements, using a mirror, and then measuring it's direction of polarization by having a rotating polarizer in front of a detector. From the fact that the amount of faraday rotation is proportional to $n_e \cdot B_\parallel$ – i.e. the product of the electron density and the component of the magnetic field parallel to the laser-beam – a line-integrated value of $B_\parallel$ can be obtained [88]. This can be used as an additional constraint in the equilibrium reconstruction, allowing also to reduce the uncertainty of the q-profile.

3.2.3 Electron Cyclotron Emission

By measuring *Electron Cyclotron Emissions* (ECE), it is possible to determine the electron temperature T_e. These measurements are done with a *heterodyne radiometer* [89]. The underlying principle behind the ECE diagnostic is essentially the reverse process of the ECRH system: As the electrons gyrate arond the magnetic field lines, they emit radiation at harmonic frequencies of the cyclotron frequency $\omega = n \cdot \frac{eB}{m_e}$. Since the strength of the magnetic field decreases with $1/R$, it is possible to determine the radial position of an emitted wave from the measured frequency. According to the *Rayleigh Jeans approximation* of the black body radiation, it is then possible to obtain T_e at that position from the intensity of the black body radiation I_{BB}:

$$T_e \approx \frac{8\pi^3 c^3}{\omega^2} I_{BB} \tag{3.3}$$

This, however, only holds if the plasma is *optically thick*, i.e. the density is high enough such that all radiation emitted in the plasma is reabsorbed again several times, before it leaves the plasma in the form of black body radiation. At least in the core of the plasma, this condition is generally fulfilled.

The ECE system installed in AUG has 60 channels that are sampled with a frequency of $1\,\mathrm{MHz}$ and is set up such that for the typical magnetic field of $2.5\,\mathrm{T}$, the resonance positions cover in principle the entire radial range (figure 3.3, brown dots). The relative accuracy

of its temperature measurements is around 7 %, with a spacial resolution of approximately 1 cm [90, 91].

3.2.4 Thomson Scattering

For *Thomson Scattering* (TS) measurements [92], light from neodymium-doped aluminium garnet (Nd-YAG) lasers is sent vertically through the plasma at two radial locations: One at the edge, one in the core (see figure 3.3, orange lines). This light is then partially scattered on electrons in the plasma and observed in several detectors with lines of sight perpendicular to these laser beams. Looking at the spectrum of the light observed in the detector, it is possible to infer several properties of the electrons at which it was scattered: First, T_e can be calculated from the doppler broadening – assuming a maxwellian distribution; And secondly, from the intensity of the light, n_e can be found out. Compared to the ECE system, the time resolution of the TS system is much lower, as it is restricted by the repetition rate of the lasers, wich is 20 Hz. For the core system, four and for the edge system six Nd-YAG lasers are used, giving a time-resolution of 80 Hz and 120 Hz for core and edge respectively. The spatial resolution of the TS system is 25 mm in the core and 3 mm in the edge.

3.2.5 Charge Exchange Recombination Spectroscopy

Charge Exchange Recombination Spectroscopy (CXRS) is a powerful diagnostic technique that allows the temperature, rotation and densities of impurities in the plasma to be measured [93]. The principle behind beam-based CXRS is the following: Neutral atoms from the NBI heating system (usually D atoms) interact with impurities (I) in the plasma, transferring their charge in the process. Following that, the impurities are briefly in an excited state, before relaxing back into their ground state through a number of intermediate steps:

$$I^{Z+} + D^0 \rightarrow I^{(Z-1)+*} + D^+ \rightarrow I^{(Z-1)+} + D^+ + h\nu \tag{3.4}$$
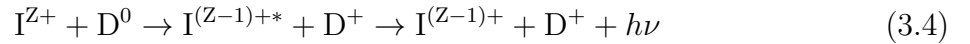
The light emitted during these transitions is then detected and analyzed in spectrometers. Similar to the TS system, one can then determine the temperature of the impurity ions from the Doppler broadening, and the impurity density from the intensity of the spectral lines. Additionally, from the Doppler shift of the spectral lines, it is also possible to obtain the projection of the impurity rotation along the line of sight (LOS) of the diagnostic. Thus, with toroidally viewing LOS, it is possible to measure the toroidal rotation velocity v_{tor}.

While CXRS measurements are also possible on the main ion species, the interpretation of the spectra is more complicated compared to impurity CXRS. Main ion CXRS is therefore not routinely available at AUG. However, it can generally be assumed that all thermal ion species are in equilibrium with each other, meaning that T_i of the impurity species is the

same as for the main ion species. Also the rotation of the impurities can be approximated to be the same as that of the main ions, as the impurities are expected to be dragged along by the main ion flow. Due to friction, however, the impurity rotation is slightly lower. To take this into account, the rotation measured on impurity species can be corrected with neoclassical calculations that are for example carried out with TRANSP.

The main ion density can obviously not be equated directly with the impurity density. However, from quasi-neutrality it is possible to calculate the main ion density, if the densities of all impurity species are known. Under the assumption that the main ion species is a hydrogen isotope (Z=1) and only one impurity species exists in non-negligible amounts, one can calculate the main ion density n_i with the following formula:

$$n_i = n_e \cdot \frac{Z_{eff} - Z_{imp}}{1 - Z_{imp}}. \tag{3.5}$$

Here, Z_{eff} is the *effective ion charge* [94], defined as

$$Z_{eff} = \frac{\sum_s n_s Z_s^2}{n_e}, \tag{3.6}$$

where s denotes the different impurity species.

To obtain good CXRS data, depending on the machine conditions and the specific settings of the plasma discharge it may be necessary to purposely introduce an impurity species into the plasma, for example via a gas puff. For the experiments conducted for this thesis, this was not necessary, due to the fact that they were always conducted shortly after a boronisation, which means they have a sufficiently high concentration of the impurity boron.

In ASDEX Upgrade, several CXRS systems are installed with lines of sight pointed at two different NBI beams. In figure 3.3, the lines of sight of the three core systems [93, 95] (green, magenta) and the faster edge system [96] (yellow) are indicated. The core systems have a radial resolution of ± 2.5 cm and usually operate at an integration time of 10 ms, but values as low as 3.5 ms are also possible. One of these two core systems has LOS that cover both HFS and LFS. From asymmetries in v_{tor} between HFS and LFS, the poloidal rotation v_{pol} can be inferred. This will be discussed in more detail in chapter 4.1 [95].

For the edge system, very low integration times down to 10 µs are possible, but for the experiments discussed in this work, this system could not be used as the wall clearance of the plasma was typically too large, such that the edge CXRS LOS were viewing outside of the plasma. However, before the 2021 experimental campaign of AUG, a new optical head was added to one of the core systems, that allows for edge data to be measured also in experiments with high wall clearance.

3.2.6 Imaging Motional Stark Effect Polarimetry

Motional Stark effect (MSE) polarimetry is a commonly used technique to obtain information about the plasma equilibrium in the core and, connected to that, about the current density and safety factor profiles [97]. In the following, a brief overview of the principle behind MSE diagnostics in general and the *imaging MSE* (IMSE) at AUG in particular is given:

Similar to the CXRS system, the MSE relies on neutrals that are sent into the plasma with a NBI source. As these neutrals collide with the particles in the plasma, they sometimes are temporarily put into an excited state before relaxing back to the ground state by emitting light. If this light is detected such that the NBI beam and the detector lines of sight are not orthogonal to each other, it can be separated from the emissions of the bulk plasma, as the light from the excited beam neutrals will be doppler-shifted.

This can be seen in figure 3.4, where an example for such a MSE spectrum is shown. Here, the light emitted from the beam neutrals is shifted to shorter wavelengths between 653 nm and 655 nm, whereas the light emitted from the bulk plasma remains centered around the *Balmer-α-line* at 656 nm ($n = 3 \rightarrow 2$). Unlike the bulk plasma emissions, the emissions from the beam neutrals are split into several separate spectral lines. This is caused by the
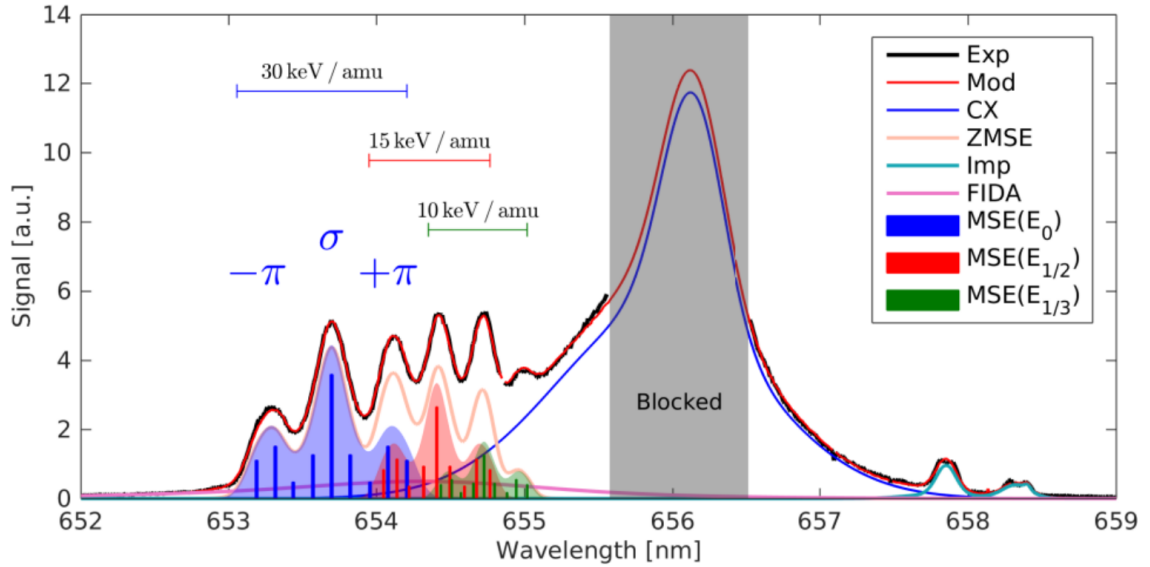

Figure 3.4: Example of an MSE spectrum. The nine doppler-shifted Stark-splitted spectral lines are highlighted in blue, to the left of the broader D-α line at 656 nm. Additionally, spectral lines from beam neutrals at half and third energy (coming from D_2 and D_3 molecules) are highlighted in red and green, respectively. Each of these groups of nine spectral lines consists of thee σ-lines, flanked by three π-lines on either side. Figure reproduced from [98].

Stark Effect resulting from the electric field $\vec{E} = \vec{v} \times \vec{B}$ the beam neutrals experience in their rest frame as they move through the magnetic field – along with any background electric field $\vec{E}_0$. Of the nine spectral lines the D-α transition is split into, three are linearly polarized when observed perpendicular to $\vec{E}$ (corresponding to Δm=0), six are linearly polarized parallel to $\vec{E}$ (corresponding to Δm=$\pm$1). According to the German words for perpendicular ("senkrecht") and parallel ("parallel"), these lines are typically denoted with σ and π.

By measuring the direction of the polarization of the σ and π lines, it is possible to determine the projection of $\vec{E}$ (and therefore also $\vec{B}$) onto the plane perpendicular to the line of sight. In doing this, it is important to take the background electrical field $\vec{E}_0$ into account. In the MSE systems in AUG, this is approximated by the contributions from v_{tor} to the radial electric field and the diamagnetic term proportional to the pressure gradients, $E_{\text{r}} \approx v_{\text{tor}} B_{\text{pol}} + E_{\text{dia}}$. The contributions from v_{pol} are neglected [22]. From the distance between the individual spectral lines, one can also determine the strength of the field, as a stronger electric field results in a larger split.

A technical challenge of this technique is that normally the σ and π components would interfere with each other, losing the information about their individual polarization directions. This necessitates the use of narrow interference filters that select only one of the two components. As this means that every line of sight requires a separate detector with its own interference filter, the number of channels in a normal MSE diagnostics is limited. This issue is addressed with IMSE systems, which allow significantly more data to be collected. The principle behind this diagnostic is the following:

Instead of detecting individual lines of sight, IMSE diagnostics capture an entire 2D image of the trajectory of a neutral beam. With a set of birefringent plates and polarizers, an interference pattern is created that encodes information about both position and polarisation. This is done in such a way that the σ and π components don't destructively interfere with each other, removing the need for narrow spectral filters, allowing the use of all the available light. Because of the fact that IMSE provides information for every spot of a 2D image (with a spatial resolution of 1–5 cm), a large quantity of data is collected, providing very strong constraints for equilibrium reconstruction codes [99, 100].

In AUG, the optical relay system is arranged such that its field of view is aligned very well with NBI source 8, one of the tangential beams of beam box 2. When measuring with this beam, the core of the plasma is well covered, both on high- and low-field-side. It is, however, also possible to make measurements with NBI source 7, one of the off-axis beams. In that case, less data is available, and in particular not in the very core, as the trajectory of source 7 is not as well aligned with the field of view of the camera and does not go exactly through the core. In figure 3.5, a comparison of the coverage using source 7 or 8 is shown. In principle also measurements with the other tangential beam – source 5 – are possible, though the overlap between beam and camera field of view is only very small, resulting in much poorer data compared to the other two sources. As the signals from the
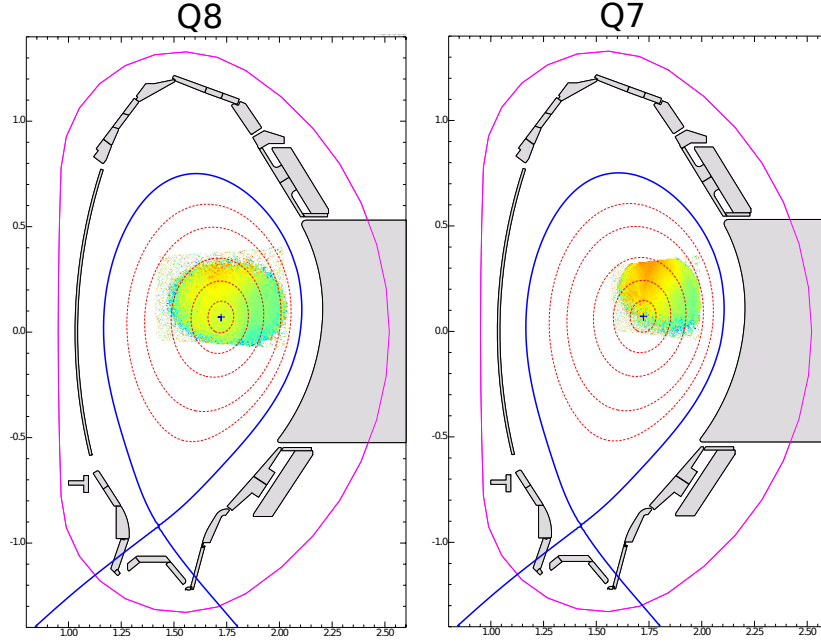
Figure 3.5: Spatial coverage of IMSE measurements when using NBI source 7 (right) or source 8 (left).

different beams interfere with each other, IMSE data can only be collected if exactly one of these three beam sources is active.

A particular challenge of the IMSE system is to obtain a good calibration of the data. While the measurement uncertainty of the field line angles are very small, the absolute value is not known at first. As an absolute calibration of the IMSE diagnostic at AUG is technically challenging and can at present not be done, it is necessary to individually shift the signals for each channel, subtracting an arbitrary offset. These offsets can be determined by using an equilibrium solver to forward model the angles the IMSE diagnostic would measure, if it was absolutely calibrated, and then subtract that from the angles that were actually measured. This of course can only be done if the real equilibrium – or rather the distribution of current – is known with certainty. As was described in section 2.1, one can use phases with sawtooth crashes to this end, as the redistribution of current during a sawtooth crash is reasonably well understood. In the context of this thesis, this calibration method is problematic as the discharges under investigation were specifically designed to have a q above unity – amongst other things to avoid sawtooth crashes. For a majority of the experiments discussed in this thesis, it is therefore not possible to determine the offset of the angle directly. Instead, the IMSE data was calibrated using offsets from other discharges. This will be discussed in more detail in section 3.2.7.

3.2.7 Integrated Data Analysis tools

Between the various diagnostics introduced in the previous sections, there is a certain amount of overlap and redundancy. For example T_e can be measured both with the ECE and the TS diagnostics, while T_i is measured with several CXRS systems that partially cover the same spatial locations. Combining all available data for a given quantity allows for an improved spatial and temporal resolution, as well as an increase in reliability by finding and correcting outliers and inconsistencies. At AUG, a number of sophisticated tools is used for this task, providing a coherent combination of data for parameters such as temperature, density and rotation, but also the effective ion charge and the magnetic equilibrium. In the following, a brief overview of these various programs is given.

IDA

With IDA, the data measured via ECE, TS, DCN and *lithium beam impact excitation spectroscopy* is combined to obtain T_e and n_e profiles [101]. The latter of these four diagnostics, the lithium beam, provides edge data for n_e. Further information on this diagnostic can be found in reference [102].

After mapping all the data onto a common (magnetic) coordinate system, IDA combines this with forward modelling of the different diagnostics. In this forward modelling, one can for example correct for the so-called *shine-through* in the ECE data, in which radiation is attributed to a different location than the cold resonance position, due to the plasma
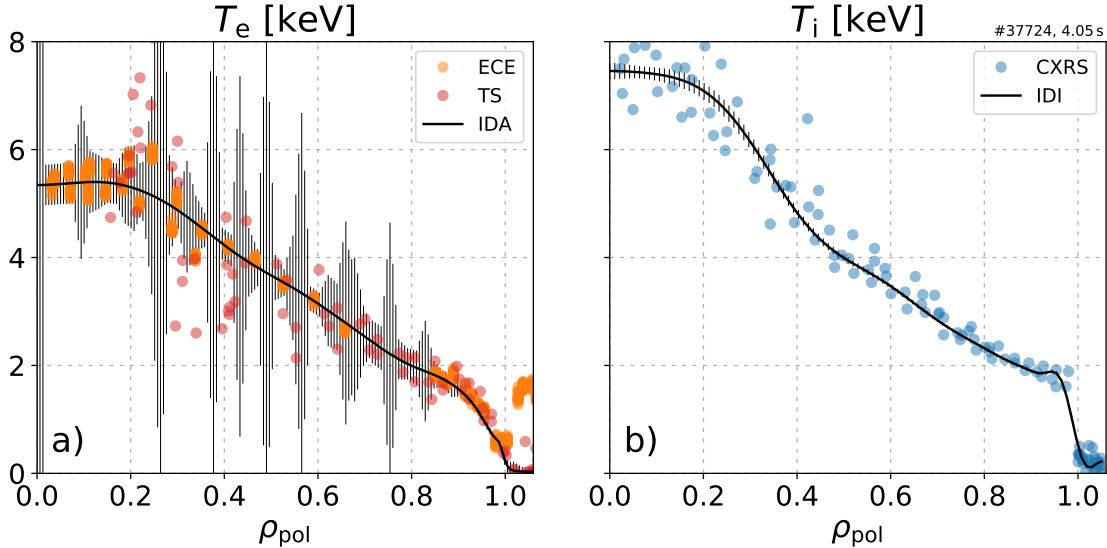

Figure 3.6: Example of a) a T_e profile calculated with IDA and b) a T_i profile obtained with IDI, based on the AUG discharge #37724 at 4.05 s. Coloured dots represent the measured data the profiles are based on, vertical lines indicate the uncertainties.

not being optically thick [91]. Together with additional constraints on things such as smoothness and monotonicity, combined profiles and an estimate of their uncertainties are calculated using a *Bayesian probability approach*. An example of a profile calculated with IDA is shown in figure 3.6 a), along with the experimental data it is based on.

IDZ

Using the same Bayesian approach as IDA, IDZ calculates the effective ion charge Z_{eff} [94]. As described in section 3.2.5, Z_{eff} can be calculated from the impurity densities as measured with CXRS. Using the IDA approach, this impurity data can be combined with measurements of the bremsstrahlung, which depends on Z_{eff} as well as T_{e} and n_{e}. As the later two parameters are ideally first calculated with IDA, IDZ is typically ran in tandem with IDA.

IDI

Using IDI, it is possible to combine the data of the different CXRS systems installed at AUG, to estimate the profiles for T_{i} and v_{tor}, as well as their gradients [103]. This is done by using *Gaussian Process Regression* (GPR) to fit the data. GPR is a commonly used technique to find a good fit through a distribution of data, that can be applied under the assumption that the noise on the data follows a Gaussian distribution. As with IDA, IDI can be further constrained with prior knowledge, such as that the profiles need to have a zero gradient in the plasma core. In figure 3.6 b), an example IDI T_{i} profile is shown, along with the underlying data.

To fit the impurity density n_{imp}, the python package *GPR1D* [104] has been used, as n_{imp} has not yet been included in IDI. Like IDI, this package is based on a GPR approach.

IDE

For tools like the ones introduced in the previous sections, where different datasets need to be aligned and mapped onto a common coordinate system, it is important to have a reliable reconstruction of the plasma equilibrium. As established in section 2.1, the plasma equilibrium can be described by the Grad-Shafranov equation (GSE, see eq. 2.5), which typically needs to be solved using numerical tools. At AUG, two such tools are used: For a quick first estimate shortly after the plasma discharge was performed, the CLISTE (**C**omp**L**ete **I**nterpretative **S**uite for **T**okamak **E**quilibria) code is used, which solves the GSE under the constraint that a least squares fit to magnetic measurements is obtained [105]. For investigations where one for example is interested in studying effects from small variations of the safety-factor and magnetic shear – particularly in the core – the code IDE was developed [106].

As is the case with CLISTE, GSE equilibrium solver often have only magnetic measurements available as constraint. As magnetic measurements are not suitable to obtain reliable

estimates of the core magnetic equilibrium quantities, the equilibrium reconstruction problem becomes ill-posed. This issue is often tackled by imposing additional constraints, for example on the smoothness of the current distribution profile. This, however, results in profiles with little physical basis that rely heavily on the regularization conditions chosen. IDE alleviates this problem by using pressure profiles (calculated from IDA, IDZ, IDI and RABBIT results) and modelling results as additional constraints. In particular, IDE couples its GSE solver with solutions to the *current diffusion equation* (CDE)

$$\sigma_\parallel \frac{\partial \psi}{\partial t} = \frac{R_0 J^2}{\mu_0 \rho} \frac{\partial}{\partial \rho} \left(\frac{G_2}{J} \frac{\partial \psi}{\partial \rho} \right) - \frac{V'}{2\pi\rho}(j_{\mathrm{BS}} + j_{\mathrm{CD}}), \tag{3.7}$$

which describes how a given distribution of the plasma current evolves over time. In this equation, $\sigma_\parallel$ is the parallel conductivity, J is related to the poloidal current and G_2 and V' are geometric factors. The quantities j_{BS} and j_{CD} are the bootstrap current and the current driven by external sources, respectively [106].
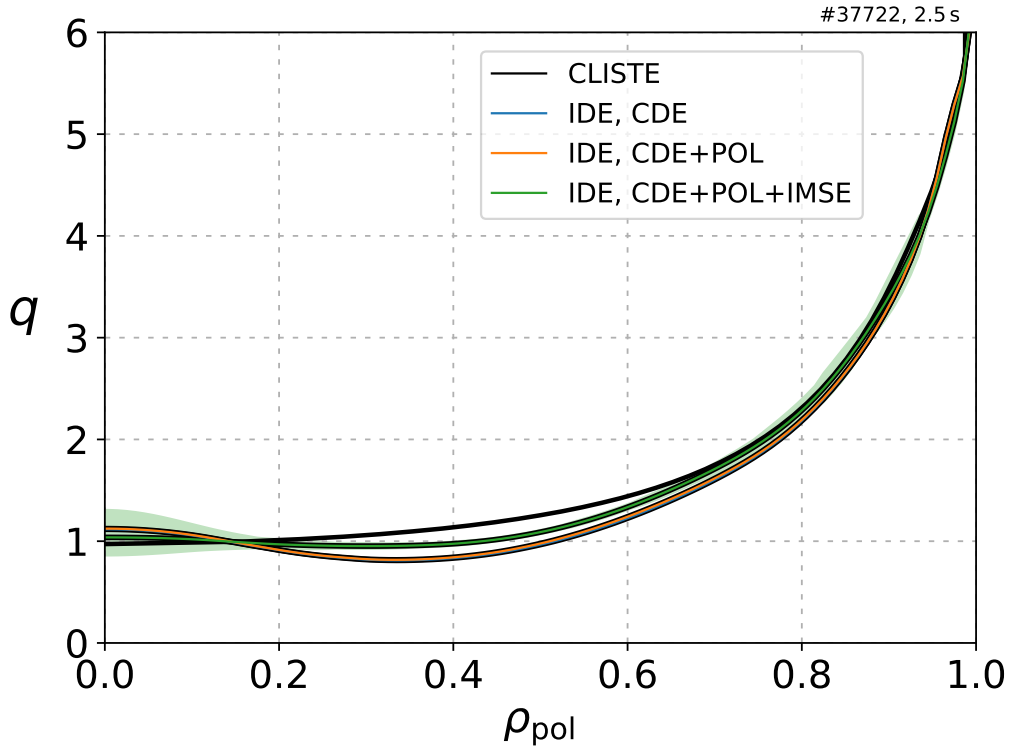

Figure 3.7: Safety-factor q calculated with IDE, taking progressively more experimental data as constraints. When IMSE and DCN polarimetry (POL) data is included, the uncertainty is significantly lower than for the profile that includes only POL, which in turn has a much lower uncertainty than the profile just based on the CDE. For comparison, also the profile calculated with CLISTE is shown.

The coupling between GSE and CDE is done every time step, iteratively. In other words, for each timepoint, the GSE is solved, considering all available measured data as constraints. The equilibrium and current distribution obtained this way is then fed into a CDE solver, providing a new current distribution which can then be taken as an additional constraint for the GSE at the following time step.

Depending on from which diagnostics data is available, the uncertainty of the profiles calculated with the GSE solver can be greatly reduced. In figure 3.7, a comparison of different q-profiles is shown, taking also data from the IMSE and/or the DCN polarimetry (POL) into account, which allow for the greatest constraints of the profiles. As can be seen, the variation between the profiles themselves is relatively small, but depending on what diagnostics are included, the uncertainties vary significantly. This is because the uncertainties shown here are only based on the measurement uncertainties from the diagnostics that were included in the equilibrium reconstruction. In areas where no such data is available, the uncertainty provided by IDE is therefore infinitely large. Consequently, for accurate and dependable core values of the q-profile, it is very beneficial to have IMSE data available.

The reason why the output from the CDE solver is not included in the uncertainty estimation is that it can't always be guaranteed that the current distribution behaves according to neoclassical theory. In the presence of MHD-modes, a redistribution of current can occur that cannot be described by the CDE. A notable example is the so-called *magnetic flux-pumping* where a 3/2 or 1/1 mode broadens a centrally peaked current-profile, resulting in a q-profile that is clamped around unity in the core [107, 108]. Another example, that is perhaps more common, is the sawtooth instability.

As was already established in section 2.1, sawtooth oscillations result in a periodic redistribution of current inside the $q=1$ surface. In order for IDE to be able to correctly describe plasma discharges where sawteeth occur, it needs to include a model that can accurately describe this redistribution of current. One of the first such models to be widely accepted was proposed by Kadomtsev in 1975, which assumes a sudden, complete reconnection of magnetic field lines within and around the $q=1$ surface, triggered by a 1/1-mode [20]. This model was, however, later found to be in contradiction with experimental evidence, as it incorrectly predicts q to be equal or larger than one, everywhere in the plasma right after the sawtooth crash [21]. In IDE, one can choose between several sawtooth models, including the Kadomtsev model, but in general the so-called *Flat-current model* (FCM) is used, which imposes a flattening of the current profile within $q=1$, while keeping the total current constant [22]. This model was found to be in good agreement with experimental data. By providing IDE with a list of time-points at which sawtooth crashes occur – determined either on ECE or Soft X-ray emission measurements [109] – one can therefore make the assumption that the current distribution at these times is known with relatively high certainty. As was already stated in section 3.2.6, one can make use of this fact to perform a calibration of the IMSE diagnostic:

Whenever IDE calculates a plasma equilibrium, it also conducts a forward modeling of what the measurements from diagnostics, whose data were used as constraints, should
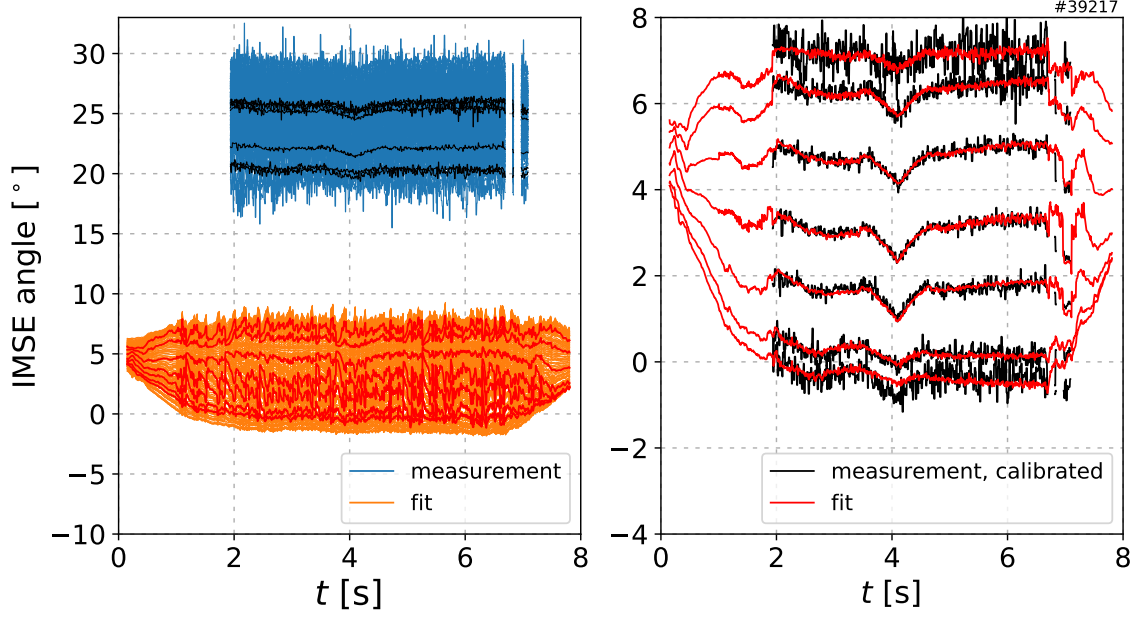
Figure 3.8: Left: Measured IMSE angles (blue) compared to ones provided by forward modelling (orange). A significant offset in the order of $\sim 20°$ is evident. Note that a large part of this offset stems from geometrical effects that could in principle be calculated and subtracted. These effects are instead corrected as part of the offset calibration, as the remaining uncertainties make it necessary anyways. Right: Same comparison, but now the measured angles are calibrated by subtracting the offset. For better visualization, only 7 out of the 146 usable IMSE channels are displayed. This subset of channels is highlighted in black and red also in the left plot.

look like for this equilibrium. It then uses this information to optimize the equilibrium such that the difference between the real and the modelled measurements is minimized. For the IMSE, the angle γ of the field lines is calculated with the following equation [22]:

$$\tan(\gamma) = \frac{A_1 B_{\mathrm{r}} + A_2 B_{\mathrm{t}} + A_3 B_{\mathrm{z}} + A_4 \widetilde{E}_{\mathrm{r}} + A_5 \widetilde{E}_{\mathrm{z}}}{A_6 B_{\mathrm{r}} + A_7 B_{\mathrm{t}} + A_8 B_{\mathrm{z}} + A_9 \widetilde{E}_{\mathrm{r}} + A_{10} \widetilde{E}_{\mathrm{z}}} \tag{3.8}$$

Here, B_{r}, B_{z} and B_{t} are the radial, vertical and toroidal components of the magnetic field $\vec{B}$, while A_1–A_{10} are geometrical coefficients. $\widetilde{E}_{\mathrm{r}}$ and $\widetilde{E}_{\mathrm{z}}$ are defined as

$$\begin{aligned}
\widetilde{E}_{\mathrm{r}} &:= \left(E_{\mathrm{r,dia}} - v_{\mathrm{tor}} B_{\mathrm{z}}\right)\big/ v_{\mathrm{beam}} \quad ; \quad E_{\mathrm{r,dia}} := \frac{\mathrm{d}p_{\mathrm{imp}}\big/\mathrm{d}r}{Z_{\mathrm{imp}} e n_{\mathrm{imp}}} \\[2mm]
\widetilde{E}_{\mathrm{z}} &:= \left(E_{\mathrm{z,dia}} + v_{\mathrm{tor}} B_{\mathrm{r}}\right)\big/ v_{\mathrm{beam}} \quad ; \quad E_{\mathrm{z,dia}} := \frac{\mathrm{d}p_{\mathrm{imp}}\big/\mathrm{d}z}{Z_{\mathrm{imp}} e n_{\mathrm{imp}}}
\end{aligned} \tag{3.9}$$

where $E_{\mathrm{r,dia}}$ and $E_{\mathrm{z,dia}}$ are the radial and vertical diamagnetic electric fields and v_{beam} is the velocity of the neutral beam particles, which is approximately $v_{\mathrm{beam}} = 3 \cdot 10^6 \, \mathrm{ms^{-1}}$ for the NBI beams used for IMSE measurements. As was already stated in section 3.2.6, the contribution from v_{pol} is neglected in equations 3.8 and 3.9. In general, this is justified as the poloidal rotation in AUG is typically well below $1 \, \mathrm{km/s}$ [110], resulting in corrections in the IMSE angles below the resolution of the IMSE. As will be discussed in chapter 4.1, in the experiments conducted over the course of this thesis the peak v_{pol} is typically higher – of the order of $\sim 5 \, \mathrm{km/s}$. Despite this, the approximation of neglecting v_{pol} is still justified; This is discussed in appendix A.

The general procedure to determine the offsets is now as follows: First, one simply runs IDE without using the IMSE data as a constraint, but still having the forward modelling of the expected IMSE angles active. Next, one selects a time interval where the plasma discharge features sawtooth oscillations – i.e. where the equilibrium can be assumed to be known reasonably well – and calculates the difference between the modelled angles and the ones that were actually measured. The offset, finally, is then simply the average over this difference – calculated for each channel separately. In figure 3.8, uncalibrated and calibrated IMSE data are shown, compared to the output of the forward model.

In the discharge depicted in that figure, determining the IMSE offset was relatively easy, since IMSE data was available for the majority of its duration, and sawteeth oscillations could be observed throughout that time. In the experiments performed for this work, the latter is generally not the case since the q-profiles are designed to be above unity. To calibrate the IMSE data, it is therefore necessary to use the offsets determined on other discharges. For IMSE measurements obtained with NBI source 8, a large database of discharges exist for which the offset was determined, allowing a reliable calibration; For measurements obtained with source 7, only two such discharges exist in the relevant experimental campaign, whose offsets deviate significantly from each other. As this discrepancy could not be resolved, the profiles based on NBI source 7 IMSE data need to be carefully discussed. For further details on these and other challenges in calibrating the IMSE data, see appendix A.

4 Effect of ExB-shear on R/LTi

In section 2.6, the question was raised which parameters are responsible for the local reduction of turbulent transport observed in a non-inductive scenario run in AUG – which is an attractive basis for a scenario that could be run in future fusion power-plants. A candidate of interest was the $E{\times}B$-shear, which was found to play an important role in simulations done with the reduced transport model TGLF; though that dependence could not be found using the more powerful code GENE.

In this chapter, in section 4.2, experiments will be discussed in which the $E{\times}B$-shear has been systematically varied, to study if and how this affects the ion temperature profiles. This variation in $\omega_{E{\times}B}$ is achieved by partially replacing NBI with ICRF heating during the discharge. This way, the torque put into the plasma is reduced, leading to a smaller toroidal rotation – the main contributor to E_r (and therefore also the $E{\times}B$-shear) in the core. However, at the same time this also leads to an increase in fast ion pressure, which needs to be considered as well for the evaluation of these experiments. To disentangle these potentially competing effects, non-linear GENE simulations are performed, allowing the possibility to change exactly one parameter at a time, while keeping everything else fixed. These simulations are discussed in section 4.3. Before that, in section 4.1, it is discussed how the different terms that can have a contribution to E_r (and therefore $\omega_{E{\times}B}$) are determined.

4.1 Terms contributing to the radial electric field

In section 2.4.1, it was introduced that there are three terms contributing to the radial electric field E_r, proportional to the toroidal and poloidal rotation v_tor and v_pol, and the impurity pressure $p_\mathrm{imp} = T_\mathrm{imp} \cdot n_\mathrm{imp}$ (see equation 2.30). In this section, challenges in obtaining and evaluating the data required for each of these terms are discussed, as well as how much each term contributes to the total value of E_r.

In principle all the required data – v_tor, v_pol, T_imp and n_imp – can be obtained using charge exchange recombination spectroscopy (see section 3.2.5). In the case of n_imp, it is important to have a smooth fit through the measured data, since it is actually the gradient that goes into the calculation of E_r. For the other parameters measured with CXRS, such fits are

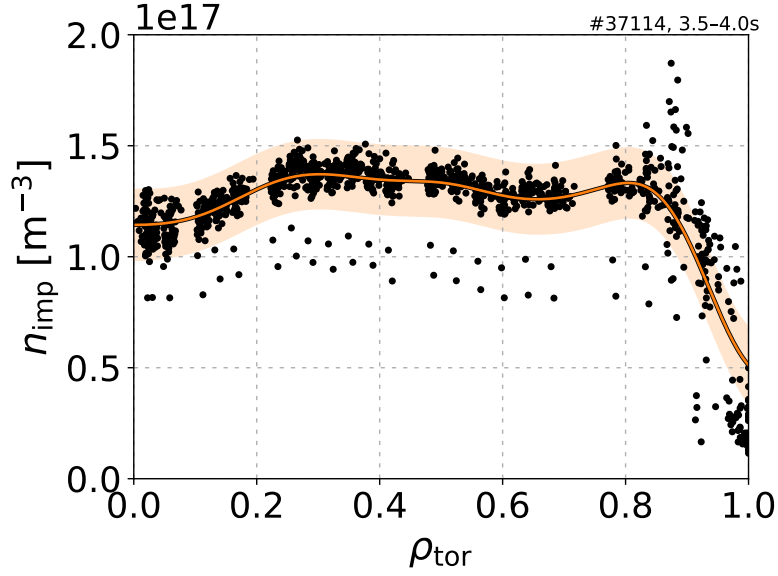Figure 4.1: n_{imp} profile of the discharge #37114. Black dots represent the data measured with CXRS in the time-interval from 3.5–4.0 s. In orange, the fit with GPR1D is shown.

provided by IDI (see section 3.2.7); A fitting through the impurity density data, however, has not yet been included in IDI, as that data is not evaluated routinely. To obtain such a fit, instead the python package GPR1D [104] is used, which – like IDI – is based on gaussian process regression. In figure 4.1 an example for such a fit through raw n_{imp} data is shown. Note that at the pedestal, some channels of the raw data seem to be clear outliers, and as a result also the fit in that region is not very reliable. But since this work focuses on the plasma core, where the fit matches the raw data rather well, this is not an issue.

The most challenging parameter to obtain, that is required to properly calculate E_{r}, is v_{pol}. In the following, the procedure to achieve this is explained in some detail [111, 112]:

As a basis for this experimental method of determining v_{pol}, one can rewrite the total particle flux in the plasma $\vec{u}$ such that it is split into two components; one pointing parallel to the magnetic field $\vec{B}$ and the other representing a rigid body rotation in toroidal direction

$$\vec{u} = \hat{u}(\psi, \theta)\vec{B} + \hat{\omega}(\psi, \theta)\vec{e}_{\mathrm{tor}}. \tag{4.1}$$

When one now projects this equation onto the toroidal and poloidal direction, one arrives at the following two equations:

$$v_{\mathrm{tor}} = s_b \hat{u}(\psi) B_{\mathrm{tor}} + \hat{\omega}(\psi) R \tag{4.2}$$
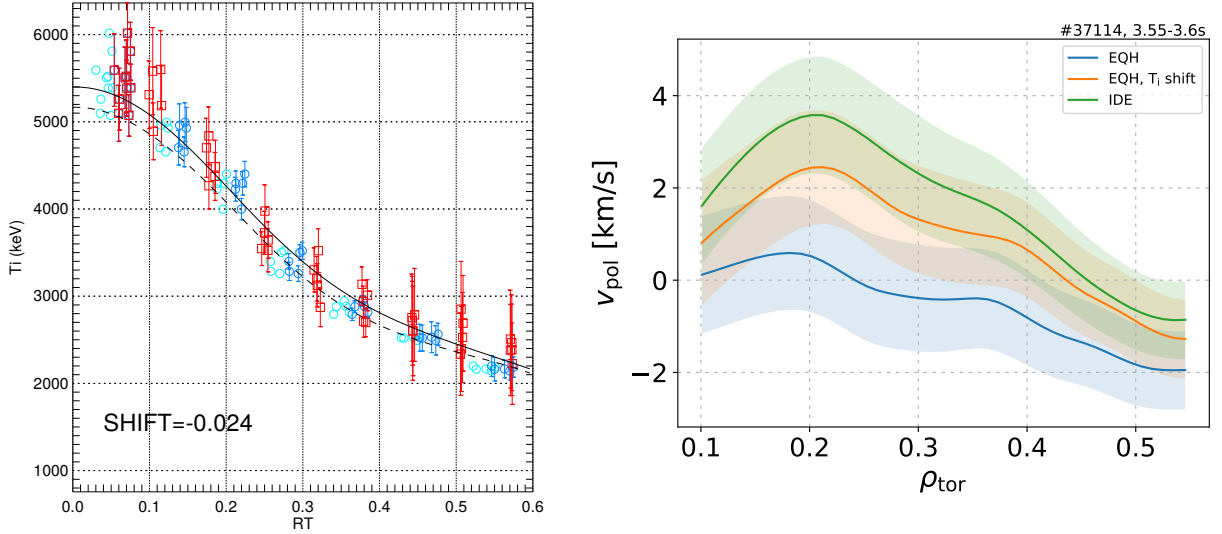$$v_{\mathrm{pol}} = s_j \hat{u}(\psi) B_{\mathrm{pol}} \tag{4.3}$$

Figure 4.2: Left: T_i profiles of discharge AUG #37114. Points in red correspond to data measured on the HFS, points in cyan to ones measured on the LFS. To guide the eye, a solid (dashed) line is fitted through the HFS (LFS) datapoints. Points in blue are the LFS datapoints shifted such that HFS and LFS T_i align. Right: Corresponding v_{pol} profiles using the Cliste equilibrium with (orange) and without (blue) shifting the LFS data such that T_i overlaps. For the line in green, the IDE equilibrium was used instead, with which such a shift was not necessary as HFS and LFS T_i are already in good agreement.

Here, the assumption was made that the plasma density is stationary and constant on a flux-surface, which allows to drop the dependence on θ in equation 4.1 (for details see [111, 112]). In equations 4.2 and 4.3, s_b and s_j indicate the direction (parallel or anti-parallel) with respect to $\vec{B}$ and the plasma current $\vec{j}$.

According to equation 4.2, it is possible to determine the factors $\hat{u}(\psi)$ and $\hat{\omega}(\psi)$ separately, by measuring v_{tor} at two different radial positions on the same flux surface, e.g. on the high- and low-field-side of the plasma. By subsequently plugging $\hat{u}$ back into equation 4.3, one can then obtain v_{pol}.

On AUG, only the CXRS systems using NBI source 8 have lines of sight that span both HFS and LFS. To measure v_{pol}, it is therefore necessary to have this source active – and in particular not have it modulated by, for example, the β feedback control. As a modulation of source 8 could in general not always be avoided in the experiments performed for this work, the measurements of v_{pol} were performed in short (typically 50 ms long) phases throughout which source 8 was set to be constantly active. During these periods, other sources – such as for example the current driving sources 6 and 7 – were modulated. As explained in appendix A, a similar approach has also been used to obtain IMSE measurements; in fact, many of the experiments performed over the course of this thesis were designed such that both IMSE and v_{pol} measurements could be obtained simultaneously.

When determining v_{pol} via this method, it is important that the points on the HFS and LFS that are compared with each other are really on the same flux surface. If HFS and LFS are not aligned properly the results can deviate significantly from the actual values. Such a misalignment can occur if the equilibrium is not reconstructed sufficiently well. On the right-hand side of figure 4.2, example v_{pol} profiles are shown, that result from using either CLISTE (blue) or IDE (green) to map the CXRS data onto flux-surfaces. Between these two profiles, a non-negligible difference can be seen. To determine which equilibrium is better (or if in fact for both such a misalignment occurs), one can compare the ion temperatures on HFS and LFS; as T_{i} is a flux-surface quantity, i.e. it is constant on a given flux surface, the profiles for HFS and LFS should in principle match perfectly. Looking at the T_{i} profiles that use CLISTE for the mapping, a mismatch becomes evident (see figure 4.2, left). For this particular discharge (#AUG 37114), using instead IDE results in a good agreement between HFS and LFS T_{i} profiles, suggesting that the equilibrium reconstructed with IDE is reasonably correct – as one would expect. Though while such misalignments happen less often and to a smaller extent with the more sophisticated IDE code, for some discharges this still occurs.

In these cases, a pragmatic solution for this problem is to simply shift the LFS data for v_{tor} by the same amount that is also required to have HFS and LFS T_{i} data overlap. This method has also been used on the CLISTE-based data shown on the left-hand side of figure 4.2. When evaluating v_{pol} with this shifted dataset, the resulting curve agrees within the uncertainties with the IDE-based profile (figure 4.2, right).

These values for v_{pol}, which are typically of the order of $\sim 5\,\mathrm{km/s}$ in the experiments performed for this work, are significantly lower than the typical values for v_{tor}, which range between 150 and $250\,\mathrm{km/s}$ in the plasma core. If one, however, recalls the formula to calculate the radial electric field $E_r = v_{\mathrm{tor}}B_{\mathrm{pol}} - v_{\mathrm{pol}}B_{\mathrm{tor}} + \frac{1}{eZ_{\mathrm{imp}}n_{\mathrm{imp}}}\frac{dp_{\mathrm{imp}}}{dr}$, the toroidal rotation v_{tor} is multiplied with the poloidal magnetic field B_{pol} while v_{pol} must be multiplied with B_{tor}. As $B_{\mathrm{tor}} \approx 2 - 3\,\mathrm{T}$ is significantly larger than $B_{\mathrm{pol}} \approx 0 - 0.4\,\mathrm{T}$ in the AUG experiments investigated here, v_{pol} can still have a non-negligible effect on the total radial electric field.

On the left-hand side of figure 4.3, it is visualized how much the three individual terms contribute to the total E_{r} in the discharge #37114 (shown in blue). As can be seen, while the largest contribution comes from the toroidal rotation term (orange), the term involving the poloidal rotation (red) still adds up to 20 % to that value. The diamagnetic term (green) partially compensates the additional contribution from the v_{pol}-term, though it is in turn only about 30 % of its size. As a result, the total radial electric field deviates only relatively little from the dominant E_{r} term from the toroidal rotation. Nevertheless, when using these electric fields to calculate $\omega_{E \times B}$, the profile based on all three terms is approximately 30 % larger than the profile calculated based on the v_{tor} term only. It can therefore not be justified to approximate E_{r} with the dominant term from the toroidal rotation; In order to properly determine the $E \times B$-shear, all three terms need to be considered. This is done for the experiments discussed in the following section.
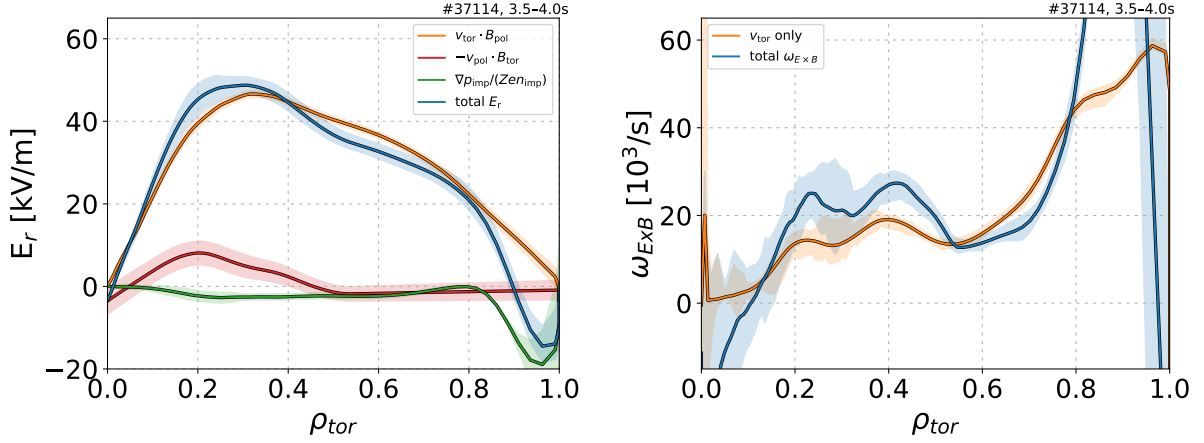
Figure 4.3: Left: Visualization for how much the three different terms in the radial force balance equation (orange, red, green) contribute to the total E_r (blue). Right: The resulting $\omega_{E\times B}$ taking only the dominant v_{tor} into account (orange) compared with the profile considering all terms (blue).

The shaded areas in figure 4.3 indicate estimates on the uncertainties of the profiles. More precisely, they represent the maximum range E_r and $\omega_{E\times B}$ vary when they are calculated with combinations of the minimum and maximum values of the individual parameters that go into equations 2.30 and 2.31.

4.2   Experimental measurements

The experiments discussed in the following are based on the scenario discussed in section 2.6, but with some variations in the settings for the heating and current drive sources. This set of experiments typically involves between 3 and 5 NBI sources – delivering 9–12 MW of heating power and driving approximately 300 kA current in the plasma –, and 4 gyrotrons, whose beams deliver 2.5–3 MW of heating power and approximately 100 kA of plasma current. Like the reference scenario, all experiments performed in the scope of this work have a toroidal magnetic field of 2.5 T on axis and a plasma-current of 800 kA. As already touched upon earlier in this chapter, the experimental strategy for studying the effects of the $E\times B$-shear $\omega_{E\times B}$ involves reducing $\omega_{E\times B}$ by partially replacing approximately 3 MW NBI heating power with ICRF, while keeping β_{pol} constant. This is achieved with feedback control using the NBI input power as actuator. This reduces the number of energetic particles injected into the plasma with a component in toroidal direction, reducing the torque applied to the plasma in the process. This leads to a reduction of v_{tor}, which according to equation 2.30 leads to a reduction of the radial electric field E_r. According to equation 2.31, this in turn finally leads to a decrease in $\omega_{E\times B}$.

In figure 4.4, this is illustrated with time-traces of relevant parameters of such a discharge. Here, ICRF heating is slowly ramped up between 4 and 5 s, and in order to keep β_{pol}

constant, the NBI power is ramped down at the same time. Consequently, the toroidal rotation is reduced as well. Despite the accompanying drop in $\omega_{E\times B}$, T_i remains roughly constant. Note that in this plot, the $E\times B$-shear is calculated taking only the contribution from v_{tor} into account, since it was not possible to obtain time-dependent profiles of v_{pol}.

To look into this in more detail, radial profiles of this discharge are shown in figure 4.5. Here, the lines depicted in blue correspond to the first shaded region in figure 4.4, without ICRF, the lines depicted in orange correspond to the second shaded region with ICRF added. In this figure, the uncertainty bands for $^R/_{LT_i}$ and p_{fast} indicate the range over which the profiles fluctuate, for $\omega_{E\times B}$ the errors represent again the maximum variation based on the uncertainties of the individual parameters it is calculated from. For T_i, the CXRS data points are plotted. In figure 4.5, a clear drop in $\omega_{E\times B}$ can be observed over the
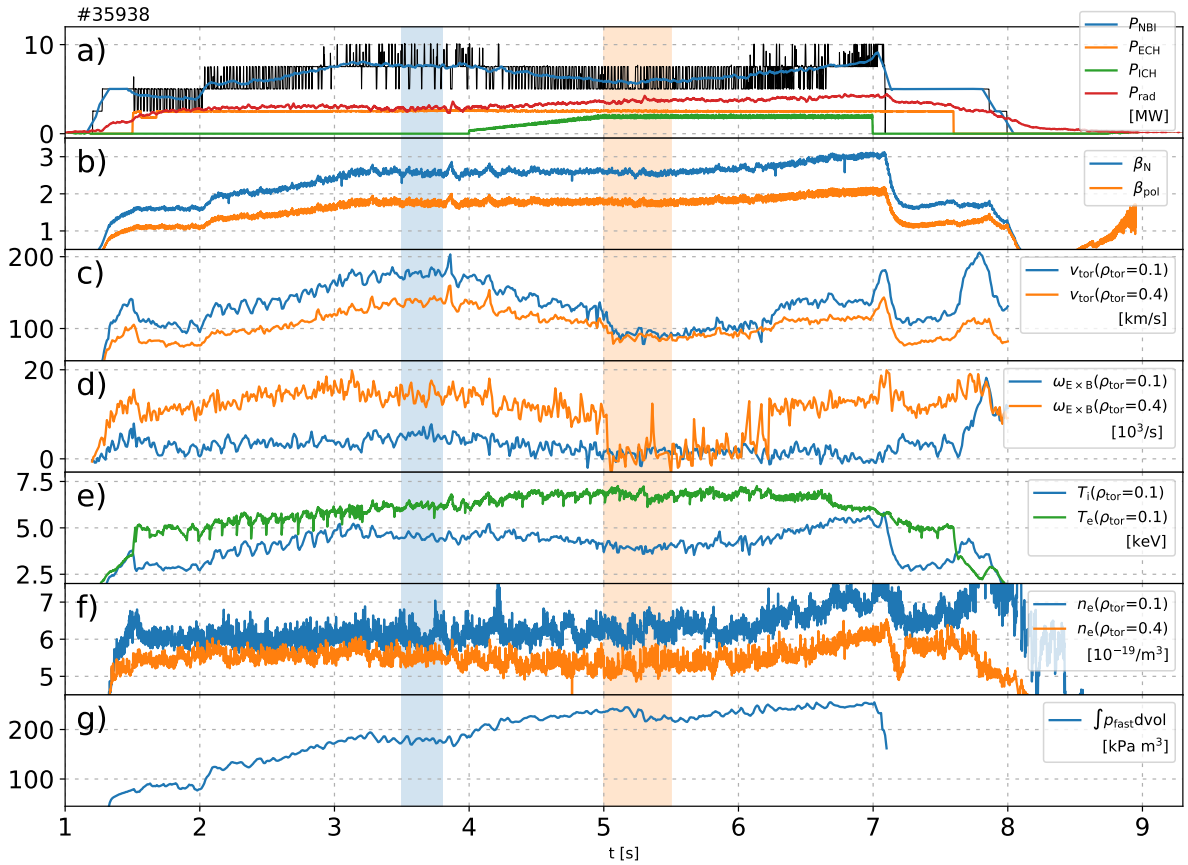
Figure 4.4: Timetrace of key parameters of the AUG discharge #35938, including the power deposited by the different heating systems (a), the plasma beta (b), the toroidal rotation (c), the $E\times B$-shear considering only the contribution from v_{tor} (d), the electron and ion temperature (e), electron density (f) and the integrated fast ion pressure (g). Two stationary phases with and without the addition of ICRF heating are highlighted in orange and blue, respectively.
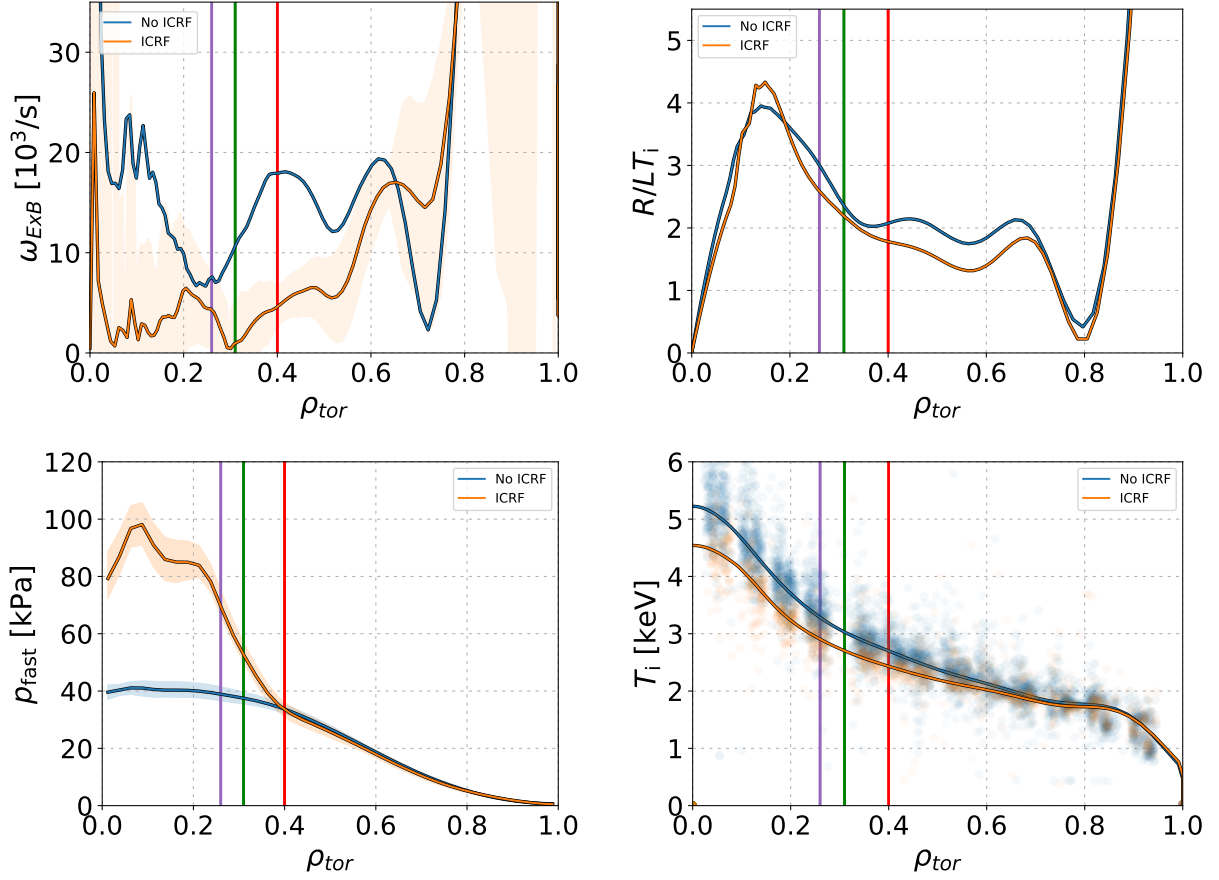
Figure 4.5: Profiles of AUG discharge #35938, comparing two phases with and without ICRF. Profiles are averaged over the two time-intervals highlighted in figure 4.4. Vertical lines mark radial positions at which GENE simulations have been performed.

majority of the radial range. While the biggest change in $E \times B$-shear is around $\rho_{\text{tor}} = 0.4$, also the drop around $\rho_{\text{tor}} = 0.15$ – where the temperature peaking is the strongest – is significant.

At the same time, the logarithmic ion temperature gradient R/LT_{i} stays constant within the uncertainty, suggesting that the $E \times B$-shear does not play a role in the local reduction of turbulent transport. There are, however, two possible complications with the experimental strategy used, as was already briefly touched upon earlier: For one, by adding ICRF heating, the fast ion pressure is strongly increased, as can be seen in figures 4.4 and 4.5. This is owed to the fact that ICRF strongly heats the hydrogen minority species, and further accelerates the energetic particles introduced with NBI heating. Furthermore, by changing the heating mix, the balance between the amount of heating going into the electrons and ions is shifted, affecting the temperature ratio $T_{\text{e}}/T_{\text{i}}$. As described in sections 2.3 and 2.4, both these things potentially affect the ion temperature gradients and turbulent transport in general.

To disentangle potential effects caused by the $E \times B$-shear and ones caused by other parameters, a number of similar experiments has been conducted, to cover a larger area in parameter space. It should also be noted at this point, that the discharge #35938 uses different settings for the ECCD compared to the discharge #32305 introduced in section 2.6, with the ECRH beams pointing less strongly off-axis. This was done mainly to prevent the accumulation of tungsten in the plasma core [113]. To make sure this difference does not influence the results regarding the $E \times B$-shear, similar experiments have also been performed with ECCD settings matching those of the reference discharge #32305. An overview of these experiments is given in figure 4.6. For a complete list of shotnumbers and time-intervals, see appendix B.

In this plot, each point corresponds to an average over a distinct flat-top phase, similar to what was shown for #35938 in figure 4.4, comparing the logarithmic ion temperature gradient $^R/_{LT_i}$ with $\omega_{E \times B}$. Here, both values are taken at the radial position where $^R/_{LT_i}$ has a local maximum. It can be seen that there is no clear correlation between these two parameters. Also when comparing only points belonging to the same discharge – which is indicated by also having the same colour – no trends are visible; in some cases, the ion temperature gradient decreases with increasing $E \times B$-shear, in others it increases or stays constant. The points corresponding to the discharge #35938 are depicted in light blue.
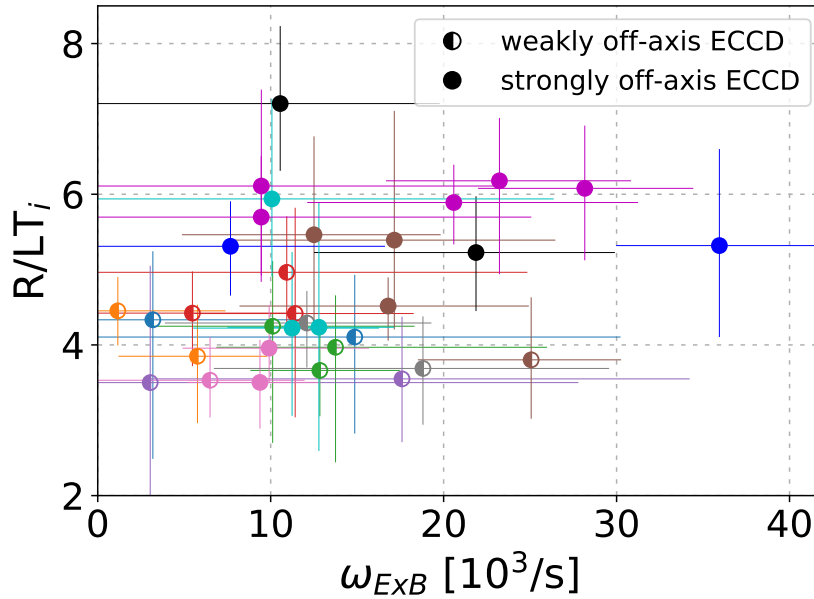

Figure 4.6: Correlation between $^R/_{LT_i}$ and $\omega_{E \times B}$ in a database of discharges where the $E \times B$-shear has been varied. Each point represents an average over a quasistationary phase of several confinement times length, taken at the position where $^R/_{LT_i}$ has its local maximum. Points with the same colour represent different phases within the same discharge. Full or half symbols represent two different settings for the ECCD.
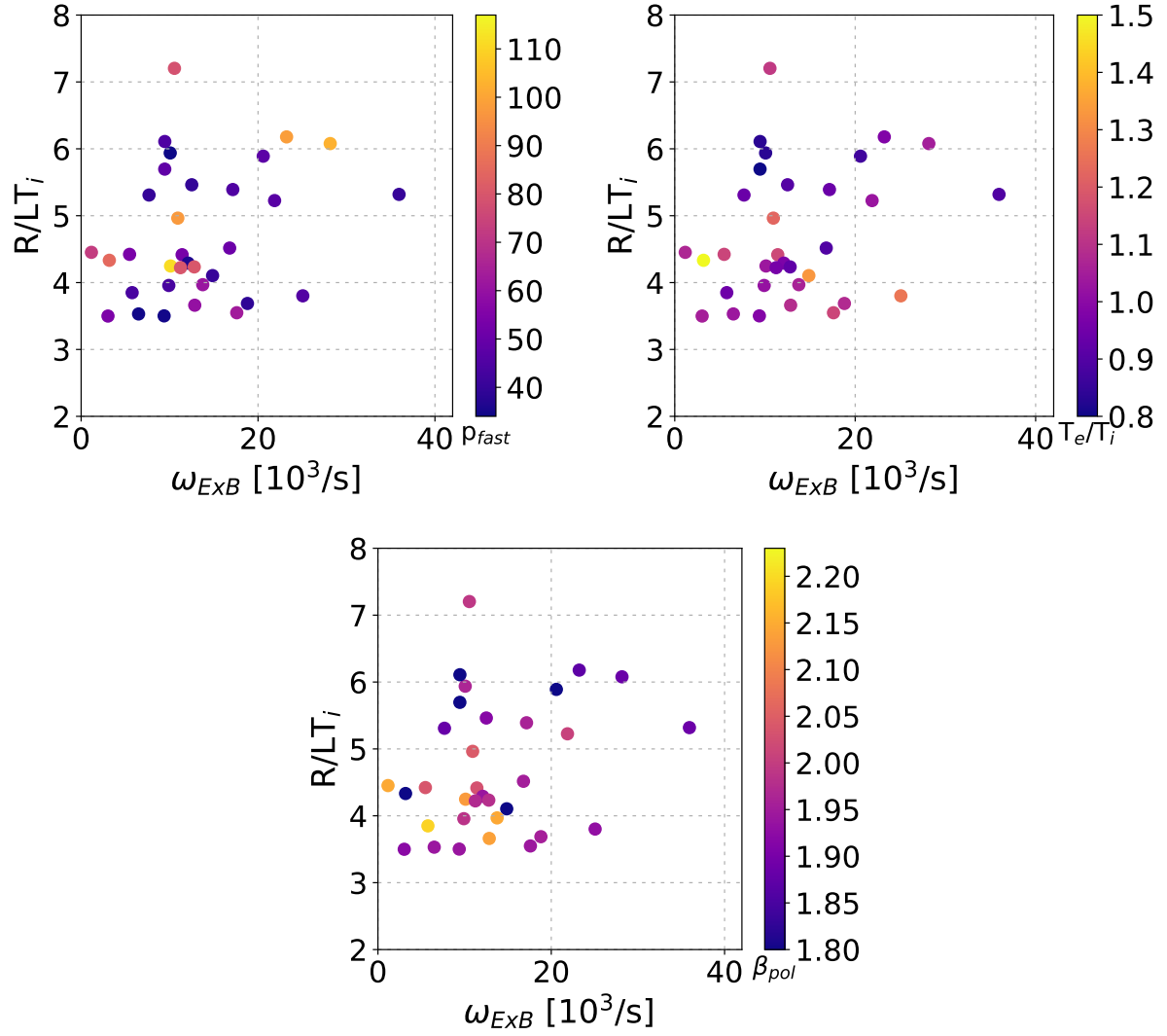
Figure 4.7: Same correlation as in figure 4.6, but with colours representing the fast ion pressure p_{fast} (top left), the temperature ratio T_e/T_i (top right) and the poloidal plasma beta β_{pol} (bottom).

To investigate trends in other parameters, whose effects might compensate effects by the $E \times B$-shear, the same dataset is plotted again, in figure 4.7, but now the colours correspond to secondary parameters of interest – p_{fast}, $T_{\text{e}}/T_{\text{i}}$ and β_{pol}. In order for one of these parameters to compensate potential effects by the $E \times B$-shear, the points in the figure should be well ordered in that parameter, such that its values gradually change with increasing ω_{ExB}. As can be seen in figure 4.7, this is not the case, allowing to reasonably rule out the $E \times B$-shear playing a role in the observed local reduction of transport. It should be noted here that figure 4.7 does not generally indicate that p_{fast}, $T_{\text{e}}/T_{\text{i}}$ and β_{pol} do not also have an effect on R/LT_{i}; it just indicates that in the studies at hand, $\omega_{E \times B}$ could be varied while keeping these parameters relatively constant.

To summarize, various experiments have been performed in which $\omega_{E \times B}$ were varied. In these, no correlation between the $E \times B$-shear and R/LT_i could be observed – even when considering other effects that might compensate $\omega_{E \times B}$-effects – suggesting that the $E \times B$-shear does not contribute significantly to the observed ion temperature peaking. However, it cannot fully be ruled out that a more complicated interplay between three or more parameters might mask an effect from the $E \times B$-shear.

To look into this more closely, nonlinear simulations with the gyrokinetic code GENE have been performed, that allow to vary parameters of interest separately. These simulations will be discussed in section 4.3.

Before that, there is one noticeable correlation in figure 4.7 that needs to be addressed: Cases with lower R/LT_{i} have in general significantly larger values of β_{pol}. This, however, does not mean that higher values of β_{pol} lead to an increase of transport, but is rather related to the fact that this dataset includes two different scenarios with different ECCD settings that have different MHD stability limits. These two different scenarios are indicated in figure 4.6 with different symbols; The one dubbed *"weakly off-axis ECCD"* scenario has a beta limit of $\beta_{\text{pol}} \leq 2.1$, while the scenario dubbed *"strongly off-axis ECCD"* has a limit of $\beta_{\text{pol}} \leq 1.95$. Looking at the distribution of the weakly and strongly off-axis scenarios in figure 4.6, a clear separation between the two scenarios can be observed. With few exceptions, the strongly off-axis scenarios have a strictly higher R/LT_{i} than the weakly off-axis scenarios. The causal relation between β_{pol} and R/LT_{i} in figure 4.7 is therefore not that a lower β_{pol} would imply a higher R/LT_{i}, but rather that for points with a lower R/LT_{i} higher values of β_{pol} are possible. The actual parameter dependence seems to be related to the ECCD settings, and therefore the q-profile.

This subset of experiments, looking in more detail if and how the q-profile affects the local reduction of transport will be explored in chapter 5.

4.3 Using GENE to disentangle $\omega_{E \times B}$ and p_{fast} effects

At the end of the previous section, an attempt was made to disentangle potentially competing effects via statistical means, with the conclusion that the $E \times B$-shear does not seem to

contribute to the peaked ion temperature profiles observed in the scenarios studied in this work. To further support this, nonlinear GENE simulations have been performed on the discharge #35938 to specifically disentangle the effects from $\omega_{E\times B}$ and p_{fast} [114]. Recalling figure 4.5, both these parameters underwent significant changes in this discharge from the phase without to the one with ICRF heating. As the potential effects from a reduction in $E\times B$-shear are opposite to those coming from an increase in fast ion pressure, it is at least conceivable that these competing effects happen to cancel each other out. By varying the potentially competing parameters separately, their effects can be studied independently.

When performing these simulations, several challenges appear: The first of which is finding an adequate radial position to perform them at. Initial attempts were done at $\rho_{\text{tor}} = 0.4$, where the change in $\omega_{E\times B}$ is largest (marked in red in figure 4.5). At that position, however, $R/L_{T_{\text{i}}}$ is already too low, and ETG and TEM modes are dominant over the ITG. Following that, a position further towards the core, at $\rho_{\text{tor}} = 0.26$ was selected (marked in purple), where the ITG is dominant, and there is still a significant change in $\omega_{E\times B}$. At that position, however, the simulations run into numerical complications, due to the fact that s is very close to 0; A low shear causes issues as the box-size of the simulations is normalized with s. Therefore, finally, as a compromise, the position $\rho_{\text{tor}} = 0.31$ was chosen (marked in green). This position is still close enough in the core for ITG turbulence to
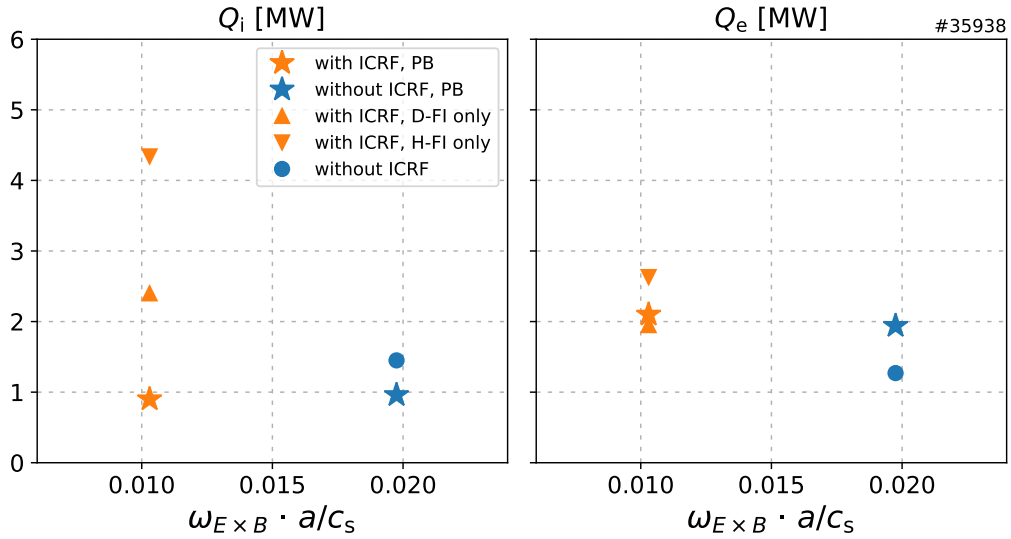

Figure 4.8: Relation between heat fluxes and $E\times B$-shear of AUG discharge #35938, according to non-linear GENE simulations. Stars indicate the power-balance values, obtained from ASTRA simulations, the circle and triangles indicate simulations using the parameters of time-intervals without and with additional ICRF, respectively. For the cases with ICRF, only one of the two fast ion species was used, neglecting either the deuterium or hydrogen species. In all cases, a simple maxwellian distribution was applied. Here, $\omega_{E\times B}$ is normalized to the ratio of the ion sound speed c_{s} and the minor radius a.

dominate, while at the same time having a higher magnetic shear. As can be seen in figure 4.5, this position is at the edge of the region where the gradient is steepened.

The second challenge lies in the fact that for the case with ICRF four species are relevant and need to be considered in the simulations: electrons, the main ions and two species of energetic particles (D and H). This makes them computationally very expensive. First attempts have therefore been conducted using only three species – omitting either the hydrogen or deuterium fast ions. The results of these simulations are indicated with orange triangles in figure 4.8. As can be seen, unlike the simulation of the case without ICRF that has only one fast ion species to begin with, these simulations are not able to reproduce the experimental ion heat fluxes determined with a power balance analysis. This suggests that the full inclusion of the fast ions is necessary. Additionally, a realistic description of the fast ion distribution seems to be important. In initial simulations including both fast ion species with a normal maxwellian distribution function

$$F_{0,M} = \frac{n_0}{\pi^{3/2} v_{\mathrm{th}}^3} \exp\left(\frac{-m v_\parallel^2/2 - \mu B_0}{T_0}\right), \tag{4.4}$$

a good agreement with the experimental values could not be reached. The reason for this seems to be that in this case the fast ion drive becomes too strong, such that the fast ion driven modes start to become dominant over the ITG mode. Only when both fast ion
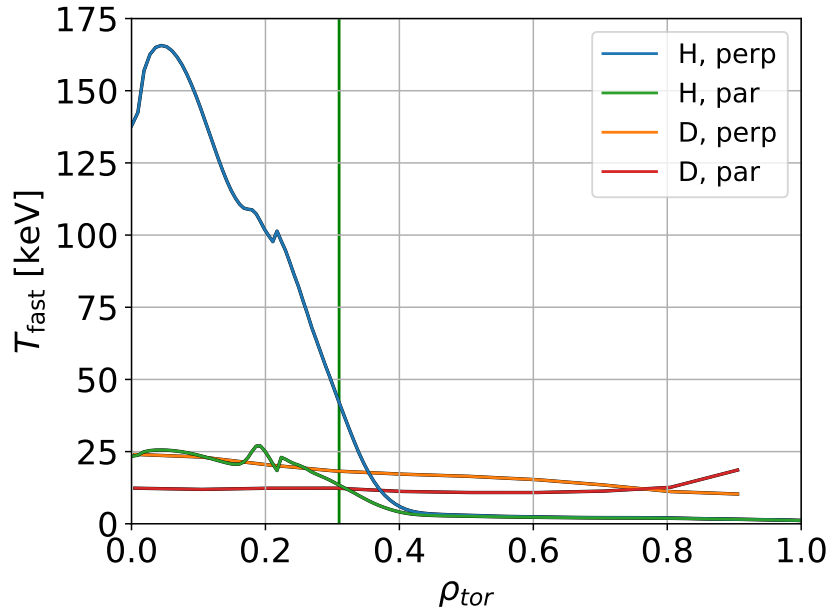

Figure 4.9: Parallel and perpendicular components of the temperatures of the hydrogen (blue, green) and deuterium (orange, red) fast ion populations.

species are described by a bi-maxwellian distribution function [115]

$$F_{0,BM} = \frac{n_0}{\pi^{3/2} v_{\text{th},\parallel} v_{\text{th},\perp}^2} \exp\left(-\frac{v_\parallel^2}{v_{\text{th},\parallel}^2} - \frac{\mu B_0}{T_\perp} \right), \tag{4.5}$$

considering the parallel and perpendicular components of the fast ion temperatures $T_{\text{fast},\parallel}$ and $T_{\text{fast},\perp}$ separately, a reasonable match with the power balance could be achieved. This is because the parallel and perpendicular components contribute differently to the drive of the mode. By correctly describing the anisotropies in the temperatures, the fast ion driven modes and the associated stabilization of the ITG does not grow too strong. In equations 4.4 and 4.5, μ and $v_\parallel$ are the magnetic moment and the velocity parallel to the magnetic field line, respectively. Together with the spacial coordinate $\vec{X}$, they form the gyro-center coordinate system that GENE uses. This important point of being able to include more realistic distribution functions has been made possible only recently, through an extension in the GENE code [115].

The separate components for the fast hydrogen temperature were calculated with TORIC, coupled with SSFPQL to correctly treat the interaction between ICRF and NBI (see figure 4.9, blue, green). $T_{\text{fast},\parallel}$ and $T_{\text{fast},\perp}$ for the deuterium fast ions were calculated with TRANSP, coupling both NUBEAM for the acceleration due to NBI and TORIC for the acceleration due to ICRF (figure 4.9, orange, red). The exact input values that have been used for this – and all other GENE simulations shown in this work – can be found in appendix C.

The final challenge is related to the radial position that was chosen in the end; For the case with ICRF, electron scale turbulence already starts to play a significant role at that point. To describe the ETG turbulence properly, a higher wave-number resolution would be necessary. Unfortunately, the resources necessary for such multiscale simulations exceed what was available for this study. Because of that, the electron heat flux Q_e is significantly overestimated in that case, as can be seen in figure 4.10. For studying relative effects from variations in individual input parameter, a good match for Q_i should be sufficient, however. As is shown in this figure, a reasonable match of Q_i with the power balance values could indeed be achieved. Here, the points in blue indicate simulations using the parameters from a time-interval without ICRF that nominally has a higher $E\times B$-shear, points in orange indicate simulations using parameters from the interval with ICRF that has a lower $E\times B$-shear.

After overcoming these challenges, one can now investigate the effects of varying $\omega_{E\times B}$, while keeping other parameters such as p_{fast} or T_e/T_i fixed. This is done by repeating the two GENE runs matching the ion power-balance values for both cases, but with the values for $\omega_{E\times B}$ of the respective other case. If indeed the $E\times B$-shear had an effect that is masked by other competing effects, then these simulations should result in a significant deviation from the power balance and the simulation done with the nominal $\omega_{E\times B}$. But as can be
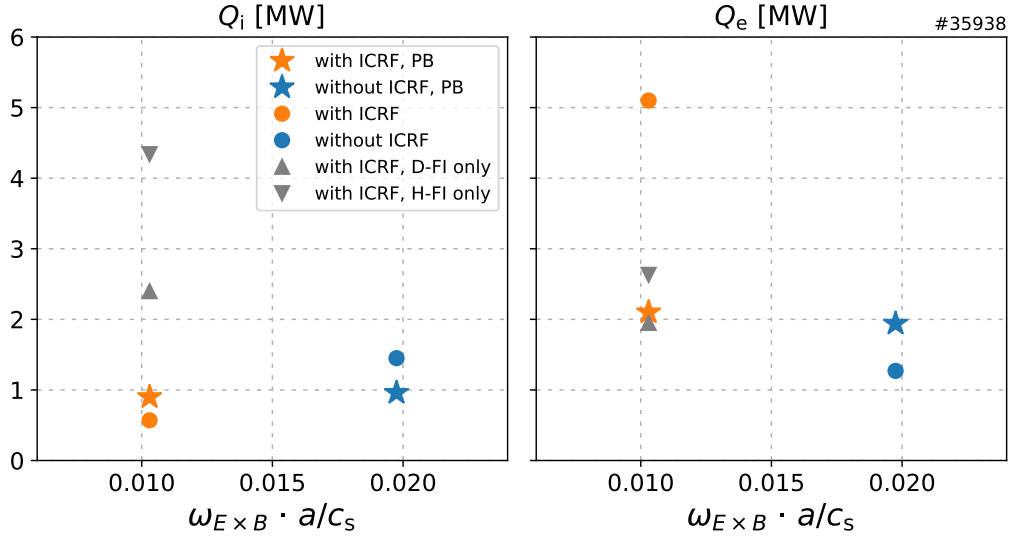
Figure 4.10: Resulting heat fluxes for non-linear GENE simulations of AUG discharge #35938. As in figure 4.8, stars indicate the power-balance values obtained from ASTRA simulations, the circle in blue indicates a simulation using the parameters of the time-interval without additional ICRF. For the case with ICRF, all four kinetic species (i.e. electrons, ions, and D and H fast ions) are now included, the fast ion species additionally with a bimaxwellian distribution. This is marked by the orange circle. For comparison, the simulations using only one fast ion species are indicated in grey.
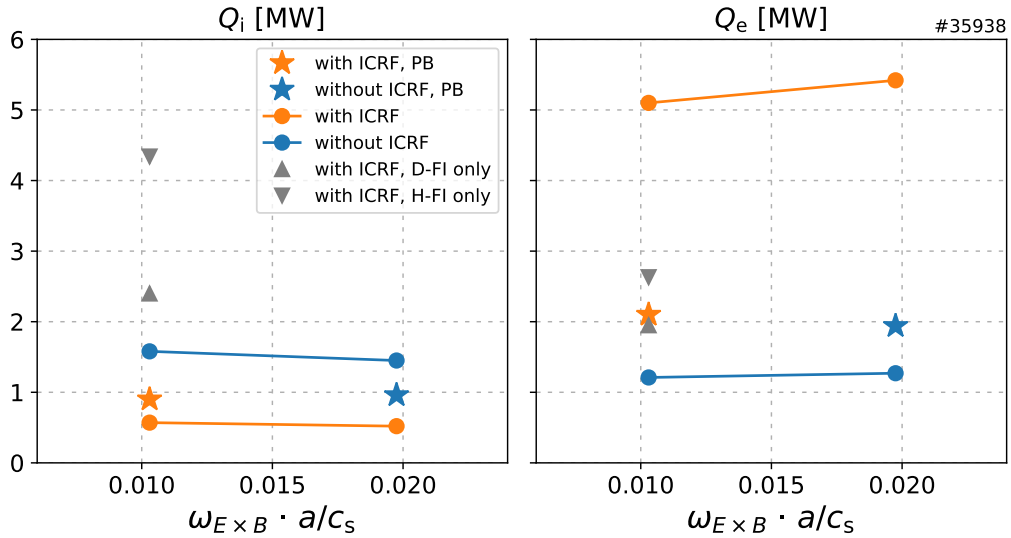
Figure 4.11: Same comparison of heat fluxes obtained with GENE compared to the power-balance values obtained with ASTRA as was shown in 4.10. Additional markers represent simulations that repeat the cases without and with ICRF, while varying $\omega_{E\times B}$. For the case with ICRF, again four kinetic species with realistic distribution functions were included.

seen in figure 4.11, the heat fluxes do not change when changing $E\times B$-shear.

This further supports the results of the experiments described in the previous section and suggests that the $E\times B$-shear does indeed not contribute to the reduction of turbulent transport in the scenarios under investigation here.

5 Effect of ECCD-Profile on R/LTi

In section 4.2, it was observed that there is a clear separation in the achieved R/LT_i, depending on what settings for the electron cyclotron current drive were used (see figure 4.6). With few exceptions, the discharges where the current was driven strongly off-axis in co-current direction (i.e. the same direction as the induced I_p), have a strictly higher R/LT_i than the discharges with a more weakly off-axis co-current drive. The exceptions to this rule – where discharges with a strongly off-axis ECCD scenario have a low R/LT_i – all started with the weakly off-axis current drive, before setting the ECCD further off-axis. This ECCD dependence should come as no surprise, as the different potential effects of the q-profile (which is of course strongly connected with the current drive profile) were already discussed in sections 2.3.2 and 2.4.

In this chapter, in section 5.1, experiments will be discussed, in which the ECCD position was varied during the discharge, to more directly observe effects on R/LT_i. As shifting the ECCD further off-axis also means that the ECRH system deposits less heat in the plasma core, in this region the electrons get heated less while the ion heating remains the same. Since the resulting changes in $T_\mathrm{e}/T_\mathrm{i}$ can also affect the ion temperature gradients, again non-linear GENE simulations are performed to disentangle these potentially competing effects. These simulations are discussed in section 5.2. As it will turn out that even relatively small changes (compared to measurement uncertainties) to the q-profile have a significant effect on R/LT_i, further experiments are attempted that aim to achieve a more precise determination of q by making use of IMSE measurements. This would allow to investigate in more detail what mechanisms exactly are behind q leading to a reduction of transport – whether it is the presence of a strong negative magnetic shear s, or if it is rather the value of q itself, as numerical studies in references [68, 69] suggest. These experiments are discussed in section 5.3. In section 5.4, finally, an attempt is made to incorporate effects from q and s in TGLF simulations, such that the experimental ion temperature profiles can be reproduced. In doing so, further insights about how the q-profile relates to the reduction of transport can be gained.

5.1   Initial experiments varying the ECCD location

As in the previous chapter, the experiments discussed in the following are based on the scenario discussed in section 2.6, but with some variations in the settings for the current drive sources. The general experimental strategy is to run an experiment similar to the ones discussed in the previous chapter, but then switch the ECCD settings at some point during the discharge. In doing so, an effect should be directly observable in a change in T_i. An overview of such an experiment can be seen in figure 5.1.

In the first part of this discharge (AUG #37114), the electron cyclotron current drive was in the "weakly off-axis" setting, centered around $\rho_{tor} = 0.1$–0.2. Then, after $4\,\text{s}$, the ECCD is broadened and shifted further outward, to now lie between $\rho_{tor} = 0.2$–0.5 (see figure 5.2). Since q on a given flux-surface is inversely proportional to the current enclosed by said flux-surface, shifting the current drive in this way should lead to an increase in q within $\rho_{tor} = 0.15$.
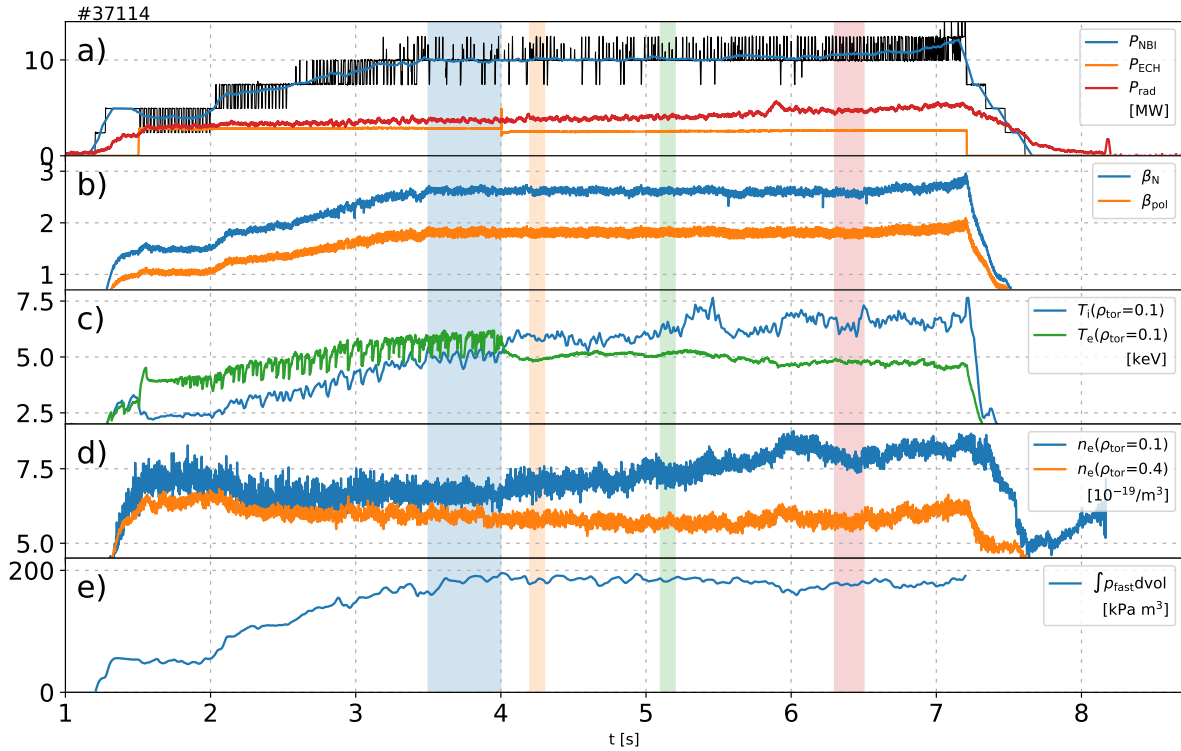

Figure 5.1: Timetraces of key parameters of the AUG discharge #37114, including the power deposited by the different heating systems (a), the plasma beta (b), the electron and ion temperature (c), the electron density (d) and the integrated fast ion pressure (e). A stationary phase in the "weakly off-axis" scenario is highlighted in blue, as well as three time intervals in the "strongly off-axis" scenario are highlighted in orange, green and red. The switch from "weakly off-axis" to "strongly off-axis" is done at $4.0\,\text{s}$.
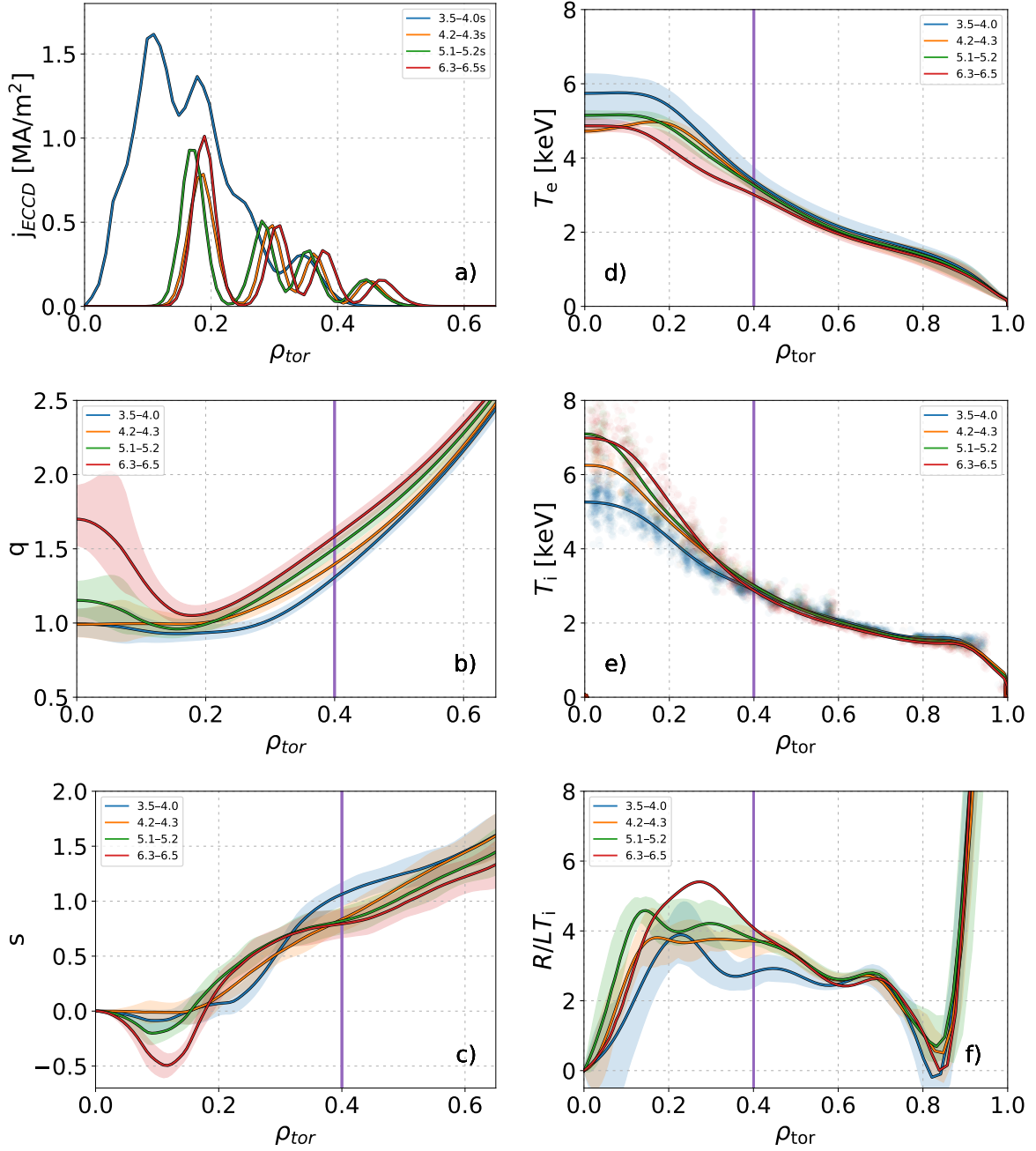
Figure 5.2: Profiles of AUG discharge #37114, comparing a phase with weakly off-axis ECCD settings (blue) with three phases of more strongly off-axis ECCD settings (orange, green, red). Profiles are averaged over the time-intervals highlighted in figure 5.1. Depicted is a) the current density driven by ECCD and profiles of the resulting q (b), s (c), T_e (d), T_i (e), and R/L_{T_i} (f). The vertical line indicates the position at which the GENE simulations have been performed. The Uncertainty bands in the right column indicate the range over which profiles fluctuate, for q and s they are averages over the errors calculated by IDE.
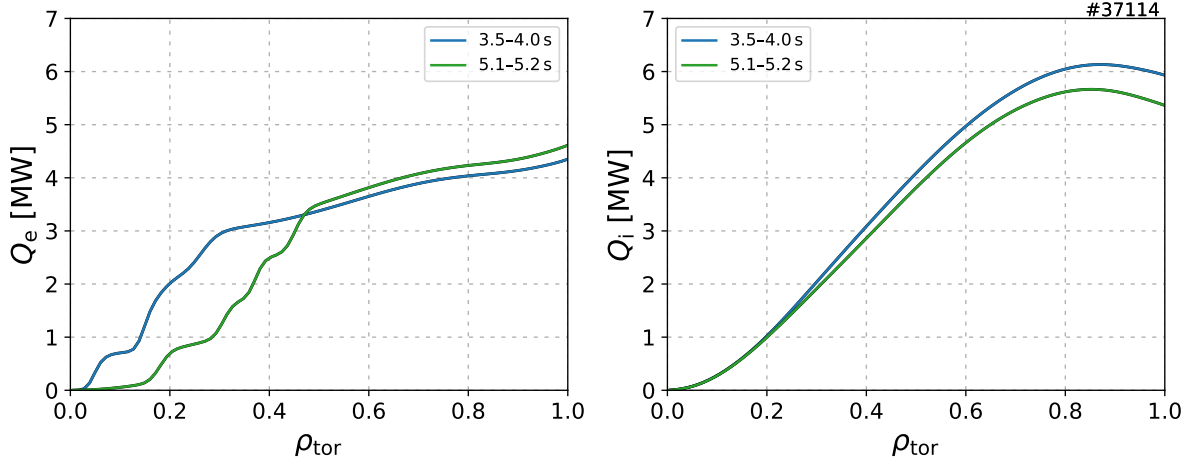
Figure 5.3: Electron (left) and ion heat flux (right) of the AUG discharge #37114. Compared are two time-intervals, one with a weakly off-axis ECCD (blue) and one with a more strongly off-axis ECCD (green). Colours are the same as in figure 5.2. As can be seen, shifting the ECCD further off-axis also leads to the ECRH depositing less heat in the core.

Looking at the time-traces in figure 5.1, the ion temperature is significantly increased after the shift in ECCD is done. This is even more clearly visible in figure 5.2, where one can see that the strongly off-axis driven time-points have a much more peaked T_i. In this figure, the colours correspond to the shaded regions in figure 5.1. This increase in T_i clearly implies that the q-profile has a significant effect on the reduction of transport. However, as in the experiments investigating the effect of the $E \times B$-shear, in reality it is never possible to just change one parameter while keeping everything else constant.

While in this case the fast ion pressure does not change between the different phases, by shifting the ECCD further off-axis also less heat is deposited into the electrons in the plasma core. This can be seen in figure 5.3. As a result, in this region the electrons get heated less, while the ion heating remains the same. As therefore T_e/T_i is reduced (from T_e/T_i=1.16 (blue in figure 5.2) to 1.08 (yellow, green) to 1.05 (red) at ρ_{tor}=0.4 and from T_e/T_i=1.14 (blue) to 0.83 (yellow) to 0.81 (green) to 0.73 (red) at ρ_{tor}=0.1.), the steeper ion temperatures might simply result from an increase of the critical gradient of the ITG. Furthermore, as can be seen in figure 5.1, the electron density slowly increases throughout the discharge. Since R/L_{n_e} also factors into the critical gradient, this can also contribute to an increase of the ion temperature peaking.

To rule out the possibility that the change in T_i is not caused by a change of the q-profile, but rather owed to the change in heating mix, again nonlinear GENE simulations have been performed [114]. These simulations are discussed in section 5.2.

5.2 Disentangling q-profile and T_e/T_i effects with GENE

The general strategy for these GENE simulations is similar to the ones performed to investigate the effect of the $E \times B$-shear: At first, simulations were run using the experimentally measured parameters as input, to make sure the simulations match the power-balance performed with the transport code ASTRA. After that, the simulations are run again, but this time with the inputs for q and s swapped between the two time-intervals; i.e. the simulation that otherwise uses the inputs for the "weakly off-axis" case uses the values for q and s from the "strongly off-axis" case, and vice versa. This way, it is possible to gauge how big the effect of the q-profile is, independent of other potentially conflicting effects. If q and s are driving factors behind the reduction of transport, then the fluxes should reduce in the weakly off-axis case and increase in the strongly off-axis case; If the steepening of T_i is mainly caused by other effects such as T_e/T_i or a steeper electron density gradient, then the fluxes should remain unchanged.

The time-intervals for which these simulations have been run were 3.5–4.0 s for the weakly off-axis current drive case (blue lines in figure 5.2) and 5.0–5.5 s for the strongly off-axis case (green lines in figure 5.2); The radial position for which these simulations have been run is $\rho_{tor} = 0.4$, the position where the profiles start to deviate from each other.

As can be seen in table 5.1, when swapping q and s, the fluxes actually increase in both cases. In the case with the weakly off-axis ECCD scenario, this, however, is due to the fact that with these inputs, a stability threshold is crossed such that the plasma is in a regime where it is dominated by MHD modes. To investigate at least the general trend for the dependence of Q_i on q and s, linear GENE simulations have been performed to test how much the q of the weakly off-axis case can be increased and how much its shear can be decreased to come as close as possible to the strongly off-axis case without crossing

settings	weakly off-axis ECCD				strongly off-axis ECCD		
	PB q=1.45, s=0.91	GENE q=1.45, s=0.91	GENE q=1.56, s=0.81	GENE q=1.45, s=0.85	PB q=1.56, s=0.81	GENE q=1.56, s=0.81	GENE q=1.45, s=0.91
Q_i [MW]	2.8	3.0±0.2	(21)	2.6±0.1	2.8	3.4±0.2	16±1
Q_e [MW]	3.2	3.1±0.2	(230)	5.0±0.2	2.3	2.3±0.1	11±1

Table 5.1: Heat fluxes resulting from non-linear GENE simulations of AUG discharge #37114, compared to ASTRA power balance (PB) results. In these simulations, two different time-points are studied – one with a weakly off-axis, one with a strongly off-axis ECCD – to investigate if the differences between those points can be explained by the change in q-profile. To this end, the values for q and s are swapped between those two points. Note that the "weakly off-axis ECCD" case with q and s from the "strongly off-axis ECCD" is in the simulations no longer dominated by ITG driven instabilities. The results of these simulations are displayed in brackets, as they cannot be compared with the others.

this MHD threshold. The linear simulations reveal that the weakly off-axis case lies in fact already almost right below this threshold. The biggest change possible is to decrease s from 0.91 to 0.85, while leaving q constant. Within this small change, Q_i is slightly reduced, which is consistent with what one would expect if the q-profile is indeed the driving factor behind the change in T_i. At this point, one might wonder why the actual experiment did not hit this MHD limit and become unstable as it was switched from the weakly to the strongly ECCD settings; this is because – as can be seen in figure 5.2 – the q-profile evolves relatively slow, over the course of multiple seconds. Along with this slow change in q-profile also the other plasma parameters can gradually evolve, which evidently also leads to a gradual increase in the MHD threshold.

The second time interval – with the strongly off-axis ECCD case – remains in an ITG dominated regime when the q and s swap is performed. Here the fact that the fluxes increase strongly, by almost a factor of 5, strongly implies that the slightly changed q-profile is indeed necessary to sustain the reduced transport; the improved T_e/T_i ratio alone is not enough for this.

Additionally, it should be mentioned here that some of the inputs for the GENE simulations matching the power balance required some fine-tuning. Both for the simulations shown listed in table 5.1, but also the ones discussed in section 4.3. In particular both q and s needed to be scanned. While these scans are not detailed enough to give information about the exact dependence of Q_i on q and s, they at least allow to infer general trends and get an idea of how sensitive these simulations are to these parameters. An overview of these scans can be seen in table 5.2.

	#37114 strongly off-axis		#35938 high $\omega_{E \times B}$		#35938 low $\omega_{E \times B}$	
settings	q=1.45, s=1.01	q=1.54, s=0.86	q=1.09, s=0.51	q=1.20, s=0.46	q=0.98, s=0.75	q=0.95, s=0.7
Q_i [MW]	7.7±0.4	6.2±0.3	1.5±0.1	1.3±0.1	0.8±0.1	0.5±0.1
Q_e [MW]	4.8±0.2	3.8±0.2	1.2±0.1	0.9±0.1	7.1±0.4	5.1±0.3

Table 5.2: Heat fluxes resulting from non-linear GENE simulations of AUG discharge #37114 and #35938. Here, pairs of almost identical simulations are compared, between which only q and s were varied. It can be seen that small increases in q and reductions in s of the order of $\sim 10\,\%$ lead to significant reductions in the ion and electron heat fluxes, with the effects of s seemingly dominating over q effects when adjusting both in competing directions. Note that the "strongly off-axis ECCD" simulations in this table have higher fluxes than the simulations using the same q and s depicted in table 5.1; this is because in the simulations depicted there, also R/LT_i needed to be varied for a good match with the power balance. An overview of the inputs used for these and all other GENE simulations performed for this work, can be found in appendix C.

Unfortunately, the resources available for these simulations were not enough to scan q and s separately to determine the individual parameter dependencies. However, in [69], GENE simulations of similar scenarios found Q_i to be affected non-linearly with q and s. As was already briefly described in section 2.4.3, the underlying mechanism in these simulations is a coupling between the ITG and linearly stable fast ion driven modes that leads to a stabilization of the ITG. Changes in the magnetic geometry affect the marginal stability threshold of these fast ion driven modes and therefore also have an impact on the amount of ITG stabilization. In more detail, Q_i has been found in [69] to sharply decrease once a threshold in pressure is exceeded. This threshold decreases quadratically with q, and is also impacted by s. The influence of s can be both stabilizing or destabilizing depending on other parameters, though the trend for scenarios similar to the ones studied in this work is that lower values of s lead to a lower Q_i. Comparing this with the scans in tables 5.1 and 5.2, these trends are in general recovered.

As will be shown in section 5.4, quasilinear simulations using ASTRA/TGLF cannot reproduce this behaviour without modifications to the transport model, that allow the incorporation of additional q and s dependent effects. To be able to do this properly, however, it is important to understand more clearly how the reduction of transport is dependent on the q-profile. One aspect – which is consistent with the simulations discussed in this section – seems to be that it is a fast ion effect that depends on the absolute values of q and s. But as was described in section 2.4.2, also negative values of s have been found to play an important role in reducing turbulent transport. In the simulations previously discussed, this area of parameter space has not been accessed.

To study this question in more detail, additional experiments have been performed, similar to the plasma discharge #37114. These are discussed in the following section 5.3. As could already be seen in #37114, even relatively small changes in q and s can have a significant effect on T_i. Because of that, special care has been taken to constrain the reconstruction of the q-profile as much as possible, to get q-profiles with sufficiently small error-bands.

5.3 Further experiments with IMSE measurements

In section 3.2.7, it was discussed that the output from the CDE solver used as constraint for the IDE evaluation cannot always be relied on, since it can happen that the current distribution doesn't behave according to neoclassical theory. For a conservative representation of the q-profiles, IDE therefore calculates an error estimate that does not take into account calculations of the CDE solver. An example for such profiles can be seen in figure 5.4. Here, q-profiles of the discharge #37114 are shown again, the same as in figure 5.2. While the values for q themselves are identical between the two figures, the uncertainties without CDE are significantly larger. In fact, within the error bars, the profiles in figure 5.4 are indistinguishable. Whats more, as the magnetic shear s is calculated from the gradient of the safety factor, the uncertainties of the shear profiles are naturally amplified to be even larger than the ones of q. In case the CDE is not considered for the uncertainties of
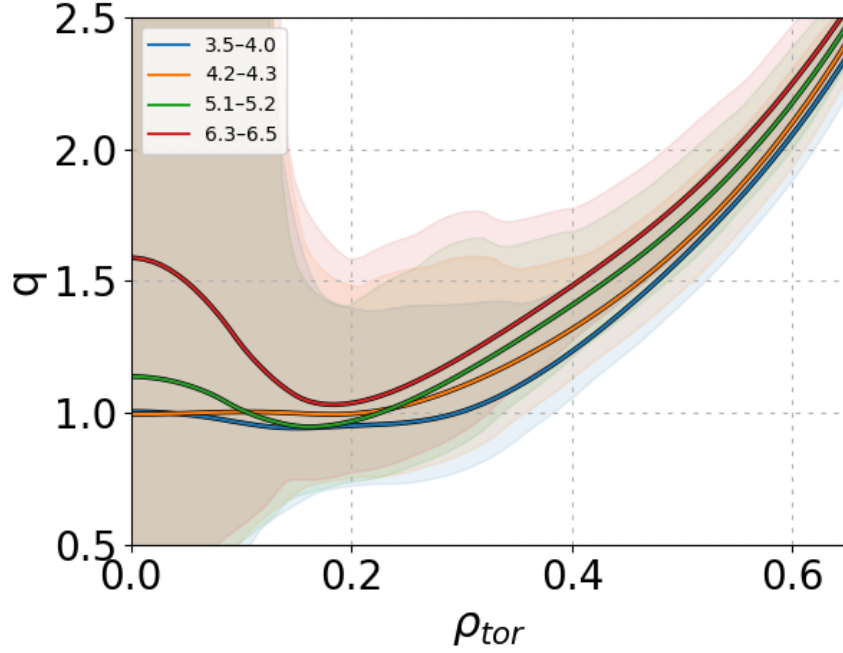
Figure 5.4: *q*-profile of AUG discharge #37114. Uncertainty bands based solely on measured data, disregarding contributions from CDE calculations.

q, IDE does in fact not calculate them for *s* as they would be essentially arbitrarily large.

As was also discussed in section 3.2.7, the uncertainties for *q* (and therefore *s*) can be significantly reduced if IMSE data is available as an additional constraint for the IDE evaluation. As briefly touched upon in section 3.2.6 and elaborated on in appendix A, there are a number of challenges involved in such measurements, regarding conflicting requirements for the NBI sources and difficulties with obtaining a good calibration. Nevertheless, IMSE measurements could be obtained for a number of AUG discharges similar to #37114, allowing to obtain profiles of *q* and *s* with significantly smaller error-bars.

An overview over this ensemble of discharges can be seen in figure 5.5. Here, six profiles obtained with strongly off-axis ECCD are shown in orange, and three profiles obtained with weakly off-axis ECCD settings are shown in blue. In total, these nine profiles are taken from four different discharges which all have sawtoothing phases that allow a calibration of the IMSE. For a detailed list of shotnumbers and time-intervals of the profiles depicted in that figure, see appendix B.

As in the original experiment – AUG #37114 – the discharges with the strongly off-axis current drive feature more strongly peaked ion temperatures compared to the discharges using more central ECCD; This can be seen well in the $R/{LT_i}$ subplot. At the same time, these strongly off-axis ECCD discharges feature *q*-profiles that are slightly elevated at mid-radii, compared to the weakly off-axis discharges, and feature in general a strong reversed
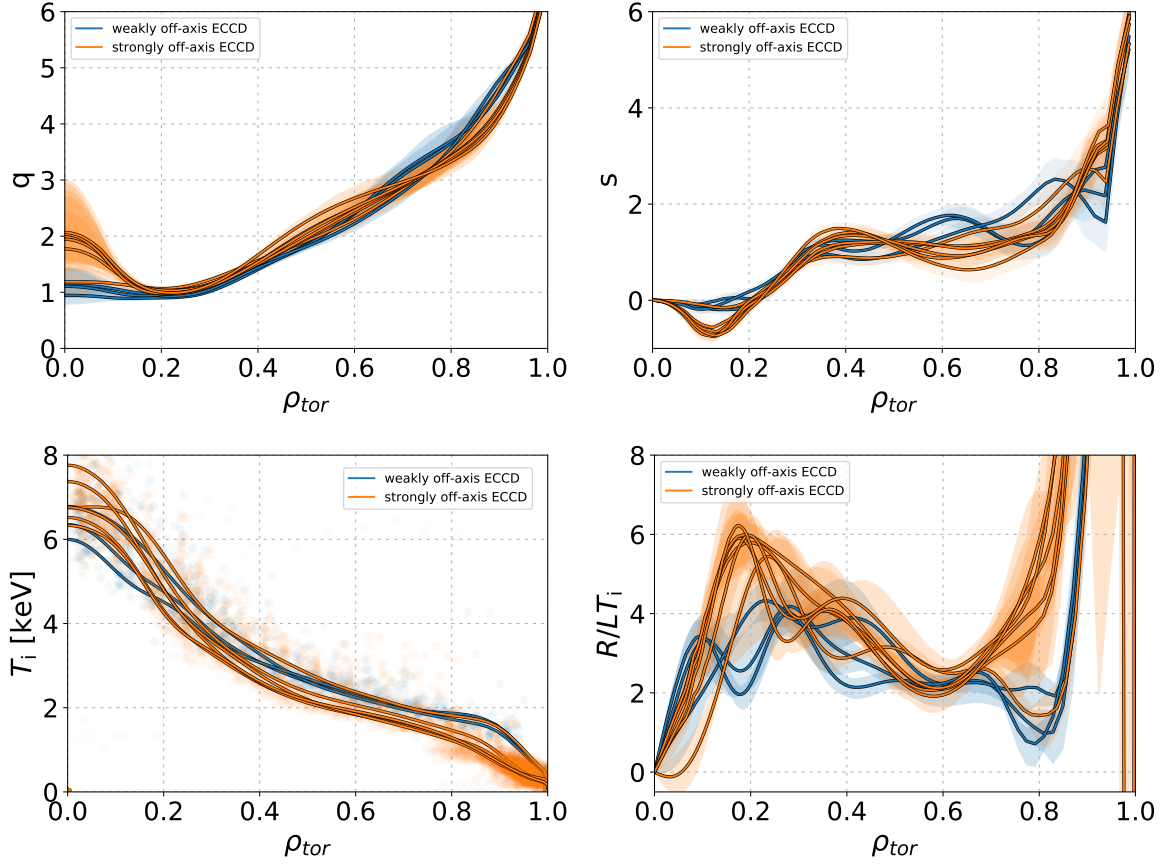
Figure 5.5: Ensemble of profiles comparing the effects from applying weakly and strongly off-axis ECCD in several different AUG discharges. T_i and R/LT_i are fitted with IDI, q and s are reconstructed with IDE, taking IMSE data into account.

shear in the core. It should be noted that, while in fact the position of the strongest ion temperature gradient – around $\rho_{tor} = 0.18$ – is just inside the position where the magnetic shear generally switches sign – around $\rho_{tor} = 0.21$ – the normalized R/LT_i is also increased further off-axis, up to $\rho_{tor} = 0.3 - 0.4$. This indicates that while the presence of a negative magnetic shear appears to also play a role in the observed reduction of transport, the more important factor seems to be the absolute value of q.

To investigate this further, a number of additional experiments has been performed, applying a wider variation of the ECCD settings to extend the range q and s lie in. For these experiments the IMSE measurements were done using NBI source 7. As discussed in appendix A, a calibration of the IMSE based on sawtoothing phases was not possible for these discharges as none were present. Instead, the IMSE offset needed to be determined based on other discharges, assuming that it does not change throughout an experimental campaign (a fact that has been observed for IMSE measurements using source 8). Two suitable discharges were found to calibrate the source 7 IMSE data, which were, however,
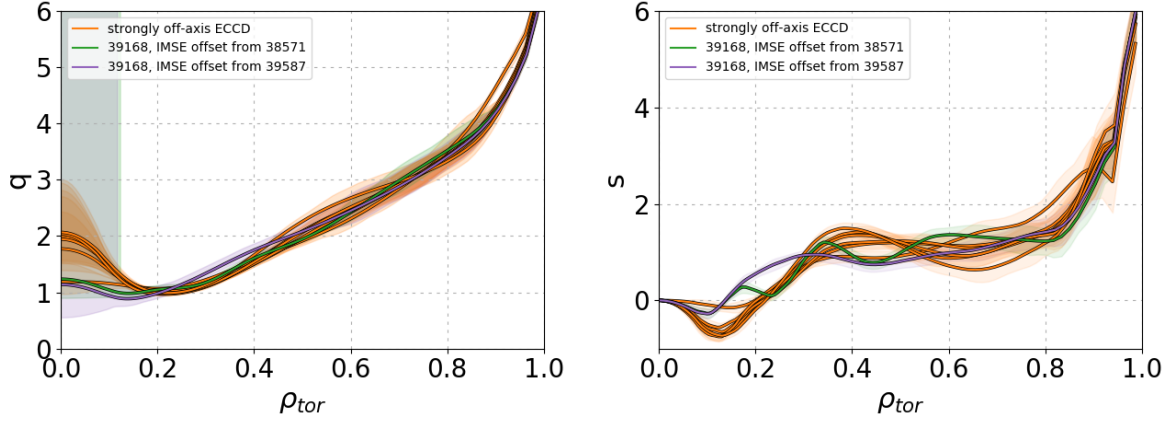
Figure 5.6: q and s of the discharge #39168 reconstructed with IDE, using the IMSE offset determined based on #38571 (green) and on #39587 (purple), compared to other "strongly off-axis ECCD" profiles where calibrated IMSE data is available (orange).

in contradiction with each other. Neither offset could be ruled out based on the nature of the sawteeth or the difference in time to the experiments under investigation.

However, for one of the discharges for which source 7 IMSE data is available – AUG #39168 – the ECCD settings are simply the "strongly off-axis" scenario already discussed at length. As one can reasonably assume that the q-profile for #39168 should be very similar to the other strongly off-axis discharges, if the profiles using one of the source 7 offsets don't match, this offset could reasonably be excluded. In figure 5.6, this comparison is shown.

It can be seen that actually both reconstructions match the other "strongly off-axis" discharges (depicted in orange) reasonably well, though the profiles using the offset based on #39587 (purple) deviate a bit more strongly, in particular for the shear. For the profile using the offset based on #38571 (green) the agreement also with the shear is better. In the following, it is therefore assumed that the profiles using the #38571 offset are more reliable, though for comparison also the profiles based on the other offset are shown.

Besides #39168, three more discharges were performed that use source 7 IMSE data. In figure 5.7 an overview of these experiments is given. While #39168 (shown in pink) uses four ECCD beams aligned off-axis in co-current direction, #39170 (grey) applies its four beams such that the current is driven in counter-direction (opposite the induced I_{p}), and more centrally, within $\rho_{\mathrm{tor}} = 0.1$. This counter-current compensates the induced current flowing in co-direction, pushing q to higher values in that region and causing a strongly reversed shear. AUG #38395 and #39169 (both red) use only two ECCD beams, one very centrally, the other around $\rho_{\mathrm{tor}} = 0.25$, resulting in a profile monotonously decreasing towards the core, without reversed shear. It should be noted here that despite q being slightly below 1 in the core – due to their strong on-axis current drive – #38395 and #39169 do not feature sawtooth oscillations.
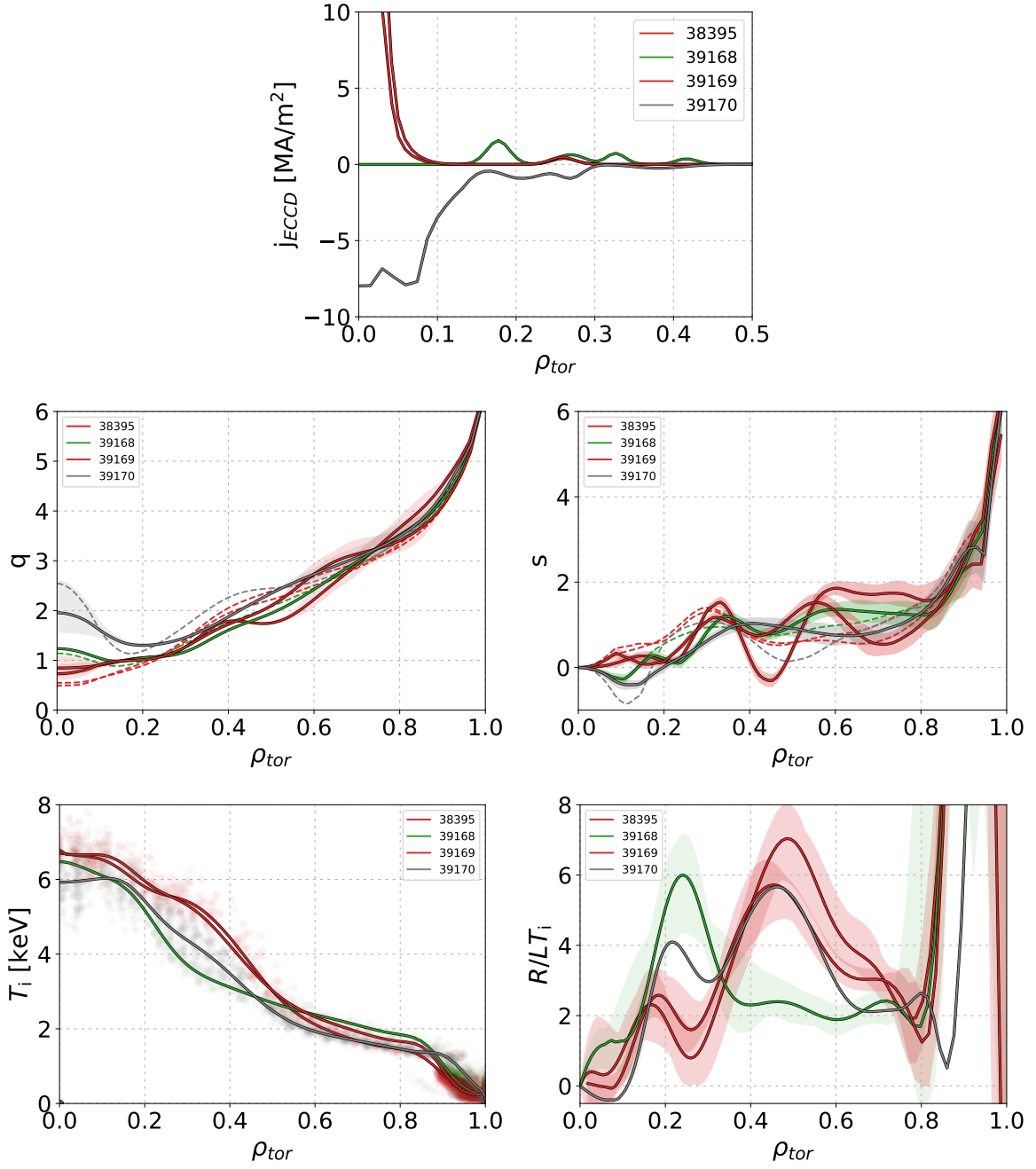
Figure 5.7: Ensemble of profiles comparing the effects of applying ECCD with different settings in several different AUG discharges. T_i and R/LT_i are fitted with IDI, q and s are reconstructed with IDE, taking IMSE data into account. The IMSE offset is based on discharge #38571, with the profiles using the offset based on #39587 being added with dashed lines for comparison.

A notable feature of the counter-ECCD discharge and more so the two-gyrotron co-ECCD discharges, is that the region where the T_i steepening is largest is shifted further off-axis compared to the two scenarios discussed so far; while the weakly and strongly off-axis ECCD scenarios have their steepest region around $\rho_{\text{tor}} = 0.2$, the new scenarios feature this region of reduced transport around $\rho_{\text{tor}} = 0.5$. Looking at the R/L_{T_i} plot in figure 5.7, however, for the counter-ECCD discharge, a smaller local maximum can also be observed around $\rho_{\text{tor}} = 0.2$.

Concentrating on the transport in this region for the moment, the data seems in general consistent with the theory that a negative s is connected with the suppression of transport: Both scenarios that feature peaked temperature profiles – strongly off-axis ECCD and counter-ECCD – have also a significant negative shear in the core, with $s = 0$ located around $\rho_{\text{tor}} = 0.2$. Meanwhile, the two-gyrotron case, for which s remains strictly > 1, R/L_{T_i} remains at a low level that does not imply a reduction of transport. However, in the counter-ECCD case, the logarithmic ion temperature gradient is lower compared to the strongly off-axis ECCD scenarios, despite the shear being slightly more negative. So if there is indeed a connection between negative magnetic shear and reduction of transport, this behaviour might saturate such that the precise value of $s < 0$ does not play a significant role.

Looking at the region around $\rho_{\text{tor}} = 0.5$, the data is generally in line with the theoretical predictions according to which the reduction of transport comes from fast ion effects, whose strength depends also on q and s. Both scenarios that feature increased values of R/L_{T_i} in this region – counter-ECCD and two-gyrotron – feature generally also higher values of q compared to the "off-axis" scenario. Though it should be noted that one of the two-gyrotron discharges – #38395 – actually has a comparatively low q, along with a locally strongly reduced s that goes down to values of $s < 0$. At the same time, it has an even higher R/L_{T_i} than the other two-gyrotron discharge. It is not fully clear if the local increase in R/L_{T_i} is in fact related to the strongly reduced s, or if this curving of the q-profile is perhaps not actually real due to IMSE offsets not being determined correctly.

It should also be mentioned that in both #38395 and #39169, the steepening of T_i only appears for short times of $\sim 100\,\text{ms}$ before the discharge disrupts or they disappear following a change in the heating mix. It is conceivable that the steepening of T_i is only transient in this scenario and does not actually represent a reduction of transport in the sense that is under investigation in this work.

To summarize, from experiments and simulations comparing the weakly and strongly off-axis ECCD scenarios, one can conclude that it is indeed the variation in the q-profile that causes the steepening of T_i in the plasma core. While the data is not sufficient to pinpoint the exact mechanisms behind this with certainty, they are consistent with theoretical predictions that the reduction of transport is caused by fast ion effects that are strongly dependent on the exact values of q and s. Additionally, the data seems to point in the direction that negative values of s seem to also play a role in the reduction of transport. Though a correlation between the absolute value of $s < 0$ and a stronger

reduction of transport is not observed. For a more definitive answer, more experiments with a wider variety in q and s are needed for which reliably calibrated IMSE data are available. To rule out systematic errors on the IMSE data, systematic studies of the stability of the IMSE calibration over a broader variety of scenarios are necessary.

5.4   Improving reduced simulations with heuristic model

It was already discussed in section 2.6 that ASTRA/TGLF is in general not capable of accurately describing the scenarios with peaked ion temperatures under investigation in this work. Although in that section it was also shown that for one particular discharge (AUG #32305) a match between simulation and experiment could be achieved by increasing the $E{\times}B$-shear, in chapter 4 it was found that in reality the $E{\times}B$-shear does not actually have a significant effect on the observed reduction of transport. For the cases under investigation here, $E{\times}B$-effects seem to be overestimated while in turn the real effects behind the stabilization of the ITG appear to be underestimated. In the reference case #32305, these two faults apparently happen to compensate each other, but this can of course not be expected for the general case. The setup described in 2.6 can therefore not be used to extrapolate to different scenarios or devices. Earlier in this chapter, it was instead shown that the specific shape of the q-profile plays an important role in the reduction of transport. Though the experimental evidence is not conclusive enough to make definitive statements about parameter dependencies. In this section, an attempt is done to modify TGLF in such a way that these missing q-profile effects could be included, such that it is possible to accurately describe the plasma scenarios investigated in this work. This approach would not only allow to use ASTRA/TGLF for the further development and study of these scenarios, it would also provide some more insight on the exact role of the q-profile in the reduction of turbulent transport.

The general approach to this is relatively simple: Similar to how the $E{\times}B$-shear effects could compensate the missing stabilizing effects, one can mimic the missing effects by re-purposing other stabilizing effects that are already included in TGLF; In fact, one could even directly use the $E{\times}B$-shear for this purpose. Instead, a simpler approach was chosen here that makes use of the dilution effect. To this end, an additional – artificial – impurity is added to TGLF, that has a density which is set to be proportional to the cumulative strength of the missing effects. This way, the artificial dilution of the main ion species causes a reduction of the heat fluxes TGLF gives as output, to values that match – or at least come close to – the experimentally measured heat fluxes. It is important to note here that this artificial impurity is only included in TGLF such that the main ion population, and therefore the drive of the ITG, is reduced. There is no heat flux attached directly to this impurity, and inside ASTRA itself everything remains unchanged – with the exception of the modified ion heat flux it gets from TGLF. A rudimentary implementation of this approach has previously been published in [116].

In a bit more detail, in the TGLF source file "tglf_interf.f90" two lines are adjusted that

modify the main ion density (gradient) to ensure quasi-neutrality is fulfilled. These are

```
tglf_as_in(2) = -1./tglf_zs_in(2)*
        (SUM(tglf_as_in*tglf_zs_in) - tglf_as_in(2)*tglf_zs_in(2))
```

and

```
tglf_rlns_in(2) = -1./(tglf_as_in(2)*tglf_zs_in(2))*
        (SUM(tglf_rlns_in*tglf_as_in*tglf_zs_in) -
            tglf_rlns_in(2)*tglf_as_in(2)*tglf_zs_in(2))
```

where "tglf_as_in", "tglf_zs_in" and "tglf_rlns_in" are lists containing the density, charge and logarithmic density gradient of all species, with "tglf_as_in(2)" etc. referring to the main ion species. In these two lines, the artificial impurity is added to the sums over all species, resulting in the main ion density and density gradient to be adjusted down. In the setup used, the charge of the artificial impurity is set to 6, which is chosen completely arbitrary. Any other charge would be valid, as long as the rest of the heuristic formula is scaled accordingly.

Based on a database of 17 distinct flat-top time-intervals from discharges that were performed over the course of this work, a formula that allows to describe these scenarios reasonably well has been found:

$$
\begin{aligned}
n_{\text{imp}} = 16.44 \cdot 10^6 \cdot p_{\text{fast,D}}^2 + \\
70.36 \cdot 10^3 \cdot \text{Step}\big(47.98(q - 1.111)\big) \cdot \text{Step}(-4.399 \cdot s) \cdot p_{\text{fast,D}}
\end{aligned}
\tag{5.1}
$$

where n_{imp} is the density of the artificial impurity and $p_{\text{fast,D}}$ is the pressure of the deuterium fast ions. The function "Step" is defined as

$$
\text{Step}(x) \coloneqq 0.5 + \frac{1}{\pi} \arctan(x),
\tag{5.2}
$$

a simple representation of a smooth step-function.

This heuristic formula has been found with the following approach: First, for each discharge individually, parameter-scans were performed to find a local optimum, where the choice of n_{imp} leads to the best match between the experimental and simulated ion temperatures $T_{\text{i,exp}}$ and $T_{\text{i,sim}}$. To quantify how good the match between simulation and experiment is, the average normalized deviation from the experimental data

$$
d = \frac{1}{N} \sum_{0.1 < \rho_{\text{tor}} < 0.7} \frac{|T_{\text{i,sim}} - T_{\text{i,exp}}|}{T_{\text{i,exp}}}
\tag{5.3}
$$

is calculated. Here, N is the number of points in the interval $0.1 < \rho_{\text{tor}} < 0.7$. This interval was chosen to exclude points in the very core where TGLF is generally not reliable, and to exclude points outside or close to the boundary where ASTRA does not actually calculate the profiles.

In a second step then, a formula applicable to the entire database $n_{\text{imp,all}}$ is found by minimizing the difference to the individual formulas $n_{\text{imp,single}}$ for each discharge at once

$$\frac{1}{N_{\text{shots}}} \sum_{\text{shots}} \frac{1}{N} \sum_{0.05 < \rho_{\text{tor}} < 0.8} \frac{\left| n_{\text{imp,single}} - n_{\text{imp,all}} \right|}{n_{\text{imp,single}}}. \tag{5.4}$$

This optimization was done with the minimize function of the python package scipy.optimize, using the Nelder-Mead method [117].

In general, this formula 5.1 is consistent with the findings in [69], in that they are proportional to the fast ion population, with modifications coming from q and s. An important difference to note is that in this formula only the deuterium fast ions are considered. For cases with ICRF, the hydrogen population is neglected. This is because there are a number of cases similar to #35938, where the temperature profiles change only little while the fast ion pressure is significantly increased by the addition of ICRF heating. Taking the full fast ion pressure, it was not possible to simultaneously match both cases. This can be explained with the findings of the GENE simulations of #35938 in section 4.3: According to them, anisotropies in the temperature profiles play an important role. In particular the fast ion driven modes that interact with and stabilize the ITG seem to be driven predominately by the component parallel to the magnetic field, which is relatively small in the case of the hydrogen species ($T_\perp/T_\parallel = 3.4$). So while the total fast ion pressure changes strongly in the case of hydrogen, the component that is actually important changes only relatively little.

Whats more, in [69], the relevant parameters are actually $T_{\text{fast}}/T_{\text{e}}$, R/LT_{fast} and R/Ln_{fast} instead of simply p_{fast}. The fast ion dependence in 5.1 is therefore likely too simplistic, though it yields reasonable results. Finding a more sophisticated formula that better represents the actual physics would require a broader database as well as the performance of more systematic parameter studies with GENE, which was beyond the scope of this work.

The q-term inside the smooth step-function indicates that there is a threshold above which the stabilizing effect becomes relevant. In fact, as described in section 2.4.3, [69] finds a threshold in pressure above which the fast ion modes are excited, leading to the stabilization of the ITG. This threshold is dependent on q, which means in turn, for a given β, there is indeed a value of q above which transport should be reduced. For a more accurate formula, this threshold should not be constant but dependent on β. As the shear dependence in [69] is not fully conclusive, the inclusion in equation 5.1 represents mainly the observation that a negative magnetic shear seems to have a stabilizing effect, that does, however, not seem to depend on the absolute value of $s < 0$. Again, for a more accurate description, further investigations are required.

Despite these avenues for improvement discussed, the heuristic formula in its current form already allows to accurately describe a relatively wide range of scenarios. In figure 5.8, T_i profiles of 4 different shots are depicted, comparing simulations with and without the addition of this heuristic model to the experimental profiles. In appendix D, the results of the remaining simulations that were performed can be found. It should be noted here, that in many of these simulations numerical instabilities occurred, that lead to transport coefficients that are locally orders of magnitude higher than the experimental values. These instabilities seemed to occur mainly inside the radius where $s = 0$.

In these TGLF simulations, the new saturation rule "SAT2" was used [74]. The input powers used in the simulations were calculated by TORBEAM in the case of ECRH and by TRANSP/NUBEAM and TRANSP/TORIC in the case of NBI and ICRF. Radiation losses were estimated based on the measured tungsten concentrations. For the initial conditions, an average over the time-intervals indicated in appendix D, was used; The boundary was set to $\rho_{\mathrm{tor}} = 0.75$. For the input for v_{tor}, the fit from IDI was used, based on
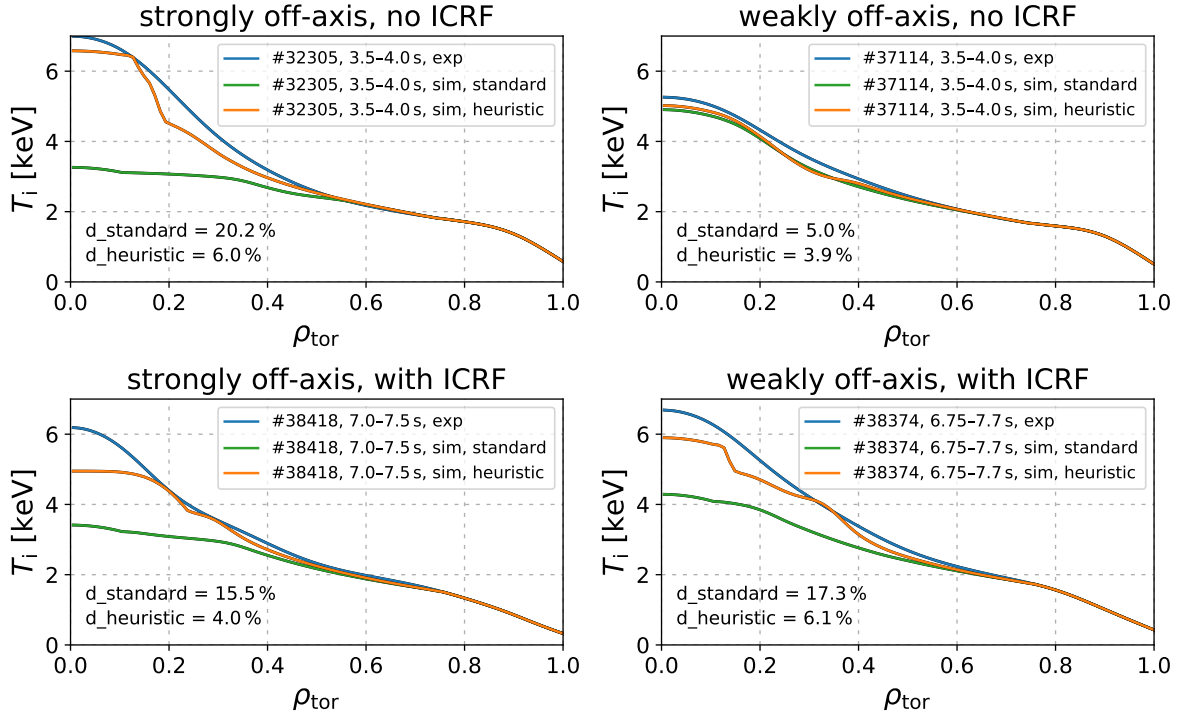

Figure 5.8: Ion temperature profiles resulting from TGLF simulations of four different discharges covering all combinations of weakly/strongly off-axis ECCD and with/without ICRF heating. For each discharge, simulations with the inclusion of the heuristic model (orange) and without (green) are compared to the experimental profiles (blue). To quantify how much of an improvement the heuristic model is, an average normalized deviation d is given.
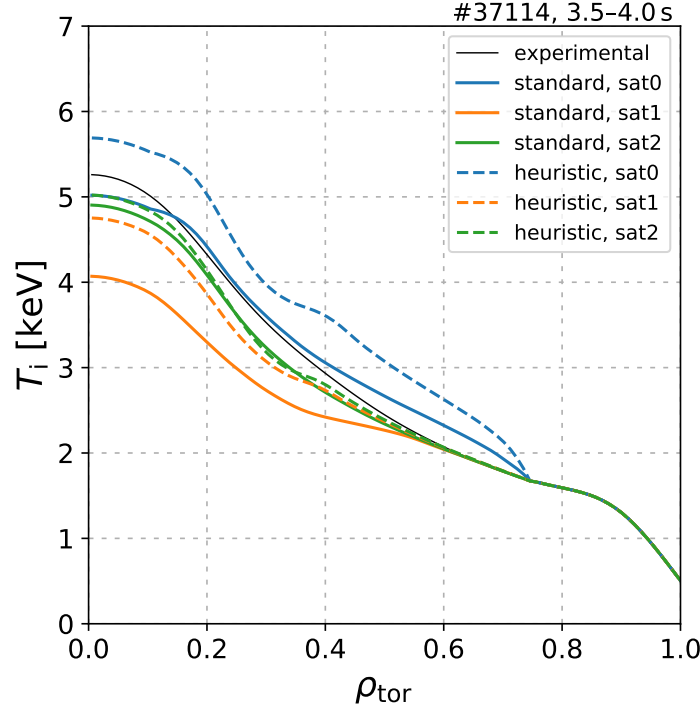
Figure 5.9: Ion temperature profiles of the discharge #37114, resulting from TGLF simulations using different saturation rules. For comparison, also the results with the heuristic formula using different saturation rules is shown with dashed lines.

impurity CXRS measurements. Neoclassical corrections to obtain the main ion rotation were not done, leading to the the rotation being underestimated by approximately $5-10\,\%$.

As can be seen in figure 5.8 and appendix D, many of the standard simulations strongly underestimate the ion temperatures, giving a factor of d in the range of $15-20\,\%$. Compared to that, the simulations with the heuristic model are significantly closer to the experimental profiles, giving mostly factors of $d \approx 5\,\%$. Notable exceptions are the weakly off-axis case without ICRF in figure 5.8 (#37114, 3.5–4.0 s) and other cases similar to it. For these cases, also the standard simulations provide a good match that is equally good as with the heuristic model.

It should be noted here, that this good match is only possible with the most recent version of TGLF, using the saturation rule SAT2. As can be seen in figure 5.9, simulations using the older saturation rules SAT0 and SAT1 match the experimental profiles less good. While SAT1 leads to an overall overestimation of the heat transport, SAT0 actually underestimates the transport in the edge, partially compensating the error further towards the core.

These significantly different results, depending on which saturation rule is used, provide a good insight of the potential for further improvements in future versions of the code.

While the proposed heuristic model is partially physics based and allows to gain some insight into the processes behind the observed reduction of transport in non-inductive advanced scenarios, it is still only a provisional workaround. In the long term, the effects that seem to be missing in scenarios such as the ones investigated in this work need to be actually implemented in TGLF and similar codes. The investigations in this work can hopefully be of use in such efforts.

6 Summary and Outlook

In recent years, scenarios have been developed in AUG that feature many properties that are desirable for future fusion power plants. These include excellent confinement, improved stability and a plasma current that is almost completely non-inductively driven. A notable feature of these scenarios is that their core ion temperatures are significantly elevated, to values that exceed what theory would predict. To further develop these attractive scenarios and be able to extrapolate their performance to larger future machines, it is vital to be able to describe them with numerical tools – in particular reduced models that allow for simulations to be finished in relatively short time. However, when doing simulations with the quasilinear model TGLF, it was found that achieving a match with the experimental ion temperature profiles is challenging. In cases where a good match could be achieved with TGLF, the quantity responsible for the reduction of transport seems to be the $E{\times}B$-shear, which is in contradiction with the results of the more powerful gyrokinetic code GENE. (For details on this, see section 2.6).

To resolve this discrepancy and to provide a broader basis for understanding what effects really play a role in the reduction of turbulent transport, various experiments have been performed over the course of this work. One big block of experiments focused on varying $\omega_{E{\times}B}$ to study if this really has an effect on the ion temperature gradients, like TGLF seems to suggest. In these experiments, great care has been taken to determine the $E{\times}B$-shear not only based on the toroidal rotation v_{tor}, but also to consider the smaller contributions from v_{pol} and the diamagnetic term (see section 4.1). In these experiments, no correlation between $\omega_{E{\times}B}$ and R/L_{T_i} could be found (see section 4.2). To rule out potentially competing effects – for example from the fast ion population –, that might mask a dependence on the $E{\times}B$-shear, non-linear GENE simulations have been performed to disentangle $\omega_{E{\times}B}$ from other effects. Also with these simulations, it was found that the $E{\times}B$-shear does not seem to play a role in the observed ion temperature peaking (see section 4.3).

In further experiments, instead, a strong dependence on the q-profile becomes evident. This could be demonstrated by a significant change in the T_i-profile after modifying the ECCD settings during a discharge (see section 5.1). These experiments have also been supported by non-linear GENE simulations, that allowed to rule out the possibility that the observed change in T_i actually stems from a change in T_e/T_i (see section 5.2). Unfortunately, attempts to determine which aspects of the q-profile are responsible for the reduction of transport

did not lead to a conclusive result. This is because achieving arbitrary variations in the q-profile and determining it with sufficient precision is technically very challenging and could only be achieved for a small number of discharges. In particular the latter part – obtaining q-profiles with very small uncertainties – turned out to be very difficult, since the requirements for achieving a good IMSE calibration are in conflict with the general design of the experiments performed in this work. Attempts to achieve a good calibration regardless lead to partially contradicting results that could not fully be resolved (see appendix A).

Nevertheless, from the experiments where the q-profile could be determined with great precision some general trends could be observed that are in line with theory (see section 5.3). On the one hand, the experiments seem to indicate that a negative magnetic shear plays an important role in the observed reduction of transport. Furthermore, they seem in general consistent with recent theoretical findings, that the reduction of transport is caused by the coupling of the ITG mode to subdominant fast ion driven modes, causing a stabilization of the ITG [69]. According to these studies, the behaviour of the fast ion driven modes is very sensitive to q and s, such that both higher values of q and lower values of s lead to reduced transport. These trends match in general the experiments that were done in this work, and are also in line with the GENE simulations that have been performed.

To further investigate these dependencies of q and s and to tackle the challenge posed at the beginning of this thesis, attempts have been done to modify TGLF such that these fast ion and q-profile effects are included and the non-inductive advanced scenarios that are studied in this work can be accurately described. To this end, a heuristic model has been developed that mimics the missing stabilizing effects via the dilution effect of an artificial impurity whose density is proportional to said effects (see section 5.4). While there are still several points that could be improved with the formula that has been found to work best in the end, it still delivers reasonable results on a small database of discharges. The dependence on q and s and p_{fast} in this heuristic model is generally in line with the experimental findings described earlier.

In future works, several remaining open points should be investigated in more detail: For one, more systematic variations of the q-profile should be done, to provide a more robust basis for investigations of the effects from q and s. Such experiments could include a scan where the value of q_{min} is kept constant, but its position is varied, or scans where the q-profile is shifted upwards, keeping its shape constant, such that only q is varied but s remains fixed. Such studies will be more feasible in the future, due to ongoing efforts at AUG to develop tools to allow the prediction and real-time control of the plasma current profiles. Such studies must be accompanied with a more robust calibration of IMSE data, requiring systematic studies of how the IMSE offsets change over time, and if they vary with different plasma scenarios.

Secondly, beyond the effects from q and s, the GENE simulations performed for this work suggest that the root cause for the reduction of transport are subdominant modes driven by fast ions. In particular, in the simulations of discharges where ICRF was used, the inclusion

of both deuterium and regular hydrogen fast ion species is necessary. In contrast to that, in our experiments a strong increase in fast ion pressure after the ICRF is activated does not seem to have a big effect on T_i. This is also reflected in the heuristic formula that was used to modify TGLF such that these experiments could be properly reproduced. An explanation for this is that it seems to be mainly the component parallel to the magnetic field that drives the fast ion modes that couple with the ITG and stabilize it that way. Meanwhile, the additional fast ion pressure from the ICRF has a large perpendicular component, suggesting that the component of the fast ion pressure that is actually important changes only relatively little. To test this theory, further experiments would be useful, where the fast ion profiles and distribution functions are systematically varied while keeping everything else constant. This could for example be done by replacing very radial NBI sources with ICRF, since that should not affect v_{tor} as much, or possibly by changing the ICRF heating scheme.

Based on a database of such experiments, and additional parameter studies with GENE, the heuristic model with which TGLF was modified to be able to simulate these scenarios, should be extended, to have a more solid physics basis. In particular the dependence on the different fast ion species is probably too simplified in its current form. It would also be important to make sure that such a model also works for simulations of experiments performed at other machines, such as DIII-D or JT-60SA, where similar scenarios are (or will be) under investigation. Only if results of predictive models can be transferred to other devices (in particular of larger size, such as JT-60SA), can they be used to develop scenarios for future machines.

Finally, it would also be very interesting to develop the scenarios further, for which the steep gradient region is shifted closer to the edge. Besides the general improvement in performance this would bring, in such scenarios it would also be possible to measure directly fluctuations from the ITG driven turbulence. While the steep gradient region in our standard scenarios is too far into the core for the diagnostics used to measure turbulence directly – the correlation-ECE or doppler-reflectometry – for these shifted profiles, measurements are possible. This would allow to more directly study how turbulence is suppressed in these scenarios and would provide valuable data that could be used to benchmark GENE simulations.

Appendix

A   Challenges in obtaining the IMSE offset

At the end of section 3.2.7, some challenges with the calibration of the IMSE data obtained during the experiments conducted in this work, were briefly touched upon. In the following, these are discussed in more detail.

In the example shown in figure 3.8, the calibration could very easily be done, as IMSE data was available for the majority of the discharge; between 1.9 s and 6.7 s. During the entirety of this duration, also sawtooth-oscillations could be observed. In the experiments that are discussed in this work, generally neither of these points is true, making the use of the IMSE challenging. As stated in section 3.2.6, IMSE data can only be obtained if exactly one of the NBI beams 5, 7 or 8 is used – ideally one of the latter two. This poses a challenge, as in principle both source 7 and source 8 are needed for the experiments performed for this thesis. Source 7 is indispensable, as it adds a significant portion of off-axis plasma current, which is vital in obtaining the desired shape of the q-profile. Source 8 on the other hand provides in principle better IMSE data, as measurements with source 7 do not cover the very core of the plasma. Furthermore, source 8 also provides CXRS measurements at the high field side (which is needed for determining v_{pol}) and the plasma edge, for discharges with increased wall clearance. To resolve these contradicting requirements, short *beam notches* are employed, where one of the two IMSE relevant NBI sources is briefly turned off – typically for 50 ms. As this time is smaller than the energy-confinement time and the current diffusion time scale, the plasma is not unduly disturbed by this. In first attempts on using this approach, source 7 was briefly turned off, while in later experiments this was done with source 8 instead, to minimize the risk of disturbing the plasma by interrupting the current drive.

In figure 6.1 an example of a discharge featuring such 50 ms beam notches of NBI source 7 is shown. As can be seen from characteristic quantities – such as the stored energy in the plasma W_{MHD}, β_{pol} and β_{N}, as well as H_{98} – it is possible to perform beam notches where source 7 and its associated current drive are deactivated, without disturbing the plasma. In the same figure, also the resulting q-profiles obtained during those short phases are shown.
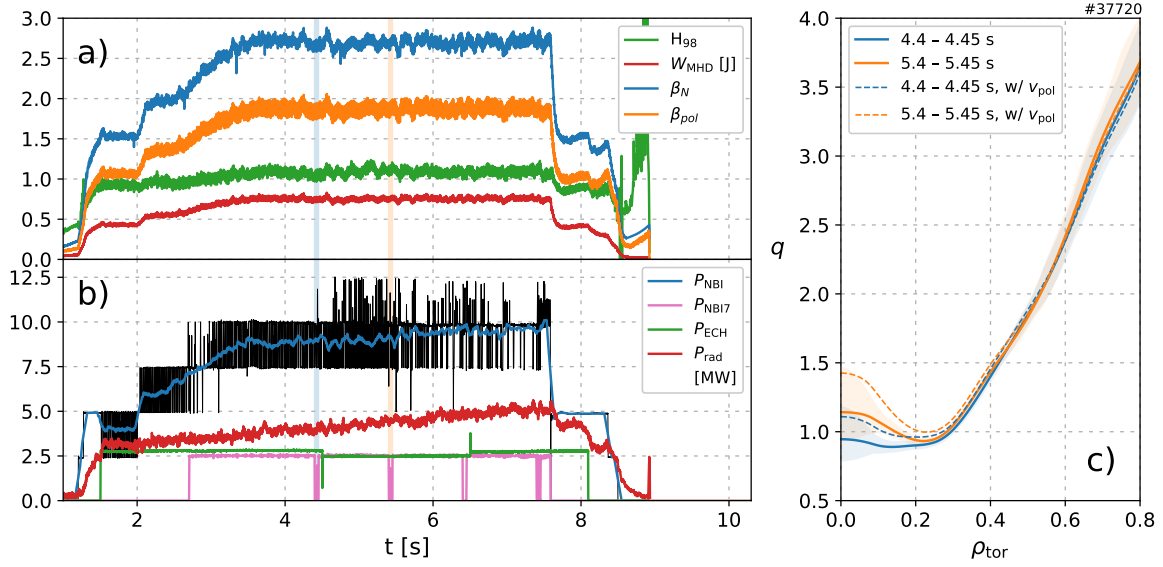
Figure 6.1: Overview of a AUG discharge featuring short beam notches to obtain IMSE data (#37720). In subfigure a) time-traces of parameters characterizing the plasma performance are shown, which remain unperturbed by the beam notches. In subfigure b) an overview of the heating power, and the power radiated away is given. In pink, the power from NBI source 7 is explicitly shown; The times where it was deactivated and IMSE data could be obtained are shaded in blue and orange in both subfigure a) and b). In subfigure c) the corresponding q-profiles obtained in these time-intervals are shown. Here, solid lines represent the standard evaluation, dashed lines include an estimate for the v_{pol} contribution to the background electric field.

Additional to the profiles coming from the regular IMSE evaluation, shown with solid lines, also an estimate of profiles obtained when considering the contribution of v_{pol} to the background electric fields is shown in dashed lines. As can be seen, these profiles lie slightly outside the error-estimates for the standard profiles, suggesting that the v_{pol} contribution should be considered. However, these dashed profiles represent actually only upper limits to the deviation the v_{pol} contribution can cause, since v_{pol} was not considered in the determination of the offsets. Assuming v_{pol} is of the same magnitude in the sawtoothing phase, its contribution is already partially considered in the calibration. Furthermore, for this estimation, a constant value of $v_{\mathrm{pol}} = 5\,\mathrm{km/s}$ was assumed, which is above the actual value for most radial positions. For these reasons, the actual systematic error from neglecting v_{pol} must be smaller and therefore still within the errorbars. It can therefore be justified to neglect this term.

In normal operation, it takes the IMSE at least $60\,\mathrm{ms}$ to collect enough data from all channels for a sufficiently good signal. To accommodate for the shorter measurement time, not all channels are read out, skipping rows at the top and bottom of the camera image.

The next challenge, after having successfully obtained IMSE data, is to do the calibration of this data, by determining and subtracting the arbitrary offset. In general, all plasma discharges discussed in this thesis feature increased values of the safety factor q that are typically above unity. As a consequence, the discharges often do not feature any sawtooth oscillations, making a calibration impossible. Of course, the avoidance of sawteeth improves the stability of the discharge and is precisely one of the reasons why the q-profiles are shaped the way they are in the first place, but regarding the use of IMSE data, it makes things more complicated. In some cases, small and irregular sawteeth appear intermittently, in particular at the beginning of the discharge, such that the offset could be determined (such a discharge is for example shown in figure 6.1). For the other discharges without any sawteeth, the approach to the calibration needs to be adjusted. To be able to calibrate the IMSE data anyways, the typical approach is to use offsets from different discharges – ideally ones that were performed on the same day. This approach is of course only viable if one can assume that the offset on the IMSE angles changes only very slowly with time.

Indeed, systematic investigations of these offsets during the 2020/2021 experimental campaign of AUG on so-called *Standard H-mode* benchmark discharges reveal that this assumption seems to be valid – at least for measurements taken with NBI source 8 [118].

On the left-hand side of figure 6.2, an overview is given of how the offset of each IMSE channel changes over the course of several months, for measurements performed using NBI
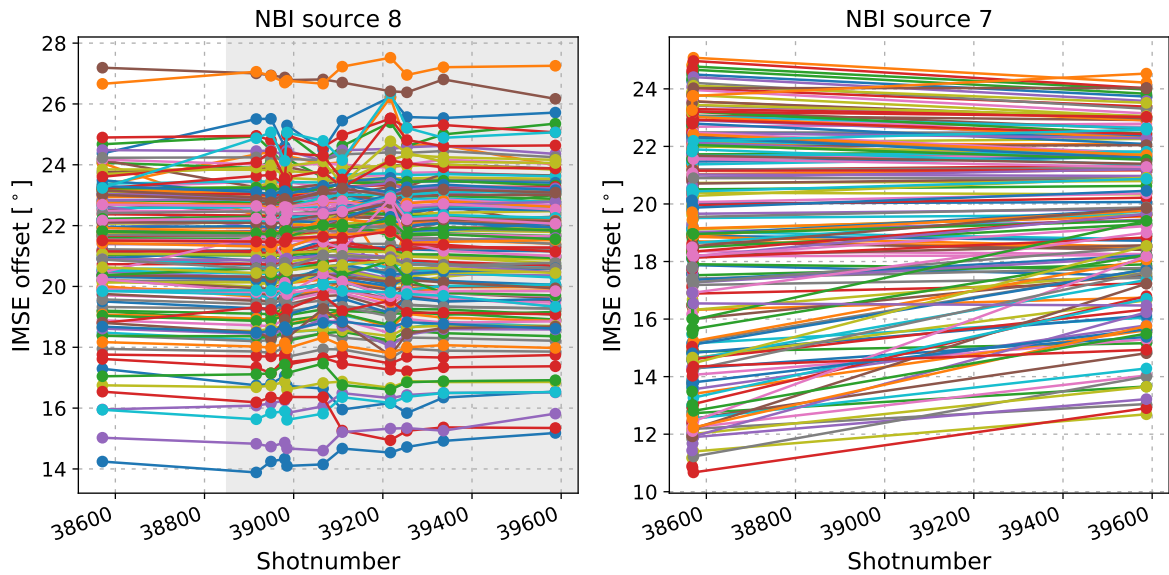

Figure 6.2: Overview of how the offset of each IMSE channel develops over the course of several months. On the x-axis, the consecutively numbered AUG discharges are listed, which occurred between February and July 2021. Left: IMSE measurements using NBI source 8. Offsets from discharges highlighted in grey are combined in one average offset; Right: IMSE measurements using NBI source 7.

source 8. It can be seen that the offsets remain remarkably constant over this time-period. From this dataset, a mean offset was determined, that could be used to calibrate any discharge performed in the 2020/2021 experimental campaign using source 8. From the scatter of the individual offsets, an uncertainty for each channel could be deduced, which is taken into account in the equilibrium reconstruction performed with IDE.

Since the offset for source 8 remains constant, it stands to reason that the same is true also for measurements using source 7. If one could determine the IMSE offset for several suitable source 7 discharges, another universal offset should be possible to obtain. Unfortunately, the number of discharges that have only source 7 active, without source 5 or 8, and that at the same time have longer phases with sawteeth are very rare. In fact, for the 2020/2021 experimental campaign, only three discharges could be found that one could use for these purposes. Whats more, these discharges were also performed on the same day and are for the purposes here repeats of each other, meaning only one datapoint for the calibration of source 7 IMSE measurements is available.

To improve the statistics, a dedicated plasma discharge was performed, similar to the standard H-mode discharges that were used to calibrate IMSE data measured using source 8; the difference to those discharges being that source 8 was alternated with source 7 in $0.5\,$s intervals. When now using the source 7 phases of this discharge to determine the IMSE offset, the result significantly deviates from the offset determined on the three other experiments. This can be seen on the right-hand side of figure 6.2. In figure 6.4 c, furthermore, an example for q-profiles resulting from IDE evaluations is shown, using one or the other source 7 offset. There is clearly a strong deviation between the two profiles. As there is no reason that the offset for one source should change so much over time, while the offset for the other source remains approximately constant, it stands to reason that one of these two offsets (or both!) are not correct.

As can be seen in figure 6.3, all discharges used for the calibration of source 7 IMSE measurements also contain phases from which one can calculate the offset for the source 8 measurements. By comparing these offsets with the previously determined source 8 offsets, one can rule out the possibility that the discharges in question are outliers – for example because the sawteeth might not behave as the flat current model would predict. This is shown in figure 6.2, where the discharges in question correspond to the left- and rightmost sets of points on the left-hand side. While the offset values for #39587 are in very good agreement with the offset-angles from the other standard H-modes, the offsets from discharge #38571 show some deviations. However, when comparing the q-profiles from IDE reconstructions of #38571, taking either the universal offset or the offset determined from the sawtoothing phase of this discharge into account, one finds the profiles to be identical within the uncertainties. This is shown in figure 6.4 a

One explanation for the fact that for the two discharges, the offset for source 7 deviates strongly while the offsets for source 8 are consistent, is that the additional current drive when using NBI source 7 affects the sawtooth behaviour such that it can no longer be described by the models used in IDE. This possibility, however, has been checked and can
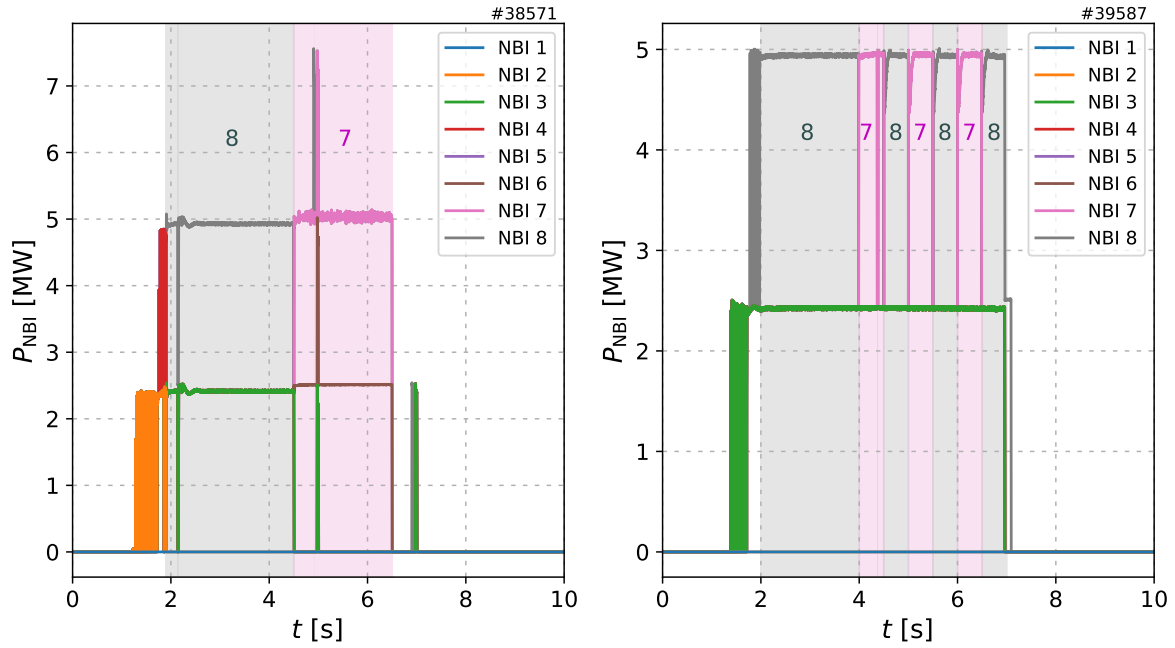
Figure 6.3: NBI sources used for discharges where determination of IMSE offsets is possible. Left: AUG #38571 with one source 8 phase, followed by one source 7 phase. Right: AUG #39587, alternating phases using source 8 and 7, each 0.5 s long, respectively.

be ruled out [119]. Nevertheless, to avoid such influences by unusual modes appearing in the presence of strong current drive, for the discharge #39587 an alternate approach to calibrate IMSE data could be applied that does not rely on the existence of sawteeth. As this discharge uses only one of the two off-axis sources (unlike #38571, that uses both sources 6 and 7) and has a relatively high line-averaged density of 8.4×10^{19} m^{-2}, the overall current drive is relatively low. Because of that, the q-profile is not expected to change significantly between the alternating source 7 and 8 phases. Now, since the offset for the source 8 phases has already been determined, one can assume the profiles in these phases to be correct. Since the profiles do not change significantly in the alternating source 7 phases, it is a reasonable assumption to trust the constraints of the current diffusion equation in this case, and use the resulting profiles as basis for the determination of the source 7 offset. The source 7 offset determined with this method is consistent with the offset based on the regular sawtooth-method, further supporting it. In figure 6.4 b, a comparison between the source 7 and source 8 phases in this discharge is shown, as well as a comparison between the profiles with and without adding IMSE as constraint in the IDE evaluation.

As this discrepancy between the two different offsets for source 7 could not be resolved by finding an error with one and excluding it thus, the profiles obtained with source 7 IMSE need to be carefully discussed. In chapter 5, both contradicting profiles are therefore considered, though by comparing the resulting profiles with profiles from similar experiments, the one more likely correct can be deduced.
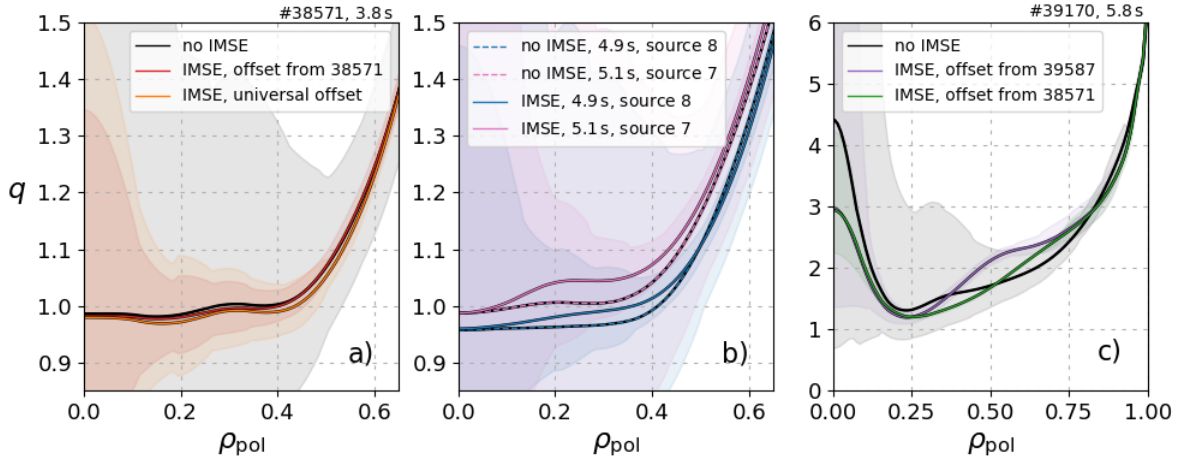
Figure 6.4: *q*-profiles reconstructed with IDE. Left: Source 8 phase of #38571, comparing IMSE data calibrated with different offsets and profile not taking IMSE into account; Middle: Comparison of source 8 and source 7 phases of #39587, with and without IMSE; Right: Comparison of profiles using source 7 IMSE data calibrated with different offsets, compared to profiles without IMSE data included.

While finalizing this work, a likely explanation has been found for the the discrepancy of the two source 7 offsets: While the NBI beam of source 6 is not directly in the field of view of the IMSE camera, it seems that stray light from this NBI beam can still affect the IMSE measurements. As only one of the two shots used to calibrate the source 7 IMSE measurements uses also source 6, this can explain the difference [120].

B   Detailed list of experiments

shot#	time	ρ_{tor}	colour	symbol
35938	3.5–3.8 s	0.15	light blue	half
	5.1–5.5 s	0.15		half
36160	3.5–3.7 s	0.235	orange	half
	5.1–5.3 s	0.25		half
38374	3.5–4.5 s	0.22	green	half
	4.7–5.5 s	0.22		half
	6.7–7.7 s	0.22		half
38381	3.5–4.6 s	0.205	red	half
	4.7–5.2 s	0.205		half
	6.5–7.0 s	0.18		half
38383	3.7–5.3 s	0.18	purple	half
	7.5–8.2 s	0.34		half
37114	3.5–4.0 s	0.235	brown	half
	5.1–5.2 s	0.15		full
	5.3–5.5 s	0.23		full
	6.3–6.5 s	0.28		full
37712	4.0–4.4 s	0.28	pink	half
	4.7–5.4 s	0.28		full
	5.7–6.4 s	0.28		full
37720	3.6–4.4 s	0.29	grey	half
	5.2–5.4 s	0.25		half
37105	6.0–6.2 s	0.25	dark blue	full
	6.5–6.8 s	0.225		full
37711	3.5–4.0 s	0.17	black	full
	5.3–6.2 s	0.19		full
37724	3.8–4.0 s	0.24	cyan	full
	5.8–6.25 s	0.235		full
	6.6–6.9 s	0.235		full
38418	3.5–4.1 s	0.18	magenta	full
	4.6–4.8 s	0.18		full
	5.1–5.3 s	0.18		full
	7.0–7.5 s	0.18		full
	8.0–8.9 s	0.18		full

Table 6.1: Full list of shots displayed in figure 4.6.

shot#	time	IDE-settings
weakly off-axis ECCD		
37720	4.4–4.45 s	rmaxi:IDE, ed. 5
	5.4–5.45 s	
37712	4.4–4.45 s	rmaxi:IDE, ed. 4
strongly off-axis ECCD		
37724	3.9–3.95 s	rmaxi:IDE, ed. 5
38418	3.8–3.85 s	rmaxi:IDE, ed. 7
	4.3–4.35 s	
	4.8–4.85 s	
	5.25–5.3 s	
	7.0–7.05 s	

Table 6.2: Full list of shots displayed in figure 5.5. The "strongly off-axis ECCD" cases are also shown in figure 5.6.

shot#	time	IDE-settings
IMSE offset based on 38571		
38395	5.45–5.7 s	rmaxi:IDE, ed. 6
39168	4.55–4.8 s	rmaxi:IDE, ed. 18
39169	6.3–6.4 s	rmaxi:IDE, ed. 23
39170	5.4–6.0 s	rmaxi:IDE, ed. 21
IMSE offset based on 39587		
38395	5.45–5.7 s	rmaxi:IDE, ed. 7
39168	4.55–4.8 s	rmaxi:IDE, ed. 17
39169	6.3–6.4 s	rmaxi:IDE, ed. 22
39170	5.4–6.0 s	rmaxi:IDE, ed. 20

Table 6.3: Full list of shots displayed in figure 5.7. Both profiles of #39168 are also shown in figure 5.6.

C   List of inputs for GENE simulations

q	s	T_e	T_i	T_fast	R/LT_e	R/LT_i	R/LT_fast
1.02	0.48	3.82	3.14	31.2	1.75	1.75	0.65

$\omega_{E\times B}$	β_e	n_e	n_i	n_fast	R/Ln_e	R/Ln_i	R/Ln_fast
0.022 / 0.013	0.015	5.27	4.58	0.70	0.91	1.03	0.14

Table 6.4: Input values for GENE simulations of #35938 at 3.5 - 3.8 s. Results are depicted by blue points in figure 4.11. Between the two simulations, only $\omega_{E\times B}$ was varied.

q	s	T_e	T_i	T_fast	R/LT_e	R/LT_i	R/LT_fast
1.09	0.51	4.03	2.80	31.4 / 40.3	2.0	1.6	0.49 / 8.70

$\omega_{E\times B}$	β_e	n_e	n_i	n_fast	R/Ln_e	R/Ln_i	R/Ln_fast
0.013	-1	5.03	4.83	0.57 / 0.20	0.81	0.81	0.81 /0.81

Table 6.5: Input values for GENE simulations of #35938 at 5.0 - 5.5 s. Results are depicted by orange points in figure 4.8. Between the two simulations, only the fast ion population was varied; one time deuterium, the other time hydrogen.

q	s	$\omega_{E\times B}$	β_e	T_e	T_i	R/LT_e	R/LT_i
0.95	0.7	0.022 / 0.013	0.01	4.033	2.80	2.20	1.88

n_e	n_i	$n_\mathrm{fast,D}$	$n_\mathrm{fast,H}$	R/Ln_e	R/Ln_i	$R/Ln_\mathrm{fast,D}$	$R/Ln_\mathrm{fast,H}$
5.03	4.40	0.45	0.18	0.25	0.25	0.25	0.25

$T_\mathrm{fast,D,\parallel}$	$T_\mathrm{fast,D,\perp}$	$T_\mathrm{fast,H,\parallel}$	$T_\mathrm{fast,H,\perp}$	$R/LT_\mathrm{fast,D,\parallel}$	$R/LT_\mathrm{fast,D,\perp}$	$R/LT_\mathrm{fast,H,\parallel}$	$R/LT_\mathrm{fast,H,\perp}$
12.28	18.21	10.08	34.69	0.77	1.41	7.10	15.32

Table 6.6: Input values for GENE simulations of #35938 at 5.0 - 5.5 s. Results are depicted by orange points in figure 4.11. Between the two simulations, only $\omega_{E\times B}$ was varied.

q	s	T_e	T_i	T_{fast}	R/LT_e	R/LT_i	R/LT_{fast}
1.45 / 1.56 / 1.45	0.91 / 0.81 / 0.85	3.1	2.7	27.0	2.21	1.65	0.45

$\omega_{E\times B}$	β_e	n_e	n_i	n_{fast}	R/Ln_e	R/Ln_i	R/Ln_{fast}
0.047	0.012	5.31	4.57	0.74	0.99	0.86	1.77

Table 6.7: Input values for GENE simulations of #37114 at 3.5 - 4.0 s (weakly off-axis ECCD case). Results are depicted in table 5.1. Between the three simulations, only q and s were varied.

q	s	T_e	T_i	T_{fast}	R/LT_e	R/LT_i	R/LT_{fast}
1.56 / 1.45	0.81 / 0.91	3.1	2.87	27.86	2.00	1.96	0.48

$\omega_{E\times B}$	β_e	n_e	n_i	n_{fast}	R/Ln_e	R/Ln_i	R/Ln_{fast}
0.047	0.012	5.3	4.6	0.75	0.82	0.67	1.78

Table 6.8: Input values for GENE simulations of #37114 at 5.1 - 5.2 s (strongly off-axis ECCD case). Results are depicted in table 5.1. Between the two simulations, only q and s were varied.

q	s	T_e	T_i	T_{fast}	R/LT_e	R/LT_i	R/LT_{fast}
1.50 / 1.56	0.91 / 0.81	3.1	2.87	27.86	2.13	2.23	0.48

$\omega_{E\times B}$	β_e	n_e	n_i	n_{fast}	R/Ln_e	R/Ln_i	R/Ln_{fast}
0.047	0.012	5.3	4.5	0.75	0.82	0.67	1.78

Table 6.9: Input values for GENE simulations of #37114 at 5.1 - 5.2 s (strongly off-axis ECCD case). Results are depicted in table 5.2. Between the two simulations, only q and s were varied.

q	s	T_e	T_i	T_{fast}	R/LT_e	R/LT_i	R/LT_{fast}
1.02 / 1.14	0.48 / 0.35	3.82	3.14	31.2	1.75	1.75	0.65

$\omega_{E\times B}$	β_e	n_e	n_i	n_{fast}	R/Ln_e	R/Ln_i	R/Ln_{fast}
0.022	0.015	5.27	4.58	0.70	0.91	1.03	0.14

Table 6.10: Input values for GENE simulations of #35938 at 3.5 - 3.8 s (high $\omega_{E\times B}$ case). Results are depicted in table 5.2. Between the two simulations, only q and s were varied.

q	s	$\omega_{E \times B}$	β_{e}	T_{e}	T_{i}	R/LT_{e}	R/LT_{i}
0.98 / 0.95	0.75 / 0.7	0.013	0.01	4.033	2.80	2.20	1.88

n_{e}	n_{i}	$n_{\mathrm{fast,D}}$	$n_{\mathrm{fast,H}}$	R/Ln_{e}	R/Ln_{i}	$R/Ln_{\mathrm{fast,D}}$	$R/Ln_{\mathrm{fast,H}}$
5.03	4.40	0.45	0.18	0.25	0.25	0.25	0.25

$T_{\mathrm{fast,D,\|}}$	$T_{\mathrm{fast,D,\perp}}$	$T_{\mathrm{fast,H,\|}}$	$T_{\mathrm{fast,H,\perp}}$	$R/LT_{\mathrm{fast,D,\|}}$	$R/LT_{\mathrm{fast,D,\perp}}$	$R/LT_{\mathrm{fast,H,\|}}$	$R/LT_{\mathrm{fast,H,\perp}}$
12.28	18.21	10.08	34.69	0.77	1.41	7.10	15.32

Table 6.11: Input values for GENE simulations of #35938 at 5.0 - 5.5 s (low $\omega_{E \times B}$ case). Results are depicted table 5.2. Between the two simulations, only q and s were varied.

D   Results of simulations using the heuristic model
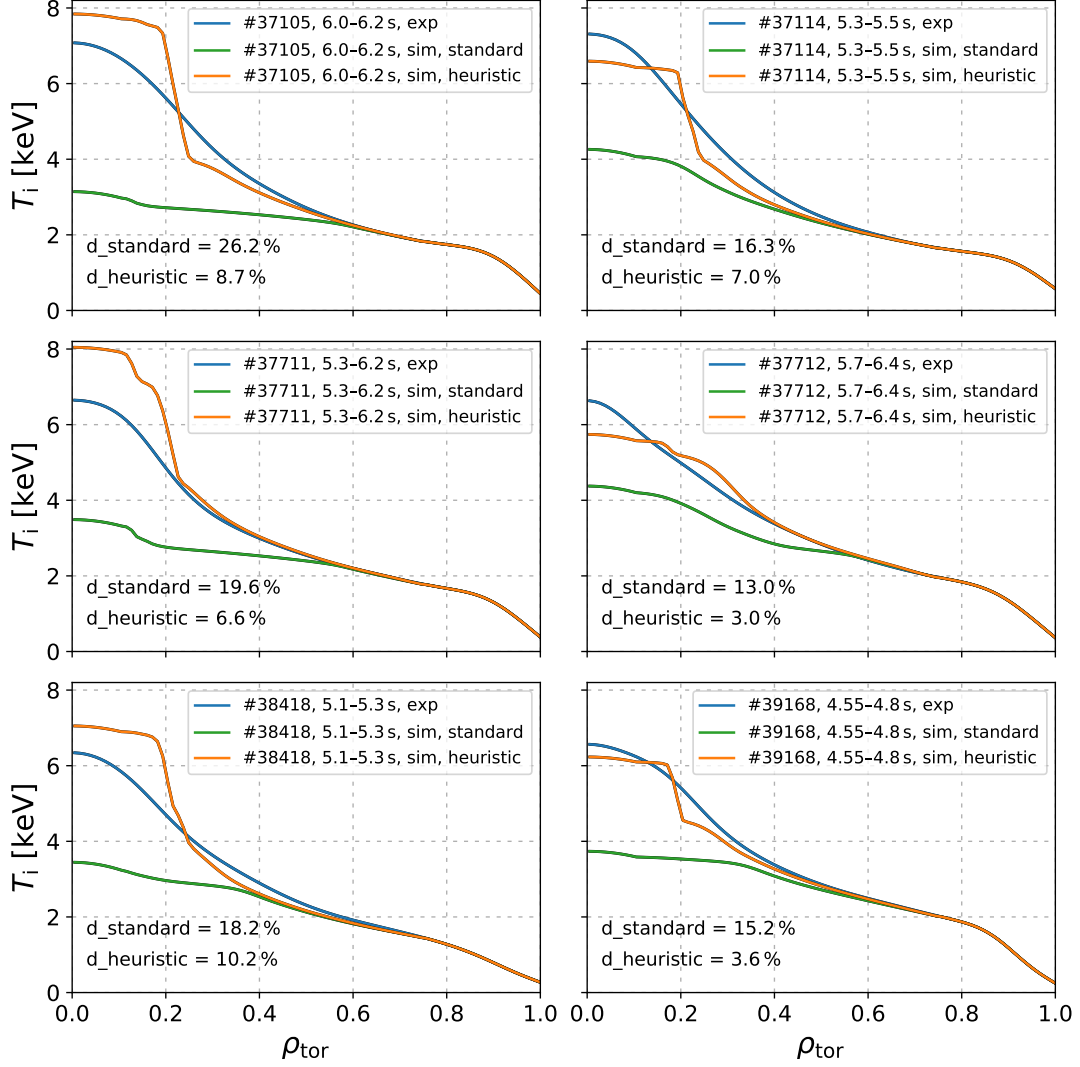
Figure 6.5: Ion temperature profiles of different discharges, comparing TGLF simulations with the inclusion of the heuristic model (orange) and without (green) to the experimental profiles (blue). Shown are all strongly off-axis cases that have not already been shown in figure 5.8.
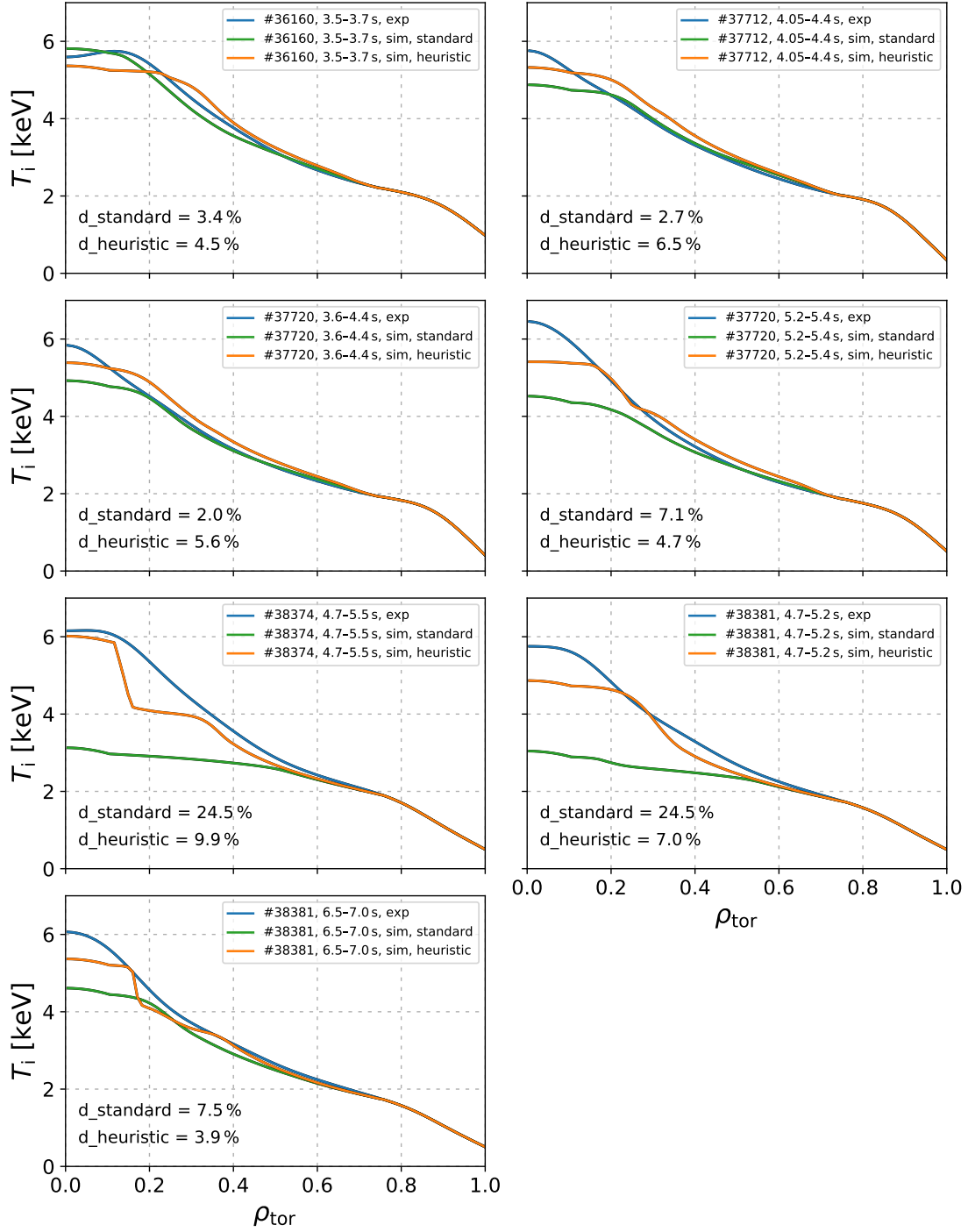
Figure 6.6: Ion temperature profiles of different discharges, comparing TGLF simulations with the inclusion of the heuristic model (orange) and without (green) to the experimental profiles (blue). Shown are all weakly off-axis cases that have not already been shown in figure 5.8.

Bibliography

[1] U.S. Energy Information Administration. International energy outlook 2021. `https://www.eia.gov/outlooks/ieo/pdf/IEO2021_Narrative.pdf`.

[2] International Atomic Energy Agency. Country nuclear power profiles – Germany. `https://cnpp.iaea.org/countryprofiles/Germany/Germany.htm`.

[3] John Wesson. *Tokamaks*. Oxford University Press, 3rd edition, 2004.

[4] H. Abu-Shawareb et al. Lawson criterion for ignition exceeded in an inertial fusion experiment. *Phys. Rev. Lett.*, 129:075001, 2022.

[5] Ulrich Stroth. *Plasmaphysik: Phänomene, Grundlagen und Anwendungen*. Springer Berlin Heidelberg, 2017.

[6] H.-S. Bosch et al. Final integration, commissioning and start of the Wendelstein 7-X stellarator operation. *Nucl. Fusion*, 57(11):116015, 2017.

[7] R.C. Wolf et al. Major results from the first plasma campaign of the Wendelstein 7-X stellarator. *Nucl. Fusion*, 57(10):102020, 2017.

[8] EuroFusion. Tokamak principle, 2011.

[9] Y. Shimomura et al. ITER overview. *Nucl. Fusion*, 39(9Y):1295–1308, 1999.

[10] R. Aymar et al. Overview of ITER-FEAT - The future international burning plasma experiment. *Nucl. Fusion*, 41(10):1301–1310, 2001.

[11] A. Bock et al. Non-inductive improved H-mode operation at ASDEX Upgrade. *Nucl. Fusion*, 57(12):126041, 2017.

[12] A. Bock et al. Advanced tokamak investigations in full-tungsten ASDEX Upgrade. *Phys. Plasmas*, 25(5):056115, 2018.

[13] H. Doerk et al. Turbulence in high-beta ASDEX Upgrade advanced scenarios. *Nucl. Fusion*, 58(1):016044, 2017.

[14] Thomas Pütterich. *Control and Diagnostic of High-Z Impurities in Fusion Plasmas*. Habilitation, Ludwig-Maximilians-Universität München, 2014.

[15] F. Troyon, R. Gruber, H. Saurenmann, S. Semenzato, and S. Succi. MHD-limits to plasma confinement. *Plasma Phys. Control. Fusion*, 26(1A):209–215, 1984.

[16] ITER Physics Expert Group on Disruptions, Plasma Control, and MHD and ITER Physics Basis Editors. Chapter 3: MHD stability, operational limits and disruptions. *Nucl. Fusion*, 39(12):2251–2389, 1999.

[17] Hartmut Zohm. *Magnetohydrodynamic Stability of Tokamaks*. Wiley, 2015.

[18] C. S. Pitcher and P. C. Stangeby. Experimental divertor physics. *Plasma Phys. Control. Fusion*, 39(6):779–930, 1997.

[19] R. J. Hastie. Sawtooth instability in tokamak plasmas. *Astrophysics and Space Science*, 256(1):177–204, 1997.

[20] B. B. Kadomtsev. Disruptive instability in tokamaks. *Soviet Journal of Plasma Physics*, 1:389, 1975.

[21] V. Igochine, O. Dumbrajs, H. Zohm, A. Flaws, and the ASDEX Upgrade Team. Stochastic sawtooth reconnection in ASDEX Upgrade. *Nucl. Fusion*, 47(1):23–32, 2006.

[22] R. Fischer et al. Sawtooth induced q-profile evolution at ASDEX Upgrade. *Nucl. Fusion*, 59(5):056010, 2019.

[23] R. Prater. Heating and current drive by electron cyclotron waves. *Phys. Plasmas*, 11(5):2349–2376, 2004.

[24] T. Ohkawa. Steady-state operation of tokamaks by R-F heating. Technical report, General Atomics, 1976.

[25] N. J. Fisch and A. H. Boozer. Creating an asymmetric plasma resistivity with waves. *Phys. Rev. Lett.*, 45:720–722, 1980.

[26] E. Poli, A.G. Peeters, and G.V. Pereverzev. TORBEAM, a beam tracing code for electron-cyclotron waves in tokamak plasmas. *Computer Physics Communications*, 136(1):90–104, 2001.

[27] J. D. Adam. Review of tokamak plasma heating by wave damping in the ion cyclotron range of frequency. *Plasma Phys. Control. Fusion*, 29:443, 1987.

[28] H. Kimura et al. Experimental study on beam acceleration with combined NBI heating and second-harmonic ICRF heating in JT-60. *Nucl. Fusion*, 31(1):83–92, 1991.

[29] M. Brambilla. Numerical simulation of ion cyclotron waves in tokamak plasmas. *Plasma Phys. Control. Fusion*, 41(1):1–34, 1999.

[30] R. Bilato et al. Simulations of combined neutral beam injection and ion cyclotron heating with the TORIC-SSFPQL package. *Nucl. Fusion*, 51(10):103034, 2011.

[31] T. H. Stix. Heating of toroidal plasmas by neutral injection. *Plasma Physics*, 14(4):367–384, 1972.

[32] M. M. Menon. Neutral beam heating applications and development. *Proceedings of the IEEE*, 69(8):1012–1029, 1981.

[33] David R. Mikkelsen and Clifford E. Singer. Optimization of steady-state beam-driven tokamak reactors. *Nuclear Technology - Fusion*, 4(2P1):237–252, 1983.

[34] A. Pankin, D. McCune, R. Andre, G. Bateman, and A. Kritz. The tokamak monte carlo fast ion module NUBEAM in the national transport code collaboration library. *Computer Physics Communications*, 159(3):157–184, 2004.

[35] TRANSP home page. https://transp.pppl.gov/index.html.

[36] G. V. Pereverzev and P. N. Yushmanov. ASTRA - Automated System for TRansport Analysis. Technical report, Max-Planck-Institut für Plasmaphysik, 2002.

[37] M. Weiland et al. RABBIT: Real-time simulation of the NBI fast-ion distribution. *Nucl. Fusion*, 58(8):082032, 2018.

[38] A. Polevoi, H. Shirai, and T. Takizuka. Benchmarking of the NBI block in ASTRA code versus the OFMC calculations. Technical Report JAERI Data/Code 97-014, Japan Atomic Energy Research Institute, 1997.

[39] A. G. Peeters. The bootstrap current and its consequences. *Plasma Phys. Control. Fusion*, 42(12B):B231–B242, 2000.

[40] EuroFusion. Charged particles movement, 2011.

[41] O. Sauter, C. Angioni, and Y. R. Lin-Liu. Neoclassical conductivity and bootstrap current formulas for general axisymmetric equilibria and arbitrary collisionality regime. *Phys. Plasmas*, 6(7):2834–2839, 1999.

[42] O. Sauter, C. Angioni, and Y. R. Lin-Liu. Erratum: "Neoclassical conductivity and bootstrap current formulas for general axisymmetric equilibria and arbitrary collisionality regime" [Phys. Plasmas 6, 2834 (1999)]. *Phys. Plasmas*, 9(12):5140–5140, 2002.

[43] Paulett C. Liewer. Measurements of microturbulence in tokamaks and comparisons with theories of turbulence and anomalous transport. *Nucl. Fusion*, 25(5):543–621, 1985.

[44] F. Romanelli. Models of plasma transport based on microturbulence. *Plasma Phys. Control. Fusion*, 31(10):1535–1549, 1989.

[45] D. H. Sharp. An overview of Rayleigh-Taylor instability. *Physica D: Nonlinear Phenomena*, 12(1):3–18, 1984.

[46] X. Garbet et al. Profile stiffness and global confinement. *Plasma Phys. Control. Fusion*, 46(9):1351–1373, 2004.

[47] F. Jenko, W. Dorland, and G. W. Hammett. Critical gradient formula for toroidal electron temperature gradient modes. *Phys. Plasmas*, 8(9):4096–4104, 2001.

[48] ASDEX team. The H-mode of ASDEX. *Nucl. Fusion*, 29(11):1959–2040, 1989.

[49] F. Wagner et al. Regime of improved confinement and high beta in neutral-beam-heated divertor discharges of the ASDEX tokamak. *Phys. Rev. Lett.*, 49:1408–1412, 1982.

[50] K. Ida and T. Fujita. Internal transport barrier in tokamak and helical plasmas. *Plasma Phys. Control. Fusion*, 60(3):033001, 2018.

[51] F. M. Levinton et al. Improved confinement with reversed magnetic shear in TFTR. *Phys. Rev. Lett.*, 75:4417–4420, 1995.

[52] Y. Koide et al. Internal transport barrier on q=3 surface and poloidal plasma spin up in JT-60U high-β_p discharges. *Phys. Rev. Lett.*, 72:3662–3665, 1994.

[53] E. Joffrin et al. Internal transport barrier triggering by rational magnetic flux surfaces in tokamaks. *Nucl. Fusion*, 43(10):1167–1174, 2003.

[54] H. Biglari, P. H. Diamond, and P. W. Terry. Influence of sheared poloidal rotation on edge turbulence. *Physics of Fluids B: Plasma Physics*, 2(1):1–4, 1990.

[55] P. Manz, M. Ramisch, and U. Stroth. Physical mechanism behind zonal-flow generation in drift-wave turbulence. *Phys. Rev. Lett.*, 103:165004, 2009.

[56] Katsumi Ida. Experimental studies of the physical mechanism determining the radial electric field and its radial structure in a toroidal plasma. *Plasma Phys. Control. Fusion*, 40(8):1429–1488, 1998.

[57] K. H. Burrell. Effects of E×B velocity shear and magnetic shear on turbulence and transport in magnetic confinement devices. *Phys. Plasmas*, 4(5):1499–1518, 1997.

[58] T. S. Hahm and K. H. Burrell. Flow shear induced fluctuation suppression in finite aspect ratio shaped tokamak plasma. *Phys. Plasmas*, 2(5):1648–1651, 1995.

[59] T. J. J. Tala, J. A. Heikkinen, V. V. Parail, Yu. F. Baranov, and S. J. Karttunen. ITB formation in terms of $\omega_{E\times B}$ flow shear and magnetic shears on JET. *Plasma Phys. Control. Fusion*, 43(4):507–523, 2001.

[60] N. Bonanomi et al. Turbulent transport stabilization by ICRH minority fast ions in low rotating JET ILW L-mode plasmas. *Nucl. Fusion*, 58(5):056025, 2018.

[61] E. J. Strait et al. Enhanced confinement and stability in DIII-D discharges with reversed magnetic shear. *Phys. Rev. Lett.*, 75:4421–4424, 1995.

[62] S. Ishida et al. Achievement of high fusion performance in JT-60U reversed shear discharges. *Phys. Rev. Lett.*, 79:3917–3921, 1997.

[63] R. C. Wolf et al. Performance, heating and current drive scenarios of ASDEX Upgrade advanced tokamak discharges. *Nucl. Fusion*, 41(9):1259–1271, 2001.

[64] R. C. Wolf. Internal transport barriers in tokamak plasmas. *Plasma Phys. Control. Fusion*, 45(1):R1–R91, 2002.

[65] R. E. Waltz, G. D. Kerbel, J. Milovich, and G. W. Hammett. Advances in the simulation of toroidal gyro-landau fluid model turbulence. *Phys. Plasmas*, 2(6):2408–2416, 1995.

[66] T. M. Antonsen et al. Physical mechanism of enhanced stability from negative shear in tokamaks: Implications for edge transport and the L-H transition. *Phys. Plasmas*, 3(6):2221–2223, 1996.

[67] G. Tardini et al. Thermal ions dilution and ITG suppression in ASDEX Upgrade ion ITBs. *Nucl. Fusion*, 47(4):280–287, 2007.

[68] A. Di Siena et al. Electromagnetic turbulence suppression by energetic particle driven modes. *Nucl. Fusion*, 59(12):124001, 2019.

[69] A. Di Siena et al. Nonlinear electromagnetic interplay between fast ions and ion-temperature-gradient plasma turbulence. *Journal of Plasma Physics*, 87(2):555870201, 2021.

[70] F. Jenko et al. Electron temperature gradient driven turbulence. *Phys. Plasmas*, 7(5):1904–1910, 2000.

[71] A. J. Brizard and T. S. Hahm. Foundations of nonlinear gyrokinetic theory. *Reviews of Modern Physics*, 79:421–468, 2007.

[72] G. M. Staebler et al. A theory-based transport model with comprehensive physics. *Phys. Plasmas*, 14(5):055909, 2007.

[73] G. M. Staebler, N. T. Howard, J. Candy, and C. Holland. A model of the saturation of coupled electron and ion scale gyrokinetic turbulence. *Nucl. Fusion*, 57(6):066046, 2017.

[74] G. M. Staebler, J. Candy, E. A. Belli, J. E. Kinsey, N. Bonanomi, and B. Patel. Geometry dependence of the fluctuation intensity in gyrokinetic turbulence. *Plasma Phys. Control. Fusion*, 63(1):015013, 2020.

[75] G. M. Staebler et al. A new paradigm for E×B velocity shear suppression of gyrokinetic turbulence and the momentum pinch. *Nucl. Fusion*, 53(11):113017, 2013.

[76] E Fable et al. Novel free-boundary equilibrium and transport solver with theory-based models and its validation against ASDEX Upgrade current ramp scenarios. *Plasma Phys. Control. Fusion*, 55:124028, 2013.

[77] ITER Physics Expert Group on Confinement and Transport, ITER Physics Expert Group on Confinement Modelling and Database and ITER Physics Basis Editors. Chapter 2: Plasma confinement and transport. *Nucl. Fusion*, 39(12):2175–2249, 1999.

[78] Xiang Jian et al. Key effects on the confinement improvement of the ASDEX Upgrade hybrid scenario. *Nucl. Fusion*, 59(10):106038, 2019. M. Reisner listed as co-author.

[79] Albrecht Herrmann and Otto Gruber. Chapter 1: ASDEX Upgrade - introduction and overview. *Fusion Science and Technology*, 44(3):569–577, 2003.

[80] R. Neu et al. Tungsten as plasma-facing material in ASDEX Upgrade. *Fusion Engineering and Design*, 65(3):367 – 374, 2003.

[81] V. Rohde, R. Dux, A. Kallenbach, K. Krieger, and R. Neu. Wall conditioning in ASDEX Upgrade. *Journal of Nuclear Materials*, 363-365:1369–1374, 2007. Plasma-Surface Interactions-17.

[82] Bernhard Streibl, Peter Thomas Lang, Fritz Leuterer, Jean-Marie Noterdaeme, and Albrecht Stäbler. Chapter 2: Machine design, fueling, and heating in ASDEX Upgrade. *Fusion Science and Technology*, 44(3):578–592, 2003.

[83] D. Wagner et al. Status, operation, and extension of the ECRH system at ASDEX Upgrade. *Journal of Infrared, Millimeter, and Terahertz Waves*, 37(1):45–54, 2016.

[84] J. Stober et al. Exploring fusion-reactor physics with high-power electron cyclotron resonance heating on ASDEX Upgrade. *Plasma Phys. Control. Fusion*, 62(2):024012, 2020. M. Reisner listed as co-author.

[85] K. Felch, H. Huey, and H. Jory. Gyrotrons for ECH applications. *Journal of Fusion Energy*, 9:59–75, 1990.

[86] V. Bobkov et al. Progress in reducing ICRF-specific impurity release in ASDEX Upgrade and JET. *Nuclear Materials and Energy*, 12:1194–1198, 2017. Proceedings of the 22nd International Conference on Plasma Surface Interactions 2016, 22nd PSI.

[87] A. Mlynek et al. Design of a digital multiradian phase detector and its application in fusion plasma interferometry. *Rev. Sci. Instrum.*, 81(3):033507, 2010.

[88] A. Mlynek, L. Casali, O. Ford, and H. Eixenberger. Fringe jump analysis and implementation of polarimetry on the ASDEX Upgrade DCN interferometer. *Rev. Sci. Instrum.*, 85(11):11D408, 2014.

[89] H. J. Hartfuss, T. Geist, and M. Hirsch. Heterodyne methods in millimetre wave plasma diagnostics with applications to ECE, interferometry and reflectometry. *Plasma Phys. Control. Fusion*, 39(11):1693–1769, 1997.

[90] W. Suttrop, A.G. Peeters, and the ASDEX Upgrade team. Practical limitations to plasma edge electron temperature measurements by radiometry of electron cyclotron emission. Technical report, Max Planck Institut für Plasmaphysik, 1996.

[91] S. S. Denk et al. Analysis of electron cyclotron emission with extended electron cyclotron forward modeling. *Plasma Phys. Control. Fusion*, 60(10):105010, 2018.

[92] B. Kurzan and H. D. Murmann. Edge and core Thomson scattering systems and their calibration on the ASDEX Upgrade tokamak. *Rev. Sci. Instrum.*, 82(10):103501, 2011.

[93] E. Viezzer, T. Pütterich, R. Dux, and R. M. McDermott. High-resolution charge exchange measurements at ASDEX Upgrade. *Rev. Sci. Instrum.*, 83(10):103501, 2012.

[94] S. K. Rathgeber et al. Estimation of profiles of the effective ion charge at ASDEX Upgrade with integrated data analysis. *Plasma Phys. Control. Fusion*, 52(9):095008, 2010.

[95] R. M. McDermott et al. Extensions to the charge exchange recombination spectroscopy diagnostic suite at ASDEX Upgrade. *Rev. Sci. Instrum.*, 88(7):073508, 2017.

[96] M. Cavedon et al. A fast edge charge exchange recombination spectroscopy system at the ASDEX Upgrade tokamak. *Rev. Sci. Instrum.*, 88(4):043103, 2017.

[97] F. M. Levinton et al. Magnetic field pitch-angle measurments in the PBX-M tokamak using the motional stark effect. *Phys. Rev. Lett.*, 63:2060–2063, 1989.

[98] R.C. Wolf et al. Motional stark effect measurements of the local magnetic field in high temperature fusion plasmas. *Journal of Instrumentation*, 10(10):P10008–P10008, 2015.

[99] O. P. Ford, J. Howard, and R. C. Wolf. The prototype imaging motional stark effect diagnostic for ASDEX Upgrade. *Rev. Sci. Instrum.*, 86(9):093504, 2015.

[100] O. P. Ford, A. Burckhart, R. McDermott, T. Pütterich, and R. C. Wolf. Imaging motional stark effect measurements at ASDEX Upgrade. *Rev. Sci. Instrum.*, 87(11):11E537, 2016.

[101] R. Fischer et al. Integrated data analysis of profile diagnostics at ASDEX Upgrade. *Fusion Science and Technology*, 58(2):675–684, 2010.

[102] J. Schweinzer et al. Reconstruction of plasma edge density profiles from Li I (2s-2p) emission profiles. *Plasma Phys. Control. Fusion*, 34(7):1173–1183, 1992.

[103] R. Fischer et al. Estimation and uncertainties of profiles and equilibria for fusion modeling codes. *Fusion Science and Technology*, 76(8):879–893, 2020.

[104] A. Ho et al. Application of gaussian process regression to plasma turbulent transport model validation via integrated modelling. *Nucl. Fusion*, 59(5):056007, 2019.

[105] P. J. McCarthy, P. Martin, and W. Schneider. The CLISTE interpretive equilibrium code. Technical Report IPP 5/85, Max-Planck-Institut für Plasmaphysik, May 1999.

[106] R. Fischer et al. Coupling of the flux diffusion equation with the equilibrium reconstruction at ASDEX Upgrade. *Fusion Science and Technology*, 69(2):526–536, 2016.

[107] C. C. Petty et al. Magnetic-flux pumping in high-performance, stationary plasmas with tearing modes. *Phys. Rev. Lett.*, 102:045005, 2009.

[108] P. Piovesan et al. Role of a continuous MHD dynamo in the formation of 3D equilibria in fusion plasmas. *Nucl. Fusion*, 57(7):076014, 2017.

[109] A. Gude, M. Maraschek, O. Kardaun, and the ASDEX Upgrade Team. An automated sawtooth detection algorithm for strongly varying plasma conditions and crash characteristics. *Plasma Phys. Control. Fusion*, 59(9):095009, 2017.

[110] A. Lebschy et al. Measurement of the complete core plasma flow across the LOC–SOC transition at ASDEX Upgrade. *Nucl. Fusion*, 58(2):026013, 2017.

[111] Alexander Lebschy. *Experimental characterization of the core plasma flow at the ASDEX Upgrade tokamak.* PhD thesis, Technische Universität München, 2018.

[112] A. Bortolon et al. Indirect measurement of poloidal rotation using inboard-outboard asymmetry of toroidal rotation and comparison with neoclassical predictions. *Nucl. Fusion*, 53:023002, 2013.

[113] R. Neu et al. Impurity behaviour in the ASDEX Upgrade divertor tokamak with large area tungsten walls. *Plasma Phys. Control. Fusion*, 44(6):811–826, 2002.

[114] Simulations performed by Alessandro Di Siena, benefiting from HPC resources from CINECA Marconi-Fusion (Project FUA35_STATS; Project leader: M. Reisner).

[115] A. Di Siena et al. Non-maxwellian fast particle effects in gyrokinetic gene simulations. *Phys. Plasmas*, 25(4):042304, 2018.

[116] M. Reisner et al. Increased core ion temperatures in high-beta advanced scenarios in ASDEX Upgrade. *Nucl. Fusion*, 60(8):082005, 2020.

[117] Fuchang Gao and Lixing Han. Implementing the nelder-mead simplex algorithm with adaptive parameters. *Comput. Optim. Appl.*, 51(1):259–277, 2012.

[118] Andreas Burckhart and Rainer Fischer. Private Communication, 2021.

[119] Anja Gude. Private Communication, 2021.

[120] Rainer Fischer. Private Communication, 2022.

Acknowledgements